RUPRECHT-KARLS-UNIVERSITÄT HEIDELBERG

Pavel Weber

ATLAS Calorimetry: Trigger, Simulation and Jet Calibration

Dissertation

HD-KIP-08-03

CERN-THESIS-2008-253

KIRCHHOFF-INSTITUT FÜR PHYSIK

Dissertation
submitted to the
Joint Faculties for Natural Sciences and Mathematics
of the Ruperto Carola University of
Heidelberg, Germany,
for the degree of
Doctor of Natural Sciences

presented by

Dipl.Phys.: Pavel Weber
born in: Grozny, Russia

Heidelberg, February 6, 2008

ATLAS Calorimetry: Trigger, Simulation and Jet Calibration

Gutachter: Prof. Dr. Karlheinz Meier
Prof. Dr. Ulrich Uwer

Zusammenfassung

Das Pre-Processor-System des ATLAS Level-1 Kalorimeter-Triggers führt eine komplexe Verarbeitung von analogen Signalen des elektromagnetischen und hadronischen Kalorimeters durch. Der Hauptteil der Signalverarbeitung des Pre-Processor-Systems erfolgt in Multi-Chip Modulen (MCM). Der erste Teil dieser Arbeit beschreibt die Entwicklung von Qualitätsprüfungen für die MCM, ihre Anwendung in der MCM Serienproduktion und die erzielten Ergebnisse.

Im zweiten Teil dieser Arbeit wurden Validierungsstudien für ein Modell der Schauer-Parametrisierung im ATLAS-Programm für schnelle Detektorsimulationen ATLFAST erfolgt. In den auf simulierten QCD-Dijet-Ereignissen basierten Studien wurden detaillierte Vergleiche des Detektor-Ansprechverhaltens und der Energieauflösung für Jets zwischen der schnellen und der vollen Simulation des Detektors durchgeführt.

Die Homogenität des Kalorimeter-Ansprechverhaltens über den gesamten Raumwinkel ist ein entscheidender Qualitätsfaktor für die Messung der Jetenergie. Eine Studie zur Interkalibration des Kalorimeters mit Hilfe von Dijet-Ereignissen ist im letzten Teil dieser Arbeit dargestellt. Die Interkalibration wird im Azimutwinkel ϕ und in der Pseudorapidität η durchgeführt. Die Leistungsfähigkeit der Kalibrationsmethoden, inklusive möglicher statistischer und systematischer Effekte, wird diskutiert.

Abstract

The Pre-Processor system of the ATLAS Level-1 Calorimeter Trigger performs complex processing of analog trigger tower signals from electromagnetic and hadronic calorimeters. The main processing block of the Pre-Processor System is the Multi-Chip Module (MCM). The first part of this thesis describes MCM quality assurance tests that have been developed, their use in the MCM large scale production and the results that have been obtained.

In the second part of the thesis a validation of a shower parametrisation model for the ATLAS fast simulation package ATLFAST based on QCD dijet events is performed. A detailed comparison of jet response and jet energy resolution between the fast and the full simulation is presented.

The uniformity of the calorimeter response has a significant impact on the accuracy of the jet energy measurement. A study of the calorimeter intercalibration using QCD dijet events is presented in the last part of the thesis. The intercalibration study is performed in azimuth angle ϕ and in pseudorapidity η. The performance of the calibration methods including possible systematic and statistical effects is described.

Oh, how many wonderful discoveries
are prepared for us by the spirit of enlightenment,
and by experience, the son of hard errors,
and by a genius, the paradoxes' friend,
and by accident, the master of invention.

A.S. Pushkin, 1829

Contents

Introduction

ATLAS (A Toroidal LHC ApparatuS) is a general purpose *pp* detector which is designed to exploit the full discovery potential of the LHC. The main interests of ATLAS are the discovery of the Higgs boson and searches for the experimental signatures of new physics beyond the Standard Model of particle physics.

Very small cross-sections of events with interesting physics signatures, as compared to the background processes in the examined energy range, set stringent requirements for the ATLAS trigger and Data Acquisition (DAQ) system. Taking into account the expected event rate of 10^9 Hz the trigger system has to provide a total reduction rate of 10^7 which corresponds to an $\mathcal{O}(100)$ Hz event rate for storage. Furthermore the trigger has to be highly efficient in selecting rare events. To meet these requirements the ATLAS Trigger is built as a system which has three levels of event selection: Level-1, Level-2 and Event Filter.

The first part of the thesis is dedicated to the commissioning and production tests of the Multi-Chip Module (MCM) which is the main processing block of the Pre-Processor System in the ATLAS Level-1 Calorimeter Trigger. Being a complex electronic device it holds the main functionality of the Pre-Processor System, namely the digitization, calibration and bunch-crossing identification of calorimeter signals. It has to be stressed that the correct functionality of the MCM is of crucial importance for the performance of the whole ATLAS trigger system.

A complete understanding of the ATLAS detector and background processes is an important task for the initial period of data taking. A comparison between experimental data and Monte Carlo simulations allows us to study the detector performance and background processes. The ATLAS full simulation provides a detailed description of the detector, but is very CPU time consuming. A fast simulation is an important tool for high-statistics studies, estimation of signal and background rates.

The studies of the performance of the calorimeter shower parametrisation model implemented in the fast simulation are described in the second part of the thesis. The model provides an improved description of the calorimeter geometry and shower development in the ATLAS calorimeter, compared to the previous fast simulation version.

The ATLAS calorimetry system is expected to play a leading role in the many searches in the high energy domain as well as in precision measurements of particle energies. The accuracy for most of the measurements planned in the ATLAS experiment at the LHC depends on jet energy measurements which will be carried out in the calorimetry. The uniformity of the calorimeter response is important for improving the precision of the energy measurements. The last part of the thesis is devoted to calorimeter intercalibration studies based on QCD jets.

In the first chapter a physics overview is given. The main components of the Standard Model of particle physics and the physics programme of ATLAS are outlined. An overview of the jet physics from the experimental point of view is also presented. In the second chapter the accelerator facilities as well as the ATLAS detector and the trigger system are described. The third chapter is dedicated to the ATLAS Level-1 Calorimeter Trigger. A detailed description of the tasks and algorithms as well as the architecture of the three main processors of the Level-1 Calorimeter Trigger is given. The next two chapters are devoted to Multi-Chip Module. The chapter four describes the development of MCM quality assurance tests. The MCM large scale tests and production are described in chapter five. In the second part of the thesis, in chapter six, a shower parametrisation model implemented in fast the detector simulation is studied. The results of the performance tests of this model based on dijet events are presented. The seventh chapter is dedicated to the calorimeter intercalibration studies. A summary is given at the end of the thesis.

Chapter 1

Physics at the LHC

1.1 The Standard Model of particle physics

1.1.1 The Standard Model

The fundamental quantum fields of matter and the forces between them are described in the theoretical framework known as Standard Model of Fundamental Particles and Interactions. This framework was basically developed in the seventies of the twentieth century. Plenty of data accumulated in accelerator experiments and analysed by that time allowed the appearance of a theory of fundamental particles. The Standard Model (SM) describes strong, electromagnetic and weak interactions. The gravity is not included in the SM, as up to now there is no proven theory of quantum gravity.

According to the SM, fundamental matter is built of six leptons and six quarks which are spin-$\frac{1}{2}$ fermions. While the leptons carry integral electrical charges, quarks carry fractional charges. The fundamental fermions are grouped into three families or "generations" of matter consisting of lepton and quark doublets as shown in Figure 1.1. Each fermion has a corresponding antiparticle partner which has identical mass and spin value and opposite values for all other quantum numbers.

$$\begin{array}{cccc} & \multicolumn{3}{c}{\textbf{Generations}} \\ & \textbf{I} & \textbf{II} & \textbf{III} \\ \textbf{Leptons} & \begin{pmatrix} e \\ \nu_e \end{pmatrix} & \begin{pmatrix} \mu \\ \nu_\mu \end{pmatrix} & \begin{pmatrix} \tau \\ \nu_\tau \end{pmatrix} \\ & & & \\ \textbf{Quarks} & \begin{pmatrix} u \\ d \end{pmatrix} & \begin{pmatrix} c \\ s \end{pmatrix} & \begin{pmatrix} t \\ b \end{pmatrix} \end{array}$$

Figure 1.1: The Fermion Families in the Standard Model.

The stable matter observed till now in the Universe is made of fermions of the first generation. While leptons exist as free particles, isolated free quarks have never been observed experimentally. Bound states of three quarks form baryons, such as the proton or the neutron, which consist of the lightest u and d quarks. Combinations of a quark and an antiquark yield a meson, such as *e.g.* the pion or the kaon.

The interactions between fermions are mediated by gauge bosons, namely gluons (g), photons (γ) as well as $W^{\pm} and\ Z^0$ bosons. Table 1.1 summarises the main properties of

Table 1.1: Fundamental forces with coupling strength

Interaction	**Mediator**	**Range,m**	**Coupling**
Strong	gluon, g	1 Fermi	1
Electromagnetic	photon, γ	∞	10^{-2}
Weak	$W^{\pm}, Z^0$	10^{-18}	10^{-7}
gravity	(graviton)	∞	10^{-39}

the known fundamental interactions [1].

The Standard Model is described by the $SU(3) \times SU(2) \times U(1)$ gauge group. The group $SU(3)$ is the symmetry gauge group of the theory of the strong interactions known as Quantum Chromodynamics (QCD). Strong interactions are responsible for binding the quarks in the neutron and proton, and the neutrons and protons within nuclei. The three colour charges of the quarks, R (red), G (green), and B (blue) form a fundamental representation of the $SU(3)$ symmetry group, which is a triplet. All quarks are assigned to this triplet. The gluons which mediate interactions between quarks belong to an $SU(3)$ color octet. All hadrons are colourless and belong to a singlet representation of the $SU(3)$ colour group.

Electromagnetic interactions are observed between charged particles and mediated by the photon. These interactions are described by Quantum Electrodynamics (QED), which is a gauge theory with only one gauge particle, the photon. It has to be mentioned, that perturbative calculations of the scattering amplitude in quantum field theories like QED face an essential difficulties, namely divergent terms associated with momentum calculations in the integrals over intermediate states, like vacuum polarisation loops. The procedure which absorbs these divergent parts by redefinition of "bare" lepton charges and masses in terms of their experimentally observed values and makes the amplitude of the process finite is called renormalisation. The theories to which the renormalisation procedure can be applied are renormalisable.

The electromagnetic interaction is unified together with the weak interaction in the framework of electroweak theory. This theory was developed by Glashow, Weinberg and Salam based on Yang-Mills gauge theories. The electroweak theory is constructed from a gauge theory with four gauge fields and four gauge bosons, arranged in a triplet and a singlet as members of multiplets of "weak isospin" I and "weak hypercharge" Y. Three of the bosons, denoted $W_\mu = W_\mu^{(1)}, W_\mu^{(2)}, W_\mu^{(3)}$, are the components of an $I = 1$ triplet of the group $SU(2)$, while the fourth, B_μ, is an isoscalar ($I = 0$) or single vector field belonging to the $U(1)$ group of weak hypercharge[1].

The fields

$$W_\mu^{\pm} = \sqrt{\frac{1}{2}}(W_\mu^1 \pm iW_\mu^2) \tag{1.1}$$

describe charged vector bosons $W^{\pm}$, that mediate the charged current interactions, while

---

[1] W_μ is an isovector, which refers to the vector transformation of a particle under the $SU(2)$ group of isospin. An isovector state is a triplet state with total isospin 1; superscripts 1, 2, 3 indicate the components in 'isospin space'. The subscript μ signifies the space-time components of a 4-vector ($\mu = 1, 2, 3, 4$).

the photon A_μ and the neutral vector boson Z^0_μ are combinations of the states $W^{(3)}_\mu$ and B_μ:

$$A_\mu = B_\mu \cos\theta_W + W^3_\mu \sin\theta_W, \tag{1.2}$$

$$Z_\mu = -B_\mu \sin\theta_W + W^3_\mu \cos\theta_W, \tag{1.3}$$

where θ_W is the Weinberg or weak mixing angle.

Serious problem arose after the attempt to introduce mass terms for the gauge fields to the Lagrangian. It was found that the addition of the these mass terms destroys the gauge invariance of the Lagrangian, and the theory becomes unrenormalisable. An elegant solution called "spontaneous symmetry breaking" was found in order to introduce the masses of the gauge bosons – W^+_μ, W^-_μ and Z^0_μ and preserve the gauge symmetry. The spontaneous symmetry breaking is determined by the Higgs [2] mechanism and new complex scalar fields, the Higgs fields. The gauge bosons and the fermions acquire masses upon coupling to the vacuum Higgs field. The important consequence of these pure theoretical considerations for the experimental physics is an appearance of a physical neutral scalar Higgs boson, which is predicted to exist as a free particle [3].

Although the Standard Model is far away from the dream of modern physics, which is unification of all fundamental interactions, it was remarkably successful at energy scales of 100 GeV accessible to current experiments. It allowed to predict the existence and intrinsic properties of many fundamental particles - W-, Z- bosons, gluon, charm and top quarks. Later on, these particles were observed and measured at experimental facilities. The only part that has not been tested is the Higgs mechanism. The discovery of the Higgs boson and the understanding of electroweak symmetry breaking is the major hope of particle physics at the LHC.

1.1.2 Quantum Chromodynamics

Parton Model

The proposal formulated in 1964 by Gell-Mann [6] and by Zweig [7] that hadrons were built from fractionally charged quarks appeared as underlying scheme to justify a highly successful classification of the hadrons, known that times. This proposal initiated the exhaustive searches for quarks at particles accelerators and in cosmic rays. The absence of any experimental evidence of the quarks was interpreted by the assumption that quarks must be extremely massive and very tightly bound in hadrons. The situation changed after a series of experiments on Deep Inelastic electron Scattering (DIS) was performed at the Stanford Linear Accelerator Center (SLAC) [8]. The process under study can be written as:

$$e + p \to e + X. \tag{1.4}$$

The squared four-momentum transfer in this process from the lepton to the hadron carried by the virtual photon is defined as Q^2:

$$Q^2 = -(l - l')^2, \tag{1.5}$$

where l is the four-momentum of the initial electron and l' is the four-momentum of the scattered electron. The goal of the experiment was to answer the question, whether there are point-like constituents which serve as scattering centers in the nucleus, similar to the goal of the Rutherford experiment for the atom. It was shown that the differential cross-section for electron scattering off the nucleon is described by two structure functions F_1

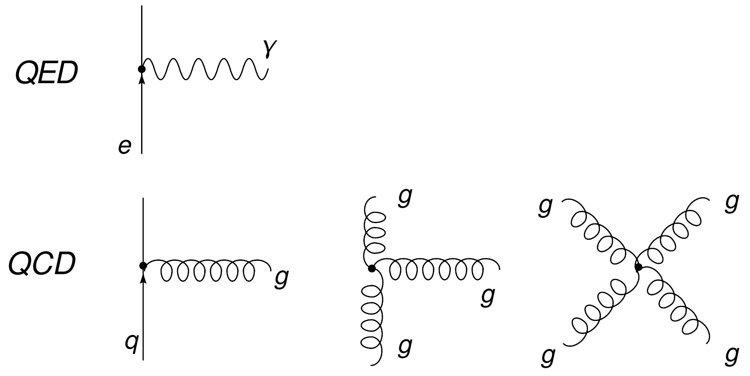

Figure 1.2: Basic QED and QCD vertices.

and F_2, which summarise all the information about the structure of the target particles. Based on the experimental data it was found that the inelastic cross-section has a weak dependence on Q^2 and significantly depends only on the dimensionless Bjorken-variable x, defined as:

$$x = \frac{Q^2}{2Pq}, \tag{1.6}$$

where P is the proton four-momentum and q is the four-momentum of the virtual photon. The fact that the DIS cross-section is almost independent of Q^2 is referred to as Bjorken scaling. The observation of scaling was the first evidence of the existence of point-like dimensionless scattering centers inside the nucleon, the partons. The predictions of quarks and observation of partons in the experiment merge in the Quark Parton Model (QPM). In the QPM a proton is composed of quasi-free non-interacting partons identified with quarks, each carrying a fraction of the parent hadron's longitudinal momentum. The variable x can be identified with the four-momentum fraction x carried by the struck parton before entering the scattering process [9].

QCD theory

The QPM, sometimes referred to as "naive parton model", gave a good first-order description for all subsequent data obtained in the DIS experiments, but still many questions concerning the proton structure remained unresolved.

The development of the theory of quantum chromodynamics, a gauge theory of the strong interactions, was the next successful step in understanding the nucleon structure. A central statement of the theory is that quarks possess three colors and interact by exchanging eight spin-1 gauge bosons – bicolored gluons. Thus, gluons play the same role for the strong interaction as photons do for the electromagnetic force. An important difference is that in QED the photon can only couple to an electric charge, and therefore there is only one basic vertex. In QCD, the gluon couples to color charges on quarks or on other colored gluons. The difference in coupling in QED and QCD is shown in Figure 1.2.

The effect of gluon self-coupling becomes apparent in antishielding the color charge in contrast to the QED screening effect. The strong force that is expressed by the strong coupling $\alpha_S(Q)$ decreases with approaching to the color charge. At short distances, or in other words at very large momentum transfers, strong interactions are sufficiently weak, quarks and gluons are essentially free particles. This phenomenon is known as asymptotic freedom [10]. At the energy scale where the processes involve a large momentum transfer the perturbative approach in QCD diagram calculations becomes possible. As the strong coupling varies with momentum transfer, the term "running coupling constant" is often used in this sense. To leading order, α_s is given by:

$$\alpha_s(Q^2) = \frac{12\pi}{(33 - 2N_f)\ \ln(Q^2/\Lambda^2)}\ , \tag{1.7}$$

where N_f is the number of quark flavours and Λ is an energy scale close to which non-perturbative effects become important. For Q^2 values much larger than Λ^2, the coupling is small and perturbative description of quark and gluon interactions becomes possible. For Q^2 of order Λ^2, quarks and gluons will arrange themselves into strongly bound clusters, namely hadrons, and the perturbative approach will not be possible any more. The value of Λ is to be determined from experiment.

Hadron-hadron collisions

Hadron-hadron interactions can basically be classified into soft and hard ones. Soft interactions are characterised by small momentum transfers, resulting in small transverse momenta of outgoing particles. The hard interactions are usually rare processes with large momentum transfers, compared to soft events.

Consider the inclusive scattering process:

$$h_1 + h_2 \to X, \tag{1.8}$$

which results from the 2-to-2 hard scattering constituent subprocess:

$$a + b \to c + d, \tag{1.9}$$

where h_1 and h_2 are incoming hadrons, X represents any kinematically allowed final state particles. The lowest order hadron-hadron scattering diagram is shown in Figure 1.3. The formula, which gives the cross-section for the collision of incoming hadrons h_1 and h_2 is [12]:

$$d\sigma(h_1 h_2 \to X) = \int_0^1 dx_1 dx_2 \sum_{a,b} f_{a/h_1}(x_1, \mu_F^2) f_{b/h_2}(x_2, \mu_F^2) d\hat{\sigma}^{(ab\to cd)}(Q^2, \mu_F^2), \tag{1.10}$$

here the terms f_{a/h_1} and f_{b/h_2} are parton density functions (PDFs). In general, the parton density function $f_i(x)$ determines the momentum-fraction distribution for a given parton type i (*e.g.* gluon, valence quark or sea quark of a particular flavour) in the hadron. In other words, PDF defines the probability for a given parton type to be found with momentum fraction between x and $x + dx$:

$$f(x)dx = P(x' \in [x, x + dx]); \quad f = q, \bar{q}\ or\ g, \tag{1.11}$$

where x is defined as the Bjorken variable by eq. (1.6). Parton distributions are non-perturbative in nature and cannot be calculated. They must instead be extracted from experimental data and then evolved up to a desired Q^2. As was discussed above the naive parton model assumes the presence of non-interacting point-like scattering centers inside the nucleon and ignores the role of gluons as the carriers of the strong force associated with colored quarks. If we take into account that quarks can radiate gluons in DIS processes

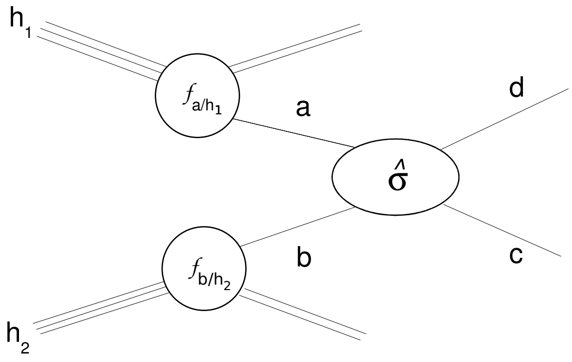

Figure 1.3: Hadron-hadron scattering diagram.

before or after being struck by the virtual photon, then we have to accept that the scaling property of structure functions will no longer be true. This means that a quark which at lower Q^2 is just seen as a point-like particle will be resolved into more partons at higher momentum transfers, and the total four-momentum of the nucleon will be distributed over more constituents. With increasing Q^2, the structure function increases at small x and decreases at large x, which is the scaling violation. The experimental data confirmed this behaviour. That means that in the improved parton model the PDFs are functions not only of x, but also of the squared four-momentum transfer Q^2. The evolution of the PDFs with Q^2 is shortly discussed below.

The hard cross-section $\hat{\sigma}$ for the partonic interaction is calculated perturbatively. The real picture of hadron-hadron scattering in the improved parton model is much more complicated compared to the one depicted in Figure 1.3. The presence of soft and collinear gluon emission off the incoming partons introduces the divergences to perturbative calculation of virtual (loop) diagrams. The way how this problem is treated is factorisation of the cross-section into short-distance, hard subprocess, involving partons, and a long-distance part, the PDFs, describing the hadrons involved. The partons emitted at small transverse momenta are absorbed into $f_{a/h_1}(x_1, \mu_F^2)$ and $f_{b/h_2}(x_2, \mu_F^2)$ and considered as a part of hadron structure, on the other hand the partons emitted at large transverse momenta contribute to the calculable part of the cross-section. The scale at which this separation is performed is referred to as the factorisation scale μ_F. The hadron cross-section in eq. (1.10) is a sum of partonic cross-sections weighted by their PDFs over all the possible contributing partons and integrated over the momentum fraction.

Although the distribution function $q(x, \mu^2)$ can not be calculated by perturbation theory, when measured experimentally it can be modified at any particular value $\mu^2 = \mu_0^2$. This modification of the PDFs is done by using the integro-differential DGLAP evolution equations named after Dokshitzer, Gribov, Lipatov, Altarelli and Parisi [13, 14, 15]. In other words, the DGLAP equations determine the Q^2 dependence of the PDFs, while the x dependence is defined from fitting of experimental data.

In the hadron-hadron collision in Figure 1.3 the two partons a and b carry momenta $x_1 P_{h_1}$ and $x_2 P_{h_2}$ of the longitudinal momentum of hadrons, where P_{h_1} and P_{h_2} are incoming hadron four-momenta in the center-of-mass[2] (cms) frame. Neglecting the particle

---

[2] The center-of-mass frame is defined as the reference frame in which the total 3-momentum is zero.

masses the four-momenta of the incoming hadrons are:

$$P_{h_1} = (E, 0, 0, E), \ \ P_{h_2} = (E, 0, 0, -E), \tag{1.12}$$

where E is the beam energy. The total cms energy squared for the hadron system is:

$$s = (P_{h_1} + P_{h_2})^2 = 4E^2, \tag{1.13}$$

The cms energy squared for the hard subprocess is related to the corresponding hadronic quantity by

$$M^2 = \hat{s} = (x_1 P_{h_1} + x_2 P_{h_2})^2 = ((x_1 + x_2)E, 0, 0, (x_1 - x_2)E) = x_1 x_2 s, \tag{1.14}$$

The difference in the momentum fractions x_1 and x_2 leads to a longitudinal momentum imbalance, thus the final state will be boosted along the direction of the beam axis. The four-momentum of the boosted final state can be written as:

$$P_{final} = (M \cosh y, p_x, p_y, M \sinh y), \tag{1.15}$$

where y is the rapidity as defined in Appendix A. Comparing the eq. (1.14) and eq. (1.15) one can write:

$$cosh\ y = \frac{x_1 + x_2}{2\sqrt{x_1 x_2}} = \frac{1}{2}\left(\sqrt{\frac{x_1}{x_2}} + \sqrt{\frac{x_2}{x_1}}\right). \tag{1.16}$$

Using eq. (1.16) and eq. (1.14) the mass and rapidity of the final state can be related to the momentum fraction of the incoming partons:

$$x_1 = \frac{M}{\sqrt{s}} e^{y}, \quad x_2 = \frac{M}{\sqrt{s}} e^{-y}. \tag{1.17}$$

Figure 1.4 shows a x-Q^2 map for the production of a particle of mass M at rapidity y at the LHC and at HERA as well as at fixed target experiments. For a given rapidity y and mass M the intersections of two inclined lines which define the rapidity and a horizontal line correspond to the required x_1 and x_2 values. The PDF values for the LHC kinematic range are obtained from those measured at HERA at the same x values via the DGLAP evolution in Q^2.

A number of partons produced in hard scattering process undergo gluon radiation resulting in showers of soft partons which finally hadronise.The process of fragmentation or hadronisation, is the process, in which the quarks and gluons of perturbative QCD are converted into the hadrons that are seen in the detectors. The fragmentation is intrinsically non-perturbative process and phenomenologically described by hadronisation models implemented in the Monte Carlo generators [17].

1.2 Physics programme with the ATLAS detector

The first proton-proton collisions will allow one to observe and measure the well-known Standard Model signals and do searches for processes beyond the SM at a completely new energy. The broad ATLAS physics programme can be summarised as follows:

- SM Higgs boson searches. The discovery of the Higgs boson will be a fundamental test for the mechanism of electroweak symmetry-breaking predicted within the Standard Model.

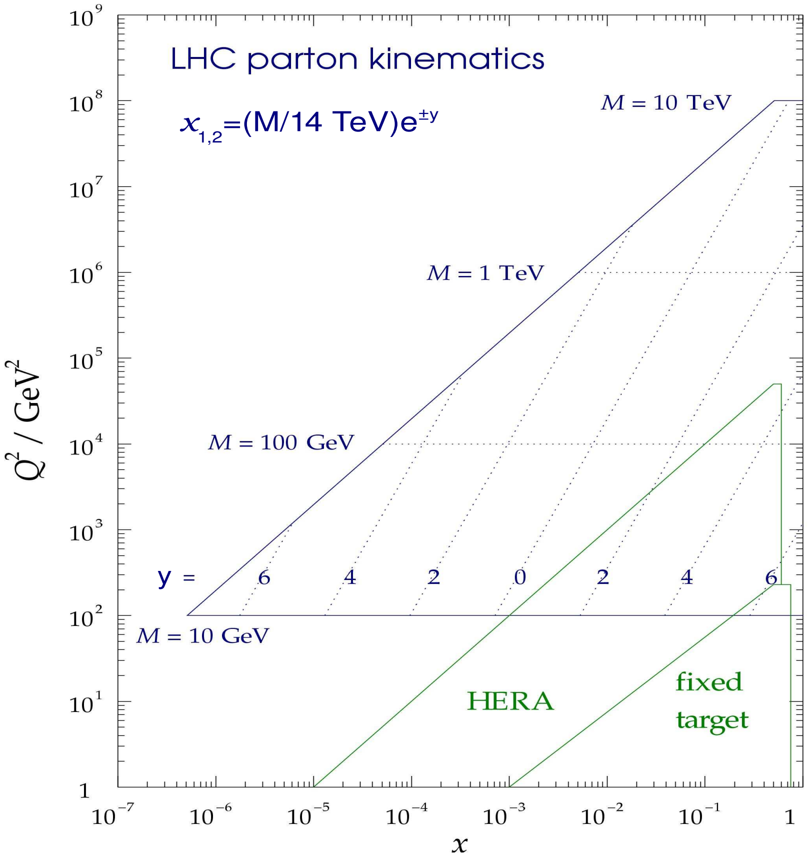

Figure 1.4: Parton kinematics at LHC. Coverage of the (x,Q^2) kinematic plane for the production of a particle of mass M by HERA and LHC [16].

- Measurements of W boson and top quark mass. The W and top masses are the important parameters in the Standard Model. These measurements will be important for consistency checks of the Standard Model. The high statistics provided by the LHC should allow one to measure the W mass with an accuracy better than $\Delta m_W \approx 15$ MeV and top mass with accuracy better than $\Delta m_t \approx 1$ GeV [32] in one year of running at low luminosity (for 10 fb^{-1}) .

- B-Physics. The programme for B-physics will include precise measurements of the CP violation in B-meson decays, measurements of the flavour oscillations in B_s^0 as well as B_d^0 mesons.

- Searches for physics beyond the SM. The experimental signatures predicted by the physics beyond the SM will be intensively investigated in ATLAS. Important signs for the new physics will be the large missing transverse energy E_T^{miss} (*e.g.* in case of the presence of extra dimensions or SUSY) and different jet topology in the event (*e.g.* compositness, mini-black holes). The main problems are expected in separation of the effects coming from the new physics and their assignment to one or another

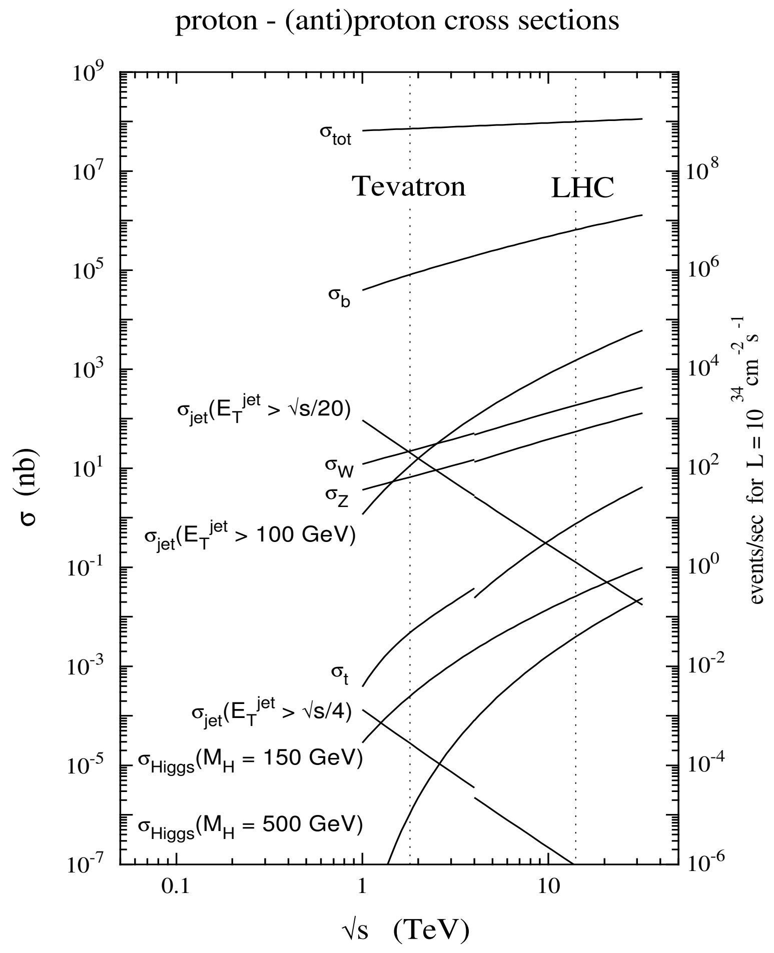

Figure 1.5: Cross-sections for various processes as a function of the cms energy [34].

theory. Another source of problems could be the instrumental effects of the detector.

The total pp cross-section at LHC can be written as:

$$\sigma_{tot} = \sigma_{el} + \sigma_{inel}, \tag{1.18}$$

where σ_{el} is the cross-section of the elastic processes and σ_{inel} is the inelastic cross-section. The expected value for total cross-section at $\sqrt{s} = 14$ TeV is $\sigma_{tot} \approx 107$ mb [31] and for inelastic cross-section $\sigma_{inel} \approx 70$ mb.

The production event rate of physics processes at a given energy is dependent on the two factors: the cross-section of the physics process at a given energy and the luminosity:

$$R = \sigma \times \mathcal{L}, \tag{1.19}$$

where R is production event rate, σ is production cross-section usually expressed in barns [3], $\mathcal{L}$ is luminosity per bunch-crossing.

Figure 1.5 shows the expected cross-sections and rates for various SM processes as a function of the center-of-mass energy calculated at NLO order. High production cross-sections for many important processes will allow to increase the accuracy of measurements

---

[3] 1 barn=$10^{-24}cm^2$

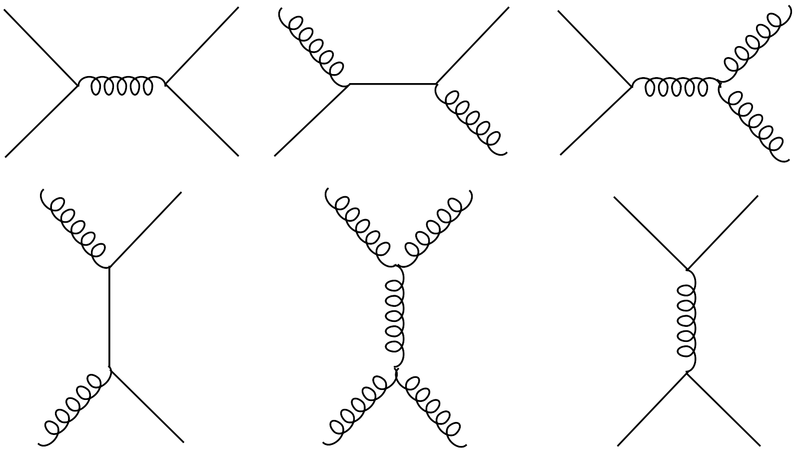

Figure 1.6: Leading order 2→ 2 diagrams for various QCD jet production processes.

and to test the SM more precisely. For example one expects the production of 10^{13} $b\bar{b}$, 8×10^6 $t\bar{t}$ pairs, 10^4 jets with E_T higher than 1 TeV per year at low luminosity (10 fb^{-1}). The statistics will be limited only by the rate at which data can be recorded. Before being recorded the data has to be selected by the trigger which performs the selection based on the information coming from the ATLAS detector. The difference between the total cross-section and the cross-section of the interesting physics is in many cases greater than ten orders of magnitude and requires highly efficient and selective trigger.

Thus, the primary tasks will be the understanding of trigger and detector performance as well as the background expected in the "discovery" channels and rediscovery of SM processes.

1.3 Jet physics

Quarks and gluons produced by hard scattering event can not be observed directly due to colour confinement. What is observed is a jet of hadronic particles whose direction and total energy correlate with that of the produced quark or gluon. Jet signatures are of decisive importance for many studies in the ATLAS physics programme. In the following sections the basics of jet production will be discussed.

1.3.1 Jet production at LHC

In section 1.1.2 the hard component of the hadron-hadron collision was discussed. In this section the general hard scattering event topology is outlined including the contributions coming from dominating soft processes and their influence on the jet finding procedure. We consider the inclusive dijet production process is defined by the reaction:

$$h_1 + h_2 \rightarrow jet + jet + X, \tag{1.20}$$

where X represents everything else produced. Some 2-to-2 leading order (LO) diagrams for various scatterings between quarks and gluons are shown in Figure 1.6. The LO diagrams make a dominant contribution to the jet production when the jet transverse momentum is large. The process of dijet production is sketched in Figure 1.7. The hard collision of two incoming partons is the process of particular interest, where one has the possibility to

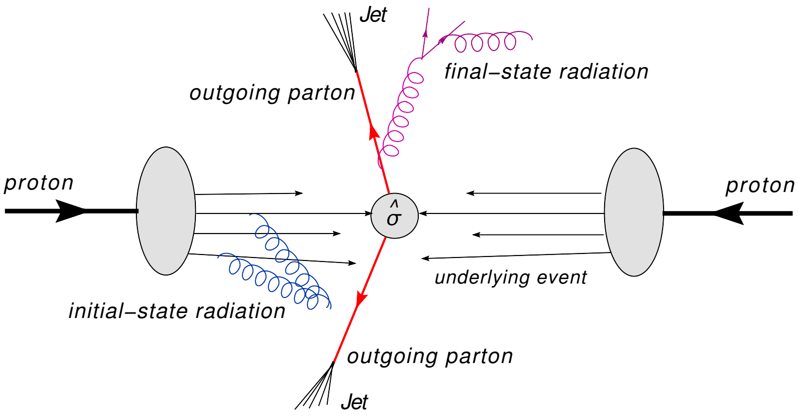

Figure 1.7: Inclusive jet production in the process $h_1 + h_2 \to jet + jet + X$, where X represents everything else produced.

study matter at a very short distances. In this process two partons are scattered at wide angles after passing very close to each other. As a result high p_T outgoing partons are produced, which hadronise, and are observed as jets of the particles later on. Along with hard production, the rest of the particles in the event is produced by soft processes. The soft parts of the hadron-hadron collision can be subdivided in a few main categories:

- **Initial state radiation (ISR).** Any of the incoming partons can start off a sequence of branchings such as $q \to qg$, which produces an initial-state radiation shower.

- **Final state radiation (FSR).** A similar process to ISR, which takes place for the outgoing partons before they hadronise.

- **Underlying event.** The partons not involved in the hard interaction scatter with small angles respectively with small p_T. These partons are associated to the underlying event (UE). The underlying event plus the ISR produce the so-called beam remnants.

- **Multiple interactions.** These are soft inelastic interactions of the beam remnants. Multiple interactions contribute to the underlying event.

- **Minimum bias events**[4]. Minimum bias events do not contain hard scattering process and are characterised by low p_T of the produced particles. In the high luminosity running regime any hard scattering collision at LHC at nominal luminosity is expected to be accompanied by ~ 23 additional soft inelastic collisions coming within one bunch-crossing. These additional collisions are minimum bias events. They are "piled up" in each bunch-crossing, this effect is known as event pile-up.

The clear understanding of these soft processes is important for the correct measurement of the high p_T hard scattering partons. However, the presence of the softer interactions and final hadronisation of all color-connected constituents of the event prevent us from direct and exact measurement of the p_T of the outgoing partons from hard scattering

---

[4] Minimum bias events term comes from the fact, that these events are accepted with totally inclusive trigger , without any cuts or biases applied.

process. What is accessible for measurement is the collimated bundle of particles (mainly hadrons) called jet, which has finally reached the detector.

Various algorithms can be applied to the measured objects or to the final states in theoretical calculations in order to identify a jet and associate it uniquely to the outgoing parton. Jet algorithms are divided into two main categories:

- The K_T algorithm.
- The cone algorithm.

1.3.2 Jet algorithms and finding procedures

The task of a jet algorithm is to combine the final state objects into jets such that the kinematic properties of the jets (*e.g.* momenta) can be related to the corresponding properties of the energetic partons produced in the hard scattering process. The jet algorithm can be applied to different objects depending on the level of consideration. These levels can be summarised as follows:

- **Detector level (data or Monte Carlo with detector simulation):** Energy deposits in the calorimeter cells typically summed up within the calorimeter towers which are used as the basic elements of the clustering.
- **Particle or hadron level (Monte Carlo):** Stable particles (e.g., hadrons) are the basic elements to be clustered.
- **Parton level (Monte Carlo):** Partons before hadronisation are clustered into jets. For Monte Carlo programs such as HERWIG or PYTHIA this will include many quarks and gluons from the parton shower and the multiple parton interactions.

The essential attribute of the jet algorithm is applicability and equal behaviour at any level of consideration:

- Theoretical calculations (final state particles, partons).
- Experimental data (signals in calorimeter cells).

This attribute means that the algorithm should find the same jets at the parton, particle, and detector level. Therefore it must not introduce any bias in the analysis based on comparison of experimental data to the theoretical predictions or simulations. Before coming to the technical implementation it is important to summarise other important characteristics of the jet algorithm. The perfect jet algorithm should be [24]:

- Fully specified: The jet selection process, the jet kinematic variables and the various corrections should be clearly and completely defined.
- Theoretically well behaved: the algorithm should be infrared and collinear safe at all orders of perturbative calculations.
- Invariant under boosts: This is important for hadron-hadron colliders where the c.m. frame of the individual parton-parton collisions is typically boosted with respect to the hadron-hadron cms frame.

- Detector Independent: There should be no dependence on cell type or size.
- Easy to calibrate.
- Suppression of soft processes: *e.g.* the processes which are related to beam remnants etc.

The first item in the list requires the exact specification of the jet algorithm at all operational stages. The second item implies that an algorithm is infrared safe if, for any n-parton configuration, adding an infinitely soft parton does not affect the jet algorithm results at all. And an algorithm is collinear safe if, for any n-parton configuration, adding and replacing any massless parton by an exactly collinear pair of massless partons does not affect the algorithm results at all. The last three items are basically related to the experimental properties of the algorithm. They can be fully analysed and understood only by certain running conditions.

Various jet algorithms are implemented in the ATLAS experiment. In the following subsections the two jet algorithms mostly used in ATLAS physics analysis and their basic properties will be discussed. These algorithms are iterative seeded cone and the K_T algorithm.

1.3.3 The cone algorithm

The algorithm selects the objects close to each other in angle and then combines them to form the momentum of the jet.

The algorithm proceeds as follows:

1. In the list of jet constituents (partons, towers, particles) find the constituents which have E_T higher than defined threshold E_T^{Seed} (typically 1-2 GeV) and mark them as seeds *i.e.* the initiator points for the algorithm.
2. For each seed define a cone with radius R and geometric center (η^C, ϕ^C) in $\eta \times \phi$ space.
3. Select all the constituents i within the cone:
$$\sqrt{(\eta^i - \eta^C)^2 + (\phi^i - \phi^C)^2} \leq R. \tag{1.21}$$
4. Calculate the jet variables $p^J = (E^J, \mathbf{p^J})$, p_T^J, η, ϕ using the four-vector sum recombination scheme[5].
5. Compare the geometric center (η^C, ϕ^C) with the calculated jet center (η^J, ϕ^J)
6. If the geometric center coincides with the jet center *i.e.* difference < 0.05, consider the jet as stable, return to step 2 and proceed with the next seed. If not - go to the next step.
7. Define a new cone with radius R and geometric center (η^J, ϕ^J). And repeat all the steps starting from step 3. The algorithm iterates until the cone geometric center matches the jet center.

---

[5] Recombination scheme means a rule of addition of constituent momentum to the jet.

The jets found by the cone algorithm can overlap with each other and share energy. To resolve this problem a split/merge procedure must be applied to bring the stable jets obtained after iterations to the final jets. Typically cones whose shared energy is larger than a fixed fraction (for ATLAS $f = 50\%$) of the energy in the lower energy cone are merged, otherwise the shared components are associated to the closest jet.

1.3.4 The K_T algorithm

The K_T algorithm starts with a list of preclusters which are formed from calorimeter towers, particles, or partons. The algorithm successively merges pairs of preclusters in order of increasing relative transverse momentum.

Initially for each precluster a four-momentum vector is assigned. The K_T algorithm begins with a list of preclusters as defined above and an empty list of final jets to be filled. It then proceeds recursively as follows:

1. For each precluster i in the list, define

$$d_i = p_{T,i}^2. \tag{1.22}$$

2. For each pair (i, j) of preclusters $(i \neq j)$, define

$$d_{ij} = min(p_{T,i}^2, p_{T,j}^2)\frac{[(\eta_i - \eta_j)^2 + (\phi_i - \phi_j)^2]}{D^2} \tag{1.23}$$

   where $D \approx 1$ is a parameter of the jet algorithm which controls the termination of merging and designates the size of resulting jets.

3. Find the minimum of all the d_i and d_{ij} and label it d_{min}.

4. If d_{min} is a d_{ij}, merge preclusters i and j into a new precluster $(E_{ij}, \mathbf{p_{ij}})$ with:

$$E_{ij} = E_i + E_j, \tag{1.24}$$

$$\mathbf{p_{ij}} = \mathbf{p_i} + \mathbf{p_j}. \tag{1.25}$$

5. If d_{min} is a d_i, the corresponding precluster i is "not mergable". Remove it from the list of preclusters and add it to the list of jets.

6. Go to step 1.

The procedure continues until there are no more preclusters. The algorithm produces a list of jets, each separated by:

$$\sqrt{(\eta_i - \eta_j)^2 + (\phi_i - \phi_j)^2} > D \tag{1.26}$$

In figure 1.8 the successive merging procedure of K_T algorithm is depicted. As was described, the K_T algorithm starts with a list of preclusters which are schematically shown in the left picture, and applying the merging procedure ends with a list of final jets in the right picture. The K_T algorithm, based on the preclustering scheme is infrared or collinear safe to all orders of calculation, so one may conclude that it is theoretically well behaved [21].

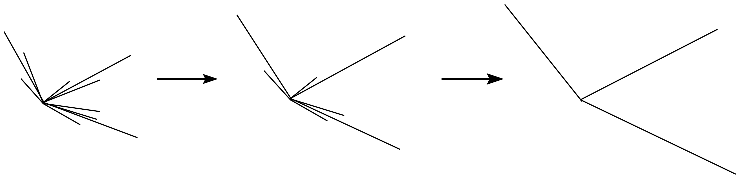

Figure 1.8: A simplified example of the successive iterations of the K_T algorithm.

1.3.5 Comparison of K_T and cone algorithms

The main characteristics for the K_T and cone algorithms can be summarised in the following lists:

$\mathbf{K_T}$ algorithm

- Infrared and collinear safe.
- No overlapping problem.
- Can have complex boundaries in η, ϕ coordinates.
- Relative slow.[6]

Iterative seeded cone algorithm

- Smooth, simple jet shape.
- Overlaps between jets possible.
- Problems with collinear and infrared safeness.
- Must find seeds, may miss jets.
- Relatively fast.
- Effective in underlying event rejection.

The choice of the algorithm depends on the event structure. An obvious example is the difference between e^+e^- collisions and hadron-hadron collisions.

If we look at an e^+e^- event in which hard scattering occurs, we will see that any of the final state particle belongs to the hard scattering process because of the absence of an underlying event and ISR. The jet definition that associates every final-state particle with one of the jets was used in that case based on the K_T algorithm [22, 20].

In hadron-hadron collision, the presence of the UE and ISR gives rise to the significant fraction of final state particles which do not belong to the hard scattering. In order to distinguish high p_T jets coming from hard scattering from so-called beam jets originating from beam remnants, the cone algorithm [23] is typically used.

Comparing to the seeded cone algorithm, the K_T is theoretically well behaved. *E.g.* if a parton divides into two partons with collinear momenta, then the algorithm immediately recombines them, producing the same result as if the parton had not divided. That means it is collinear safe. The K_T algorithm also does not have overlapping problem as it uniquely assigns each precluster to only one jet. The main concern for the K_T algorithm, which

---

[6] The K_T algorithm is an $\mathcal{O}(n^3)$ algorithm, i.e. for n particles $\sim n^3$ calculations are required.

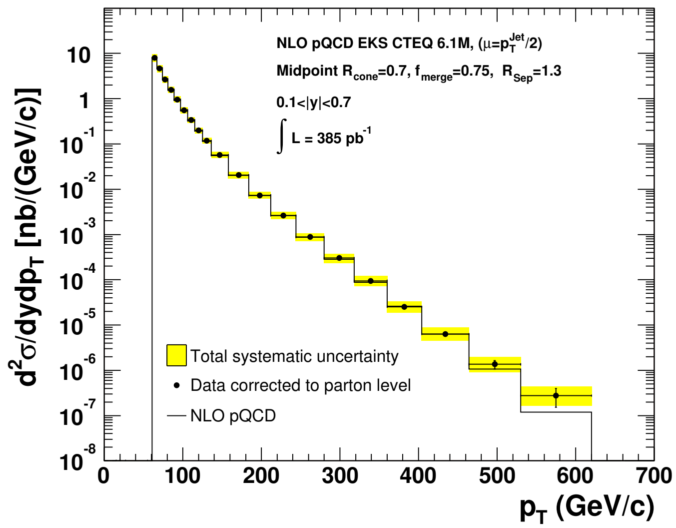

Figure 1.9: Measured inclusive jet differential cross-section corrected to parton level compared to the NLO pQCD [28].

should be treated carefully is the complex boundaries. The complex boundary shape comes from the fact that particles with very small E_T can be very far from the jet axis. The energy coming from the underlying and pile-up event can be added to the K_T jets. This leads to a complication for the K_T calibration procedure, namely the subtraction of the UE and pile-up energy from the jet. The details of the K_T jet momentum calibration and successful implementation of the calibration procedure, which was performed in the D0 experiment can be found in [26].

Seeded cone algorithms suffer from problems due to infrared sensitivity. An example of infrared sensitivity is soft radiation between two jets which can cause merging. Another problem is collinear sensitivity where for instance the energy is split between multiple objects and algorithm is failing to produce a seed. However, this effect is significantly reduced for larger E_T jets. The modification of the seeded cone algorithm is a seedless cone algorithm. It does not have infrared and collinear problems but is expensive in computer time. Another algorithm called "midpoint" is also based on the seeded cone algorithm [27]. The algorithm adds additional seeds using the midpoints of all pairs of the jets found by the seeded cone algorithm. The midpoint algorithm is free from the infrared sensitivity and does not need too much computer time with respect to the seedless cone algorithm.

1.3.6 Inclusive jet cross-section

Hadronic jet production at high energy colliders has proved to be one of the most valuable testing-grounds for Quantum Chromodynamics in an energy regime never probed before. At hadron colliders one of the most important measurements is the determination of the inclusive transverse energy spectrum of jets. Whereas at e^+e^- colliders, where the all final state particles come from interaction of interest, at hadron-hadron collider the final state particles come from hard scattering process present only a small fraction from the total

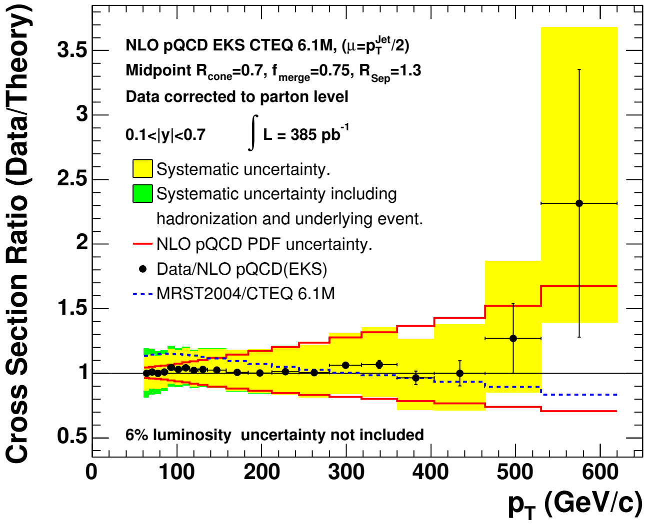

Figure 1.10: The ratio of the data corrected to parton level over the NLO pQCD prediction of the EKS calculation using CTEQ6.1M in central the rapidity region [28].

number of particles originating from the UE pileup events. That is why at hadron-hadron colliders the choice is done in favour of inclusive jet cross-section, that is, cross-section to produce exactly n jets, usually one or two leading [7] jets with specified properties plus any number of other jets or particles.

The inclusive jet cross-section measured by the CDF Collaboration is shown in Figure 1.9. The midpoint algorithm was used for this measurement. The theoretical calculations are carried on using the EKS (Ellis, Kunszt and Soper) NLO QCD program [29]. The comparison to next-to-leading order (NLO) calculations with data corrected to parton level shows good agreement within the experimental systematic uncertainties, denoted as yellow band.

A detailed comparison on a linear scale between inclusive jet cross-section and NLO theoretical predictions together with systematic theoretical and experimental uncertainties is depicted in Figure 1.10. The plots show that theoretical predictions done using CTEQ6.1 and MRST2004 PDFs are in reasonable agreement with the experimental results.

The PDF uncertainty is the dominant theoretical uncertainty in the whole transverse momentum range. A significant fraction of PDF uncertainty comes from the gluon distribution uncertainties at large x values.

The main contribution to the systematic error is coming from the absolute Jet Energy Scale (JES). JES defines the correct energy of the jet at different levels of consideration (parton, particle or calorimeter level) based on the measured calorimeter jet energy. The JES is expected to be the main source of systematic uncertainty for jet cross-section measurements also at LHC. The expected statistical uncertainties on the jet cross-section will be small. It is important to emphasise that the JES determination will be the challenging task at LHC. The desired goal of an overall systematic uncertainty below ±1% on the JES requires clear understanding of the detector performance, physics effects, *e.g.* algorithm dependance and calibration procedure.

---

[7] Leading jet in an event refers to the jet with the highest transverse energy E_T.

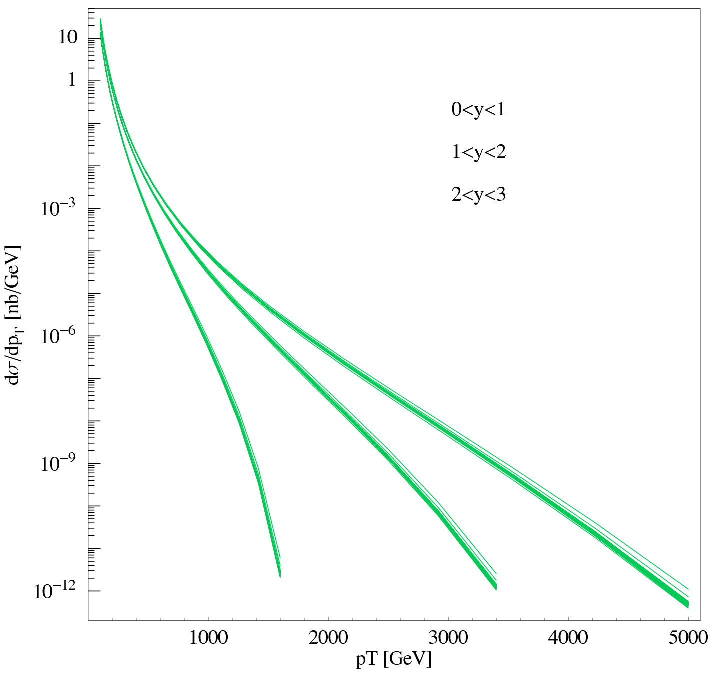

Figure 1.11: The prediction for inclusive jet cross-section for LHC using the CTEQ6.1 PDF set with error estimates [30].

In Figure 1.11 the inclusive jet cross-section predictions for three different rapidity regions is depicted. Due to the high jet production rate at LHC, the cross-section can be measured over many orders of magnitude up to very large transverse momentum $\sim$ 5 TeV in the central rapidity, at relatively short time scale. This will allow rather stringent limits on potential deviations from the Standard Model. New physics, *e.g.* quark compositness is expected to show up as an excess of events at high p_T compared with pQCD. Measurement of the inclusive jet cross-section will also be a fundamental test of perturbative QCD predictions.

Chapter 2

The ATLAS experiment

2.1 The LHC storage ring

The LHC machine will be operated in the proton-proton collision mode at the never before reached center-of-mass energy of $\sqrt{s}$=14 TeV, while colliding heavy ions such as lead (Pb) LHC will reach a cms energy per nucleon pair of $\sqrt{s}$=5.5 TeV. The LHC is constructed in the circular former LEP (Large Electron Positron) tunnel at CERN.

The 27 km ring will host 1232 superconducting dipole magnets (each is 15 m long), 386 quadrupoles and many thousands ($\sim$ 6000) of correcting magnets. The two vacuum chambers carrying protons circulating in opposite directions are integrated into a two-in-one magnet cryostat, in order to fulfill the economical constraints and limited space conditions in the tunnel. The Radio-Frequency (RF) system of the LHC which uses superconducting cavities will be used to capture, accelerate and store the injected beam.

The dipole magnets are applied for beam steering, providing a 8.33 T bending magnetic field for the 7 TeV proton beams. The function of the quadrupoles is to focus the beam. The magnets should be brought down to the temperature of 1.9K by the cryogenic system to operate in the superconducting state.

The LHC will be supplied with protons and Pb ions from the existing injector chain at CERN comprising LINAC (LINear ACcelerator, PS (Proton Synchrotron) and SPS (Super Proton Synchrotron). The protons, after several stages of acceleration, achieve 450 GeV energy and are finally injected from the SPS into the LHC ring via two transfer lines TI2 and TI8 and are accelerated to 7 TeV energy per beam. An overview of the CERN accelerating facilities is given in Figure 2.1.

The LHC will provide proton-proton collisions with a design luminosity of $10^{34}cm^{-2}s^{-1}$, and heavy (Pb) ion collisions with a nominal luminosity of $10^{27}cm^{-2}s^{-1}$. The luminosity can be expressed as:

$$\mathcal{L} = \frac{f n_b N_1 N_2}{A_{int}}, \tag{2.1}$$

where f is the beam revolution frequency (11.25 kHz), N_1 and N_2 are the numbers of protons in the colliding bunches, and A_{int} is the interaction area assuming a Gaussian beam profiles at the interaction point (IP).

Starting from 1 % of design luminosity in the commisioning phase, the LHC will be brought to the initial phase of running with a luminosity of $10^{33}cm^{-2}s^{-1}$ which is also referred to as low luminosity phase. In the third year of running the LHC will reach the high luminosity of $10^{34}cm^{-2}s^{-1}$. To achieve the design luminosity of $10^{34}cm^{-2}s^{-1}$, 2808 bunches of 10^{11} protons each have to be stored. The bunches are grouped into

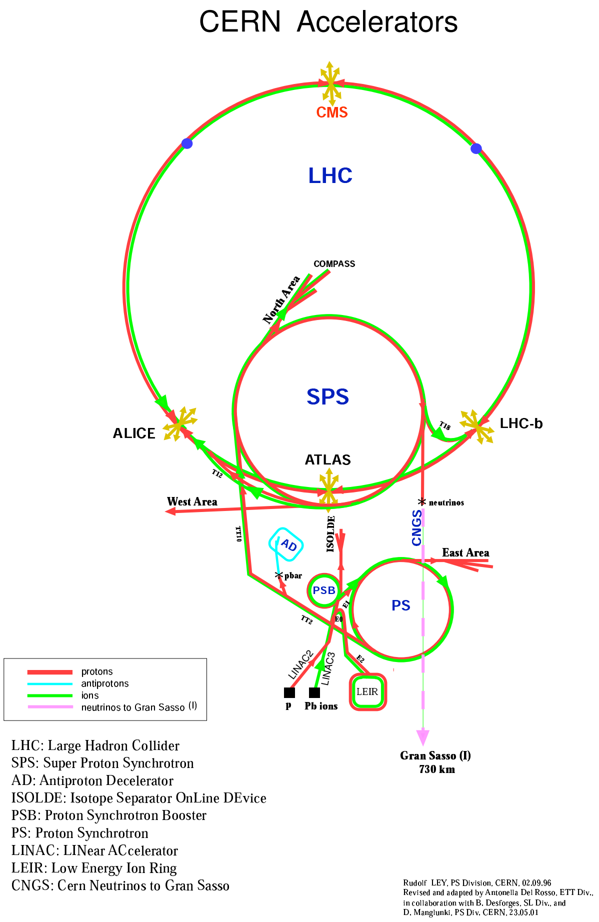

LHC: Large Hadron Collider
SPS: Super Proton Synchrotron
AD: Antiproton Decelerator
ISOLDE: Isotope Separator OnLine DEvice
PSB: Proton Synchrotron Booster
PS: Proton Synchrotron
LINAC: LINear ACcelerator
LEIR: Low Energy Ion Ring
CNGS: Cern Neutrinos to Gran Sasso

Rudolf LEY, PS Division, CERN, 02.09.96
Revised and adapted by Antonella Del Rosso, ETT Div.,
in collaboration with B. Desforges, SL Div., and
D. Manglunki, PS Div. CERN, 23.05.01

Figure 2.1: Overview of the CERN accelerating facilities.

"trains" of 81 bunches, which in turn are grouped into 12 batches each containing three bunch trains. The distance between two bunch trains is expected to be about 38 bunch-crossings. The bunch-crossing interval will be 25 ns and the total energy stored per beam will be around 350 MJ. The luminosity lifetime is estimated to be approximately 10 hours (after 10 hours only 1/3 of initial luminosity). The basic performance parameters for the LHC nominal p-p operation mode are shown in Table 2.1.

At high luminosity the effect of pile-up starts to play a significant role. The contributions to pile-up come from two main sources:

- The number of minimum bias events per bunch-crossing at high luminosity is ~ 23. For each interesting event selected by the trigger, on average there will be signals from 23 proton-proton collisions superimposed in the detector.
- The long detector response, several hundred nanoseconds (up to 500 ns), makes the detector sensitive to the events coming from many bunch-crossings. That means that signals from about 20 bunch-crossings are superimposed.

The effect of pile-up has a large impact on the detector design. Fast detector response and fine readout granularity to keep the channel occupancy low are required to decrease the pile-up effect.

Table 2.1: The nominal LHC parameters for high luminosity operation mode [36].

parameter	**value**
Proton energy	7 TeV
Dipole field	8.33 T
Number of bunches	2808
Number of particles/bunch	1.15×10^{11}
Bunch spacing	24.95ns (7.5m)
RMS bunch length	7.5cm
RMS beam size at IP	16.7 μ m
Crossing angle	285 μ rad
Peak luminosity	10^{34}
Stored energy per beam	362 MJ

Four large-scale collaborations will operate detectors in different points around the LHC. ATLAS and CMS are multi-purpose detectors with a broad physics programme, ranging from the search for the Higgs boson to supersymmetric particles. The LHCb experiment is dedicated to the physics of b-hadrons produced at the LHC in order to make precision studies of CP asymmetries and of rare decays in the B-meson system [37]. The aim of the ALICE experiment is high-energy heavy-ion physics [38]. It will study strongly interacting matter at extreme energy densities, in particular the formation of the Quark-Gluon Plasma (QGP).

2.2 The ATLAS detector

ATLAS (A Toroidal LHC ApparatuS) is a general purpose pp detector which is designed to exploit the full discovery potential of LHC. The major focus of interest of ATLAS is the discovery of the Higgs boson in a wide mass range. Other important goals are searches for supersymmetric particles, for compositeness of the fundamental fermions, as well as the investigation of CP violation in B-decays and precise measurements masses of $W-$, $Z-$ bosons and top quark mass (see Section 1.2). The main experimental signatures at ATLAS will come from the measurements of electron, photon, muon, jet, determination of missing transverse energy E_T^{miss} and b-quark tagging. The most important design requirements for ATLAS detector imposed by the physics goals are:

- The ATLAS detector should have fast, radiation hard electronics (in particular in the tracking system), and high detector cell granularity to reduce the effect from pile-up.

- The triggering system should be fast and efficient.

- Large acceptance in pseudorapidity η with full azimuthal ϕ angle coverage is required.

- Efficient tracking also at high luminosity for high-p_T lepton-momentum measurements.

- ATLAS calorimetry should provide precise electron and photon identification and accurate measurements of jet energy and determination of missing transverse energy.

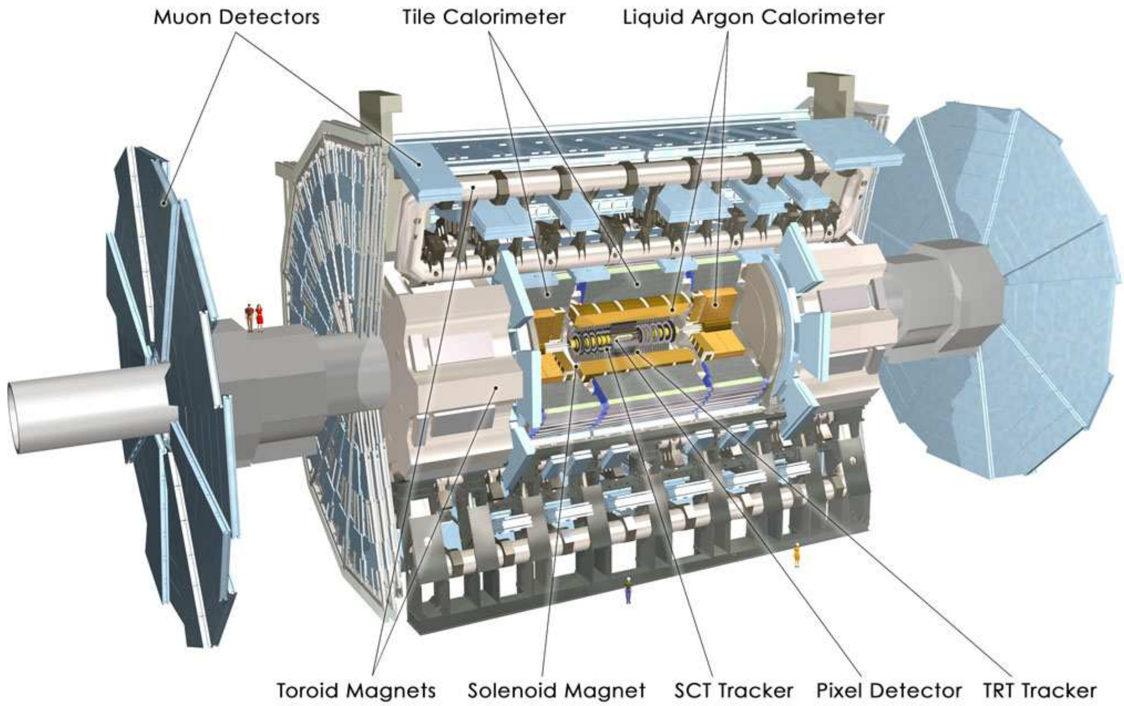

Figure 2.2: Overall layout of the ATLAS detector [39].

- Good muon identification and momentum resolution over a wide range of momenta.

The overall detector layout is given in Figure 2.2. The main ATLAS detectors are:

- **Inner Detector**
  - Pixel detector
  - Semiconductor tracker
  - Transition radiation tracker
- **Calorimeter**
  - Electromagnetic calorimeter (Liquid Argon Calorimeter)
  - Hadronic calorimeter
- **Muon spectrometer**

The Inner Detector (ID) is contained within a cylinder of length 7 m and radius of 1.15 m, in a solenoidal magnetic field of 2 T. The full tracking coverage is $|\eta| \leq 2.5$. The magnetic field for ID is provided by the a central solenoid (CS) which is a part of the superconducting magnet system.

The ID is followed by the liquid argon (LAr) electromagnetic sampling calorimeter which covers the pseudorapidity region $|\eta| < 3.2$. The LAr calorimetry is embedded in cryostat cylinder with outer radius of 2.25 m and length of 6.8 m along the beam axis. The ATLAS hadronic calorimeters cover the range $|\eta| < 4.9$. The hadronic barrel calorimeter extends from an inner radius of 2.28 m to an outer radius of 4.25 m and is 11.44 m long.

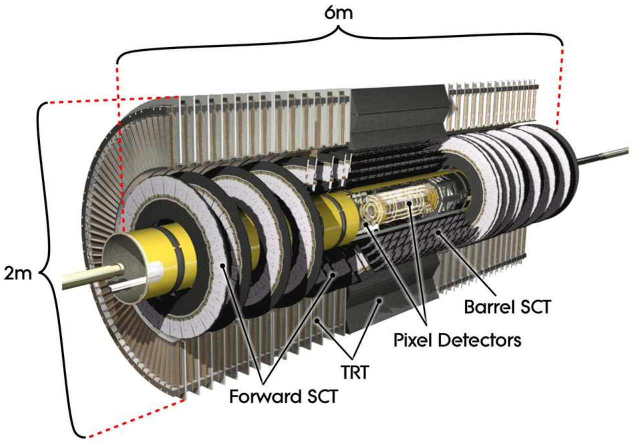

Figure 2.3: Inner Detector view. It consists of two high resolution detectors at the inner radii (Pixel Detector and Semiconductor Tracker) and continuous tracking elements (Transition Radiation Tracker) at the outer radii [39].

The ATLAS detector ends up by a huge muon system with acceptance $|\eta| < 2.7$. This muon system makes the ATLAS setup very large with a length of 46 m and a diameter of 25 m. In the following sections a description of the main ATLAS subsystems will be given.

2.2.1 Inner detector

A three-dimensional view of the layout of the Inner Detector is shown in Figure 2.3. The Inner Detector consists of high-resolution detectors at inner radii (up to 56 cm) with continuous tracking elements at outer radii, all contained in a CS. Mechanically, the Inner Detector consists of three units: a barrel part over ±80 cm, and two identical end-caps. In the barrel, the high-precision detector layers are arranged on concentric cylinders around the beam axis in the region with $|\eta| < 1$, while the end-cap detectors are mounted on disks perpendicular to the beam axis.

The Semiconductor Pixel Detector is closest to the IP. It is designed using silicon pixel technology to provide a high-granularity, high-precision set of measurements close to the interaction point. The readout chips are connected to the pixel elements using “bump bonding” technology which provides high density of readout channels $\sim 140 \times 10^6$. In the pixel detector at radius 11 cm, a radiation dose of 25 kGy/year at high luminosity is expected. The high radiation level requires the replacement of the detector after a few years depending on the luminosity profile.

The Semiconductor Tracker is designed as a silicon microstrip detector and provides four precision measurements per track in the intermediate radial range. The detector contains 61 m^2 of microstrip detectors, with 6.2 million readout channels. The spatial resolution provides a tracks separation by more than ~ 200 μm.

The precision tracking elements are contained within a radius of 56 cm, followed by the continuous tracking elements.

The Transition Radiation Tracker is based on the use of straw tube detectors. The TRT provides a large number of tracking points (about 36 per track), thus precise track measurement. The barrel TRT straws ($\sim$ 100000) are parallel to the beam direction, while end-caps contain 320000 radial straws. The total number of electronic channels is 420000 [40].

The combination of the two silicon and TRT techniques gives a very robust pattern recognition and high precision in both ϕ and z coordinates.

2.2.2 Calorimetry

Calorimeters are widely used in modern high-energy physics experiments. The basic function of the calorimeters is the measurement of the energy and position of the incident particles or jets. Calorimeter systems are usually constructed of calorimeters of different types, for optimal performance on different incident particles.

Calorimeters will play a crucial role in ATLAS. The main tasks of the ATLAS calorimeter are: accurate measurement of the energy and position of electrons and photons, energy and direction of jets and determination of missing transverse energy. The interactions of incident charged or neutral particles with matter in most of the cases result in the development of particle showers which are divided into two types: electromagnetic and hadronic. Before coming to the calorimeter instrumental description, the main parameters and characteristics of the electromagnetic and hadronic showers will be shortly outlined in the following two sections.

Electromagnetic showers

When high energy particle (e^-, e^+ or γ) penetrates matter it invokes an electromagnetic cascade mainly via two processes: bremsstrahlung for the charged particles and pair production for the photons. Starting from the incident particle the number of particles is increasing, while the average energy of the shower particles decreases. This multiplication process continues until the energy per particle becomes equal to the critical energy ϵ_c. The critical energy can be defined as the energy at which the energy losses from radiation (bremsstrahlung) equal those from ionisation. At this point the shower reaches its maximum and starts to decline. The profile of an electromagnetic shower is usually described by two variables:

- **Radiation length** X_0 for longitudinal development. The radiation length is defined as a mean distance over which a high energy electron or positron loses about 63.2% or (1-e^{-1}) of its energy by bremsstrahlung. The radiation lenth is applied in order to describe shower parameters independently from material type.
- **Molière radius** p_M for the lateral development. Molière radius is related to radiation length and critical energy ϵ_c as:

$$p_M = 21.2\ MeV \times \frac{X_0}{\epsilon_c} \tag{2.2}$$

Approximately a 90% of the shower energy is contained within a cone with radius p_M around the shower axis.

Hadronic showers

The incident hadron strongly interacts with the medium producing a number of hadrons, and so on. The charged hadrons ionise the medium on the path till they undergo strong

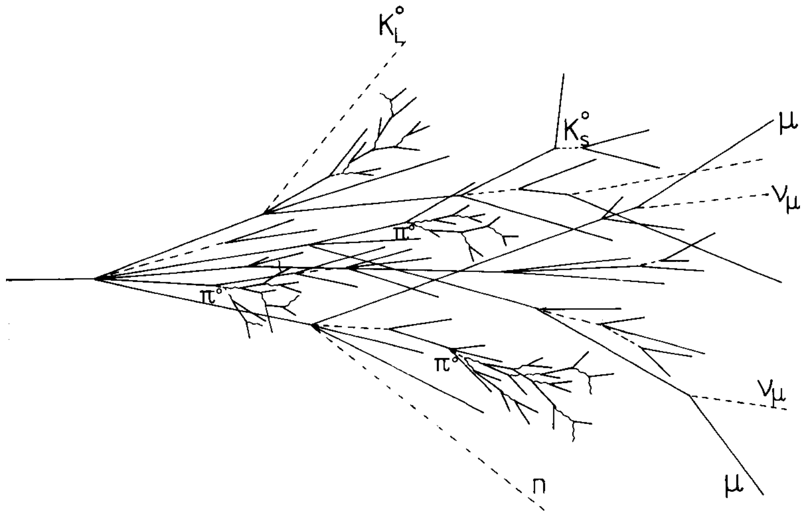

Figure 2.4: Example of a hadronic shower [41].

interaction with nuclei. As a result of electromagnetic and strong interactions in hadron showers a large number of different particle (electrons, positrons, photons, neutrons, protons etc.) may be produced during the shower development. Thus the structure of the hadronic shower is much more complicated than the structure of the electromagnetic one. An example of the hadronic shower is drawn in Figure 2.4.

The hadronic shower can be divided very roughly in the following components:

- **Detectable electromagnetic component** ($\mathcal{O}$ (50%)). The main contribution to this component comes from π_0 decays $\pi_0 \to \gamma\gamma$.
- **Detectable non-electromagnetic component** $\mathcal{O}$ (25%). Ionisation losses by charged hadrons (p, $\pi^{\pm}$ μ etc.).
- **Undetectable non-electromagnetic component** ($\mathcal{O}$ (25%)).Inelastic nuclear collisions contribute to the non-electromagnetic component. This component can not be measured in the calorimeter and remains undetectable.
- **Escaped energy** ($\mathcal{O}$ (2%)). Contribution from neutrinos.

The presence of the non-electromagnetic invisible component in hadronic showers makes the calorimeter response to the hadrons smaller than to electrons. In practice this fact can be expressed as follows:

$$e/h > 1, \tag{2.3}$$

where e is the calorimeter electromagnetic response and h is the hadronic response. The definition for calorimeter response which is used here and later is:

- **Calorimeter response** is the ratio of the average calorimeter signal to the energy of the particle, which initiates this signal.

The calorimeters to which the criteria $e/h > 1$ can be applied are called non-compensating. The ATLAS calorimetry is non-compensating by design. The degree of non-compensation is defined by the value e/h. Experimentally the value e/h can not be measured and is

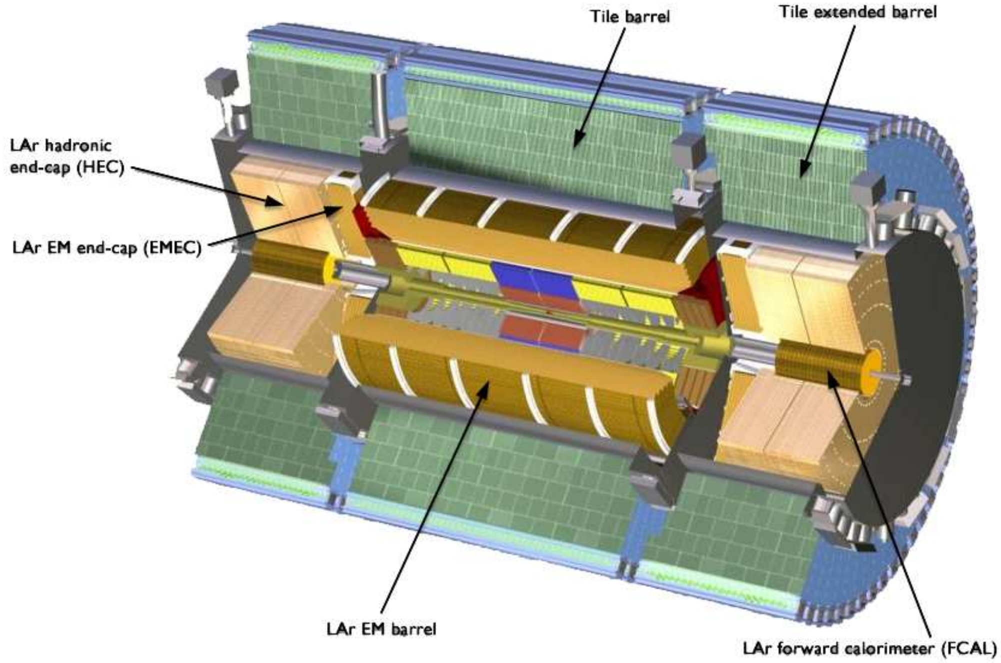

Figure 2.5: Atlas calorimetry [39].

derived from the measured e/π signal ratios. By π is the calorimeter response to pions is implied.

Calorimeter layout

The overall ATLAS calorimeter layout is given on Figure 2.5. The ATLAS calorimeter consists of two parts: the electromagnetic (em) and hadronic calorimeter.

- **The electromagnetic** calorimeter covers the rapidity region $|\eta| < 3.2$ and includes:
  - the barrel em calorimeter – $|\eta| < 1.475$
  - the endcap em calorimeter – $1.375 < |\eta| < 3.2$
- **The hadronic** calorimeter covers the rapidity region $|\eta| < 4.9$ and comprises:
  - the barrel and extended hadronic calorimeters – $|\eta| < 1.7$
  - the end-cap hadronic calorimeters – $1.5 < |\eta| < 3.2$
  - the forward calorimeters – $3.1 < |\eta| < 4.9$

The barrel em calorimeter is contained in the barrel cryostat together with the Inner Detector, the solenoid coil and the presampler detector. The barrel cryostat is 6.8 m long, with an outer radius of 2.25 m, and an inner cavity radius of 1.15 m. Two end-cap cryostats separated by 9.5 cm in space from the barrel cryostat contain the end-cap LAr electromagnetic and LAr hadronic calorimeters, as well as the forward calorimeter. Radially, ATLAS calorimeter ends up with the Tile Calorimeter which is designed as one barrel and two extended barrel hadron parts with inner radius of 2.3 m and outer radius

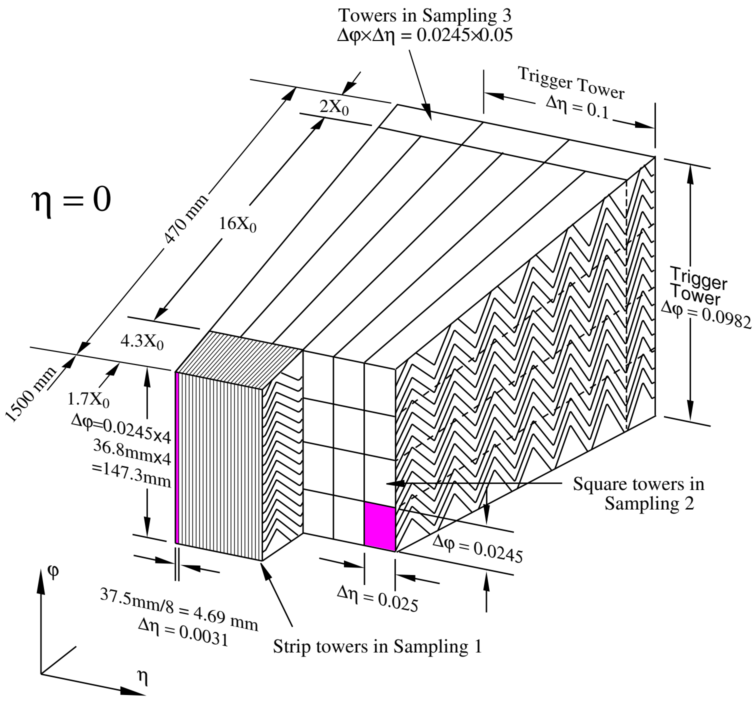

Figure 2.6: Perspective view of the accordion structure of the em calorimeter [53].

of 4.2 m, respectively. The barrel part has a 5.6 m length along the beam axis, while each of the extended barrel parts is 3 m long.

All ATLAS calorimeters are of the sampling type. A typical sampling calorimeter consists of different materials with different functions:

- **Passive material.** The function of the passive material is absorption of the particles. A high density material is usually used in absorption layers (lead, iron, copper, uranium).

- **Active material.** In the active material the signal generation takes place. The main signal sources in active material are ionisation and scintillation processes.

In the following sections a detailed description will be given to the different parts of the ATLAS calorimetry.

Electromagnetic calorimetry

The technology used in the ATLAS em calorimetry is based on LAr as the active material and lead for absorbers over its full coverage. The "accordion geometry" for absorbers and electrodes shown in Figure 2.6 provides high granularity and very good hermeticity. Due to the accordion geometry, the em calorimeter doesn't have any azimuthal cracks and is symmetric in ϕ which has an important impact on the accuracy of energy measurements.

A set of requirements for the em calorimeter performance can be formulated based on the underlying physics processes to be studied and the LHC experimental conditions. A summary of em calorimeter requirements can be written as follows:

- **Excellent energy and angular resolution.** The expected energy resolution of the em calorimeter is:
$$\frac{\Delta E}{E} = \frac{10\%}{\sqrt{E(GeV)}} \oplus 1\% \tag{2.4}$$
The em calorimeter will provide the important signatures for Higgs searches in channels: $H \to \gamma\gamma$ and $H \to ZZ \to 4e$. With the given energy resolution it would be possible to achieve a Higgs mass resolution of 1%. The angular resolution for the reconstruction of photons should be 50mrad/$\sqrt{E}$.

- **Linearity of response better than 0.5% and energy scale precision 0.1%.** The non-linearity and accuracy of the energy scale will contribute to the systematic errors of Higgs mass measurements.

- **Excellent γ/jet, electron/jet, τ/jet and γ/π_0 separation.** This is important to suppress the QCD jet background. The jet rate is expected to be five orders higher than the rate of isolated electrons with $p_T > 20$ GeV. The high segmentation of em calorimeter and information from the inner tracker must provide a good jet background rejection.

- **Low noise level.** The main noise contributions to the energy resolution come from pile-up event and electronic noise of the readout chain. Fast detector response, and fast electronics and high granularity are required to suppress the pile-up and electronic noise.

Electromagnetic calorimeters

The em calorimeter consists of the barrel part ($|\eta| < 1.475$) and two end-caps ($1.375 < |\eta| < 3.2$). The barrel calorimeter has two identical half-barrels, separated by a small gap (6mm) at $z = 0$. In the central region for $|\eta| < 2.5$ the em calorimeter consists of three longitudinal sampling layers with different granularities. For $|\eta| > 2.5$, the em calorimeter is segmented in two longitudinal sections and has a coarser lateral granularity. The total number of readout channels is $\sim$ 190000. The total thickness of the em calorimeter is above 24 X_0 in the barrel and above 26 X_0 in the end-caps.

Presampler

The total material (cryostat walls, solenoid coil, inner detector etc.) seen by an incident particle before the calorimeter front face is about 2.3 X_0 at $\eta = 0$, and increases with pseudorapidity in the barrel because of the particle angle. In the region where the amount of material exceeds ~ 2 X_0 (as is the case for $|\eta| < 1.8$), a presampler is used to correct for the energy lost by electrons and photons upstream of the calorimeter. The presampler consists of an active LAr layer of thickness 1.1 cm (0.5 cm) in the barrel (end-cap) region. In the transition region between barrel and end-cap, around $\eta = 1.4$, a scintillator layer between the two cryostats is used to compensate the energy losses in the dead material which reaches a maximum of 7 X_0.

Hadronic calorimetry

The main objectives for hadronic calorimetry is accurate determination of E_T^{miss} and jet reconstruction. The requirements formulated in [42] can be summarised as follows:

- **Rapidity coverage.** The precision of the measurements of E_T^{miss} and jet energy which can provide an important signature for new physics requires a rapidity coverage up to $|\eta| < 5$. The critical regions for E_T^{miss} and jet measurements are the transition or crack regions in the calorimeter, which need more careful treatment.

- **Energy linearity for jets.** The study of the quark compositeness signatures requires the jet energy scale accuracy to be within 1% – 2% up to the E_T of 4 TeV.

- **Energy resolution.** In order to fulfill the physics requirements for precise jet-jet mass reconstruction in $W \to jet + jet$ decay and top quark mass measurements, the jet energy resolutions have to be:

$$\frac{\Delta E}{E} = \frac{50\%}{\sqrt{E}} \oplus 3\% \quad \text{for } |\eta| < 3 \tag{2.5}$$

$$\frac{\Delta E}{E} = \frac{100\%}{\sqrt{E}} \oplus 7\% \quad \text{for } 3 < |\eta| < 5 \tag{2.6}$$

- **Total thickness.** The total calorimeter (em and hadronic) thickness of about 10 interaction lengths $10\lambda_{int}$ in order to provide an adequate hadron shower containment and background reduction for the muon system. The interaction length is defined as the average distance a hadron has to travel in the calorimeter before a nuclear interaction takes place.

Tile Calorimeter

A large scintillating tile hadronic barrel calorimeter (TILECAL) is a sampling calorimeter which uses iron as the absorber material and scintillating tiles (3 mm thick) as active material. The tiles are placed in planes perpendicular to the colliding beams and are staggered in depth. They are read out by wavelength shifter fibers (WLS) oriented in the same direction as the tiles. These fibers are connected to Photomultiplier Modules (PMTs). A single TILECAL module is illustrated in Figure 2.7.

The WLS absorb the scintillation light, transmit it along the fiber and re-emit it at a lower energy *i.e.* longer wavelength. The development of the WLS with perpendicular tiles orientation to the direction of the incoming particles made it possible the innovative geometry of the TILECAL . This geometry provides a hermetic coverage and ϕ uniformity in the calorimeter response. The TILECAL contains three sampling layers in longitudinal direction with granularity 0.1×0.1 in $\Delta\eta\times\Delta\phi$ with some exceptions in the third layer with coarser granularity (0.2×0.1). Azimuthally, the barrel and extended barrels are divided into 64 modules. In η, the readout cells, built by grouping fibers into a photomultiplier, are projective to the interaction point. The calorimeter is placed behind the em calorimeter ($\sim 1.2\lambda_{int}$). The total number of readout channels is about $\sim$ 10000.

LAr Hadronic End-cap Calorimeter

The hadronic end-cap calorimeter (HEC) shares the cryostats with the em end-cap calorimeter and the forward calorimeter. The HEC is a LAr sampling calorimeter with absorber plates made of copper. It is designed to provide coverage for hadronic showers in the range $1.5 < |\eta| < 3.2$. The HEC consists of the four wheels, two in each end-cap cryostat.

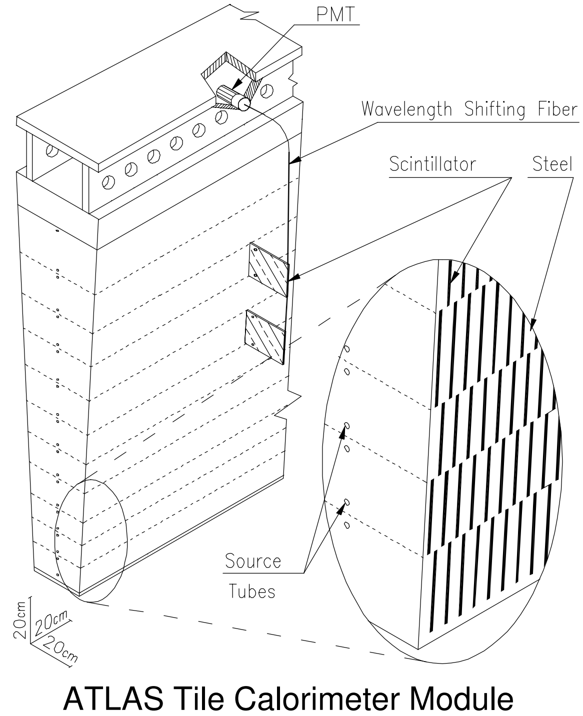

Figure 2.7: Schematic view of a single Tile calorimeter module. The various components of the module – scintillator tiles, fibers, PMTs are shown [54].

LAr Forward Calorimeter

The main objective for the FCAL is to provide an acceptance region for the forward jets which can be signatures of heavy Higgs production in the vector boson fusion process. Another function of the FCAL is to minimise the background for the muon system.

The FCAL covers the range $3.1 < |\eta| < 4.9$. Due to the high radiation level in this η region the FCAL is made of radiation-resistant materials. The FCAL was designed as a high density detector, in order to achieve $9.5\lambda_{int}$ in a short longitudinal space and prevent energy leakage. It consists of three longitudinal sections. The first section is made of copper, while the other two are made of tungsten. In each section there is a metal matrix with regularly spaced tubes which are parallel to the beam line. The readout electrode made of copper consists of a rod inserted in a tube. The distance between rod and tube is filled by LAr and form LAr gap with thickness 0.2 mm. The FCAL granularity is $\sim 0.2 \times 0.2$ in $\eta \times \phi$. The total number of channels is 3584.

2.2.3 Muon spectrometer

The concept of the muon spectrometer is based on the magnetic deflection of muons in a system of three large superconducting air-core toroid magnets. In the central pseudorapidity range $|\eta| \leq 1$, magnetic bending is provided by a large barrel magnet constructed from eight coils surrounding the hadron calorimeter. In order to achieve a muon momentum resolution $\Delta p_T/p_T < 1 \times 10^{-4} \times p_T$ [GeV] an accuracy better than 50 μm is required.

For the range $1.4 \leq |\eta| \leq 2.7$, muon tracks are bent in two smaller end-cap magnets inserted into both ends of the barrel toroid. The range $1 \leq |\eta| \leq 1.4$ is referred to as transition region, where deflection is provided by a combination of barrel and end-cap magnetic fields.

Four different types of tracking chambers are used to perform precise measurements of muon tracks and triggering using the signals from the muon system. In the barrel region the chambers are mounted in three cylindrical layers around the beam axis, while in the transition and end-cap regions the chambers are installed vertically, also in three layers. The total number of readout channels in muon spectrometer is about 10^6.

Monitored Drift Tubes (MDTs) provide precision measurement of muon track coordinates over most of the η-range. The MDTs are aluminum tubes of 30 mm diameter, 50 μm diameter central wires and length from 70 cm to 630 cm. The single-wire resolution is about 80 μm.

Cathode Strip Chambers (CSCs) are used at large pseudorapidities and close to the interaction point. They have a higher granularity than the MDTs and are appropriate for demanding rate and background conditions. The CSCs are multi-wire proportional chambers with cathode strip readout.

Resistive Plate Chambers (RPCs) and **Thin Gap Chambers** (TGCs) provide the trigger function of the muon system in the barrel and end-cap regions, respectively. They cover the pseudorapidity range $|\eta| \leq 2.4$. The RPCs are very fast by design, the typical time resolution they provide is 1 ns. RPC is a gaseous detector without wires with a small gas gap ($\sim$ 2 mm) between two resistive plates. The TGC are similar in design to multi-wire proportional chambers with a gas gap of 2.8 mm and anode wire diameter of 50 μm.

The trigger chambers provide bunch-crossing identification, a trigger with well-defined p_T thresholds and measurements of the second coordinate in a direction orthogonal to the one measured in the precision chambers.

In order to provide high momentum resolution of the spectrometer, the chamber deformations and positions are constantly monitored by means of optical alignment systems ($\sim$ 5000 optical sensors) with an accuracy of 10 μm or better.

2.2.4 Magnet system

The ATLAS magnet system is a system of four large superconducting magnets. This magnetic system is 22 m in diameter and 26 m in length. It consists of:

- the solenoid which is aligned with the beam axis provides a 2 T axial magnetic field for the inner detector.
- the barrel toroid and the two end-cap toroids provide a toroidal magnetic field of approximately 0.5 T and 1 T for the muon detectors in the central and end-cap regions, respectively.

2.3 The Trigger system

At the LHC design luminosity of $10^{34} cm^{-2} s^{-1}$ and bunch-crossing rate of 40 MHz the expected event rate is 10^9 Hz, while the event data recording is restricted to a few hundred Hz due to the limitations set by processing time and storage capacity. The primary goal for the ATLAS trigger and Data Acquisition (DAQ) system is to reduce the initial event rate to an acceptable rate for permanent storage by pre-selecting rare events with interesting physics signatures. The total rate reduction factor provided by the ATLAS trigger system is expected to be $\sim 10^7$ which corresponds to an $\mathcal{O}(100)$ Hz reduced event

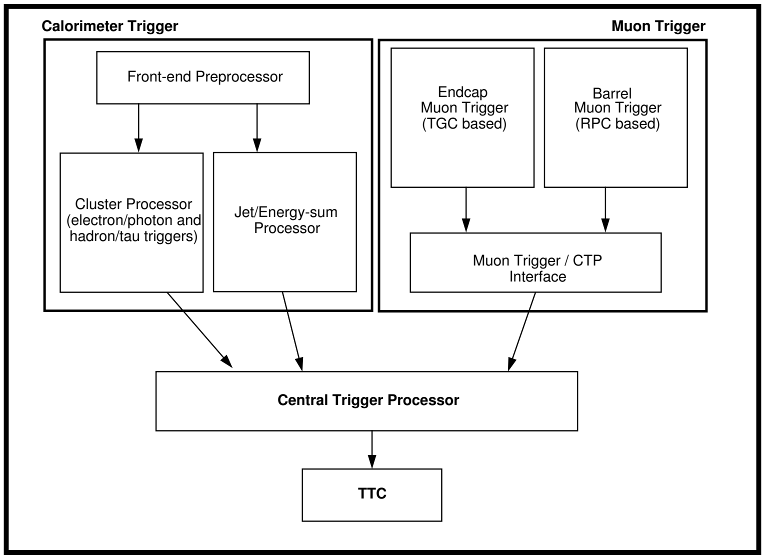

Figure 2.8: Block diagram of the Level-1 trigger system [43].

rate for storage. The total event size of ∼ 1.5 MB gives a storage capacity of 300 MB/s. In general it takes about ∼1 s for the trigger and DAQ system to process the event until it is permanently stored. The long processing time in the acquisition system compared to the LHC bunch-crossing requires pipelined buffers for temporary event storage.

The ATLAS trigger consists of three levels of event selection: Level-1, Level-2 and Event Filter. The Level-2 trigger and Event Filter are usually referred to as High Level Trigger (HLT). In the following two sections the description of the architecture of the ATLAS trigger system and DAQ as well as data flow from the detector front-end electronics to storage is given.

2.3.1 Level-1 trigger

The Level-1 Trigger consists of three parts: the Calorimeter Trigger, the Muon Trigger and the Central Trigger Processor (CTP). The block diagram of the Level-1 Trigger is shown in Figure 2.8 The Level-1 trigger is implemented as a pipelined parallel custom-electronics system, running synchronously with the LHC bunch-crossing frequency of 40 MHz. The reason for such an implementation is to minimise the latency[1] for the Level-1 trigger. The design of the detector front-end electronics and trigger requires the latency of the Level-1 trigger to be smaller than 2.5 μs. The “hard-wire” algorithms perform fast processing of the data coming from calorimeters and muon detector and provide the final decision to accept or reject an event within a fixed time of 2 μs. Furthermore, the Level-1 trigger reduces the event rate from 40 MHz to ∼ 100 kHz [43].

Level-1 calorimeter trigger

The Level-1 calorimeter trigger consists of three subsystems:

- **Pre-Processor (PPr)**

---

[1] Latency – time taken to form and distribute trigger decision.

- **Cluster Processor (CP)**
- **Jet/Energy-sum Processor (JEP)**.

The calorimeter trigger receives about $\sim$ 7200 analog signals from electromagnetic and hadronic calorimeters, which are digitised and assigned to the correct bunch-crossing in the Pre-Processor subsystem. The digitally processed data are then transmitted to the CP and JEP subsystems. The CP subsystem identifies possible isolated electrons, photons and hadronic τ decays. The JEP subsystem identifies jet objects and calculates the global sums for the E_T^{miss} and $\sum E_T$ triggers. The identified by CP and JEP subsystems objects are referred to as trigger objects. The processing results are sent to the CTP and Regions of Interests (RoI)[2] are sent to the Level-2 trigger system. A detailed description of the level-1 calorimeter trigger will be given in the next chapter.

Level-1 muon trigger

The level-1 muon trigger is based on the trigger chambers RPC and TGC of the muon spectrometer. A short description of the trigger chambers was given in section 2.2.3. The muon trigger processes the hit information coming from RPCs in the barrel region and TGCs in the end-caps. The trigger reconstructs the muon path using the coincidence between hits in different muon detector layers. Based on this information it identifies muon track candidates above the programmable p_T threshold and assigns them to the unique bunch-crossing. The trigger has to operate with with a p_T threshold in the range 6-35 GeV. The muon trigger sends the information to the Muon-to-Central-Trigger-Processor Interface (MUCTPI), which calculates the multiplicity values for muon candidates for the six programmable p_T thresholds, removes doubly counted tracks and provides the results to the CTP. The MUCTPI also distributes the RoI information to the Level-2 trigger and to the DAQ system.

A large fraction of muon trigger electronics is distributed on the detector in the ATLAS cavern in order to provide an accurate timing of detector signals into trigger logic and to reduce the cabling from $\sim$ 800k channels. The data from the on-detector logic are transmitted after processing via $\sim$1000 optical links to the off-detector electronics located in ATLAS service cavern USA15.

Based on the calorimeter and muon trigger data, the CTP generates the final Level-1 "yes/no" decision to accept or reject the event. This decision is based on the the Level-1 trigger menu. The Level-1 trigger menu can be defined as a set of logical combinations of results from the Level-1 Calorimeter and Muon Triggers. The decision generated by CTP is sent to the Timing, Trigger and Control (TTC) system.

Based on the optical-broadcast system, the TTC distributes the Level-1 Accept signal together with the LHC clock (bunch-crossing), other trigger information, and control commands to readout electronics of the detector subsystems. On every L1Accept, CTP also provides Level-1 trigger summary information to the DAQ. In case the event is finally accepted and stored, these data can be used for offline trigger monitoring and trigger performance studies.

---

[2] Regions of Interests (RoI) are the detector regions with interesting signatures, identified by Level-1 trigger and used as guideline by the Level-2 trigger. The Level-1 RoI record contains the selected trigger type and the coordinates in (η, ϕ).

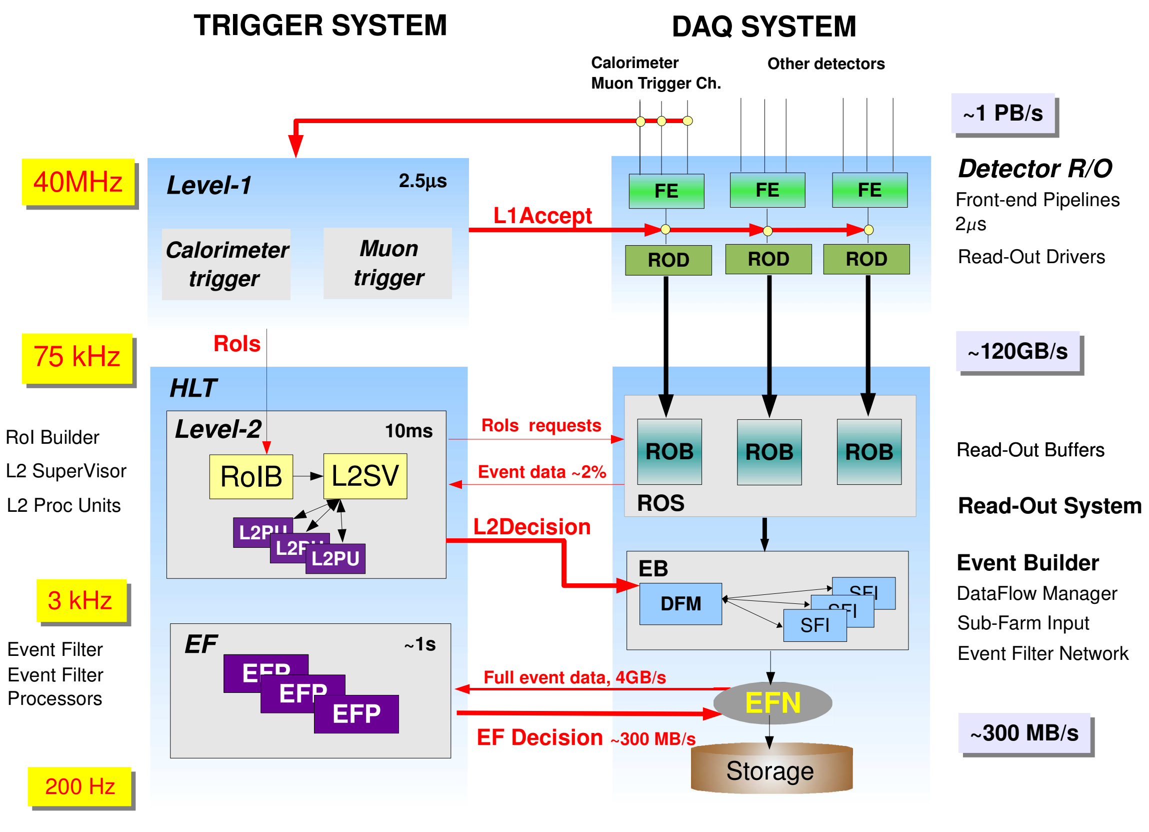

Figure 2.9: Block diagram of the trigger and DAQ system.

2.3.2 High-level trigger and DAQ

The complete High-level trigger system consists of software applications, which run on standard Linux PCs connected to standard Ethernet networks. The block diagram of the ATLAS trigger/DAQ system and dataflow is shown in figure 2.9. Upon a L1Accept, the data are pushed from detector front-end buffers to the ReadOut System (ROS) via ReadOut Drivers (RODs). In RODs the data are formatted in event fragments. The ROS is responsible for receiving data from the detector and storing them as long as it required by the Level-2 trigger. It consists of ∼150 ROS PCs. Upon a request the ROS makes the data available to the further systems via the Gigabit Ethernet network. The incoming bandwidth to the ROS is expected to be 120 GB/s. All events fragments transmitted via ∼ 1600 readout optical links for the selected bunch-crossing are stored in ReadOut Buffers (ROBs) until the Level-2 generates a decision [44].

In the previous paragraph the flow of the detector data has been discussed upon the L1accept generation. Meanwhile the positive decision made by the Level-1 trigger activates the Level-2 trigger algorithms which are able to look more precisely at an event accepted by Level-1. The Level-2 trigger algorithms are included in the HLT software framework, which performs the event reconstruction and selection applying a sequence of steps to the trigger candidates in order to identify final physics objects like electrons, photons etc. A detailed description of HLT algorithms can be found in [45].

The Level-1 trigger supplies Level-2 trigger with RoI information via RODs. The Region-of-Interest Builder gathers the RoI information from various parts of the Level-1 trigger and sends it to the Level-2 SuperVisor (L2SV).

The Region-of-Interest Builder (RoIB) in the High Level Trigger (HLT) is a VMEbus based system which consists of 9U VME boards. It is designed to collect raw event fragments from the Level-1 trigger sources and assemble the data fragments into a complete RoI record of Level-1 [46].

The Level-2 SuperVisor (L2SV) receives the RoI information from RoIB and assigns it to the least loaded Level-2 Processing Unit (L2PU) for further analysis. The L2PU is part of the Level-2 SuperVisor farm which consists of standard PCs connected to the RoIBs via S-links [47] and to the HLT via Ethernet.

The trigger algorithms running on the assigned L2PU make a request to the ROS system to retrieve the full granularity event data within a given RoI and generate a decision according to the trigger menu. In this way the Level-2 system uses the RoI as seeds for information to be processed, which significantly reduces the data transfer. This approach reduces the amount of event data required for the Level-2 trigger to generate the decision to value of ~2% from the full event size. The L2SV receives the results of the proccesing from L2PU and forwards it to the DataFlow Manager (DFM). The Level-2 trigger reduces rate to ~ 3 kHz with average latency 10 ms.

The DataFlow Manager controls the event-building on the Event Builder (EB) nodes. The main tasks for DFM is to receive the Level-2 decision and allocate a free (EB) node and control even-building process. DFM is a multi-threaded application running on a single PC equipped with two CPUs.

Upon the Level-2 positive decision the event data fragments are collected by EB node called SubFarm Input (SFI), built and formatted into a complete event. The events which are rejected by Level-2 are deleted from the corresponding ROBs of the ROS.

After an event is fully assembled by the EB it is sent to the Event Filter (EF) via the Event Filter Network (EFN) which connects EB, EF nodes and permanent storage. The Event Filter is a combination of hardware and software which processes the event in the last stage of the selection. The Event Filter farm combines ~ 1900 nodes [48]. At this stage the full event reconstruction and selection using alignment, calibration and magnetic data is done. The reconstruction is performed using the complex offline style algorithms, developed in the ATLAS offline software framework Athena [49]. The typical EF processing time is 1-2 s. The EF is also seen as an important stage of online physics and detector monitoring. The event accepted by the EF is finally sent to permanent store at a final rate of ~200 Hz.

Chapter 3

The Level-1 Calorimeter Trigger

3.1 Overview

The Level-1 Calorimeter Trigger is a pipelined digital system built of custom- and commercial electronics components. The Calorimeter Trigger electronics is located in the USA15 cavern and completely separated from the on-detector electronics by a thick shielding wall ($\sim$ 2m). The Calorimeter Trigger consists of the three major processing subsystems: Pre-Processor (PPr), Cluster Processor (CP) and Jet/Energy-sum Processor (JEP).

The input to the Calorimeter Trigger is formed by $\sim$ 7200 analog signals from the electromagnetic and hadronic calorimeters, summed in projective Trigger Towers (TT) with a granularity in $\eta \times \phi$ of 0.1×0.1.

The Pre-Processor receives analog input signals from all ATLAS calorimeters and digitises and synchronises them in parallel; in addition it performs the bunch-crossing identification (BCID), uses a Look-up-Table (LUT) to calibrate the transverse energy and perform the pedestal subtraction in order to suppress noise. The eight-bit E_T values with accuracy of $\sim$ 1 GeV are the output data, which are transmitted to the subsequent processors. The Pre-Processor system occupies eight 9U VME crates.

The Cluster processor receives the digitally processed data from the PPr. The Low Voltage Differential Signaling (LVDS) technology is used to provide high-speed transmission of the data downstream. The main tasks of the CP is identification of possible isolated electrons, photons and hadronic τ decays. The 56 CP Modules (CPM) are located in four 9U crates. The results from all CPMs are collected and summed by 8 Common Merger Modules (CMM). The final multiplicities of objects which pass the programmable threshold conditions on the transverse energy are sent to the CTP.

The JEP subsystem is hosted in two 9U VME crates and consists of 32 Jet/Energy-sum Modules (JEMs). The JEP and CP systems use the same custom crate backplanes, that improves the uniformity of the trigger system. JEP identifies jet objects and calculates the global sums for the E_T^{miss} and $\sum E_T$ triggers. The 4 CMMs merge the results from all the modules and transmit them to the CTP. Based on the data from both systems the CTP makes a decision to accept or reject an event and distributes it to the trigger and DAQ system.

Searching for the trigger objects in both CP and JEP systems is performed by means of a sliding window algorithm which will be discussed for each system in some detail in the next sections. Here it has to be mentioned, that the algorithm requires a large amount of data to be shared between processors on board level and on crate level. Thus the feature of the Calorimeter trigger is a large number of interconnections between modules and crates

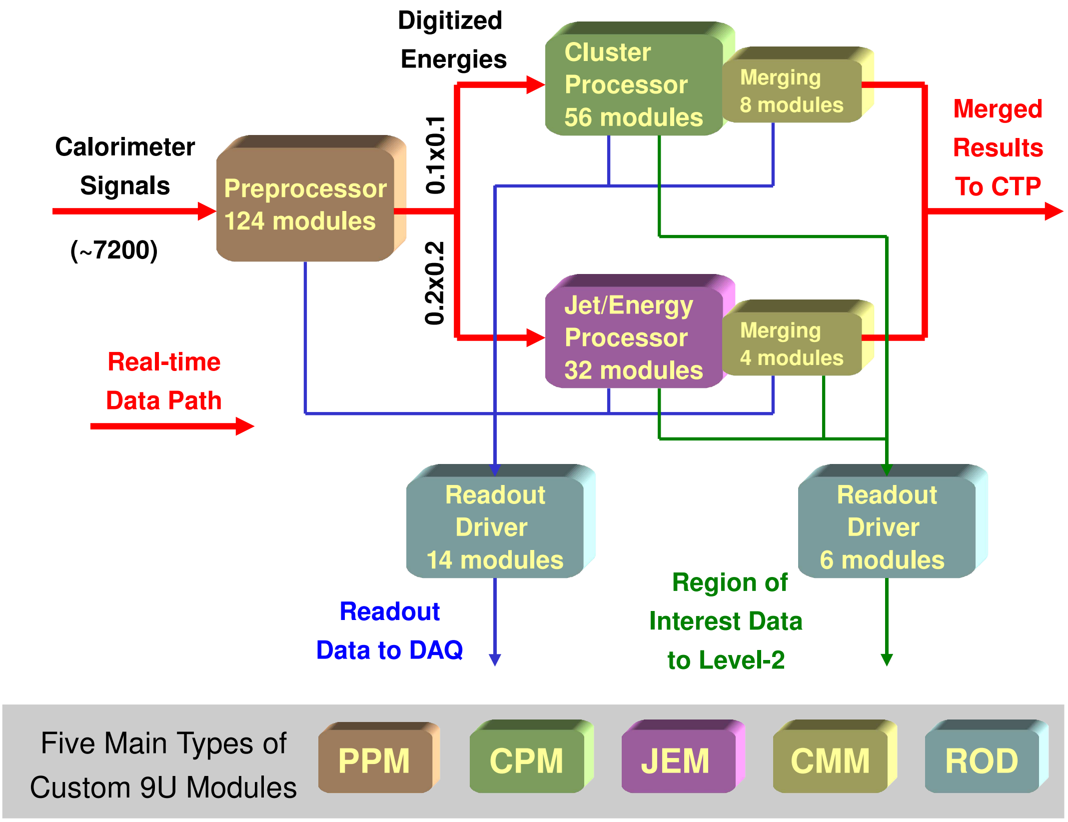

Figure 3.1: Simplified block diagram of the Level-1 Calorimeter Trigger [51].

in order to fulfill the algorithm requirements.

In addition to the described data path, which is usually referred to as trigger real-time path, each system of the Calorimeter trigger generates readout data as a response to a Level-1 Accept signal, produced by CTP and distributed by TTC. These readout data represent the auxiliary intermediate data for each module as well as output and input data (after digitisation for PPr). The readout data are sent via high-speed ($\sim$ 800Mbit/s) optical links using the Agilent G-link technology to the ReadOut Drivers (RODs) and then to the ROS. It is intended to be used for monitoring purposes of the trigger performance in online data taking or in offline analysis. Other RODs are used for RoI data transmission to the Level-2 trigger. There are 20 RODs in the system. 14 RODs process only DAQ data, while the remaining 6 process only RoI data. A simplified block diagram of the Level-1 Calorimeter Trigger is given in Figure 3.1.

3.2 Pre-Processor

In the following sections the architecture and basic functionality of the Pre-Processor system is given. A detailed description of the Pre-Processor system can be found in [55].

3.2.1 The analog front-end input signals

The analog trigger tower signals are the input to the PPr system. They are formed by summation of calorimeter readout cells. The profile of the pulses coming from the LAr

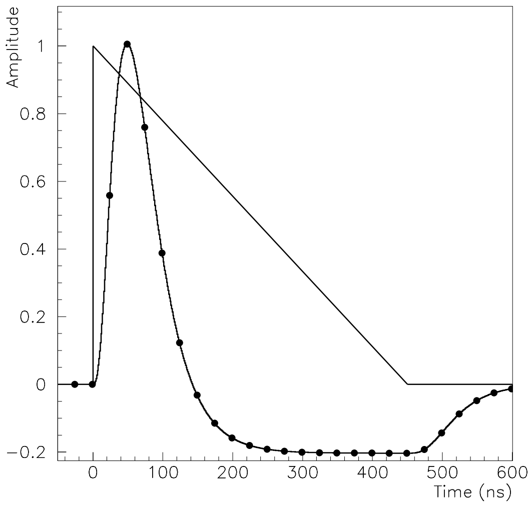

Figure 3.2: A typical LAr triangular pulse produced in the detector, and the pulse after bipolar-shaping. The dots show the sampling points at 40 MHz frequency [53].

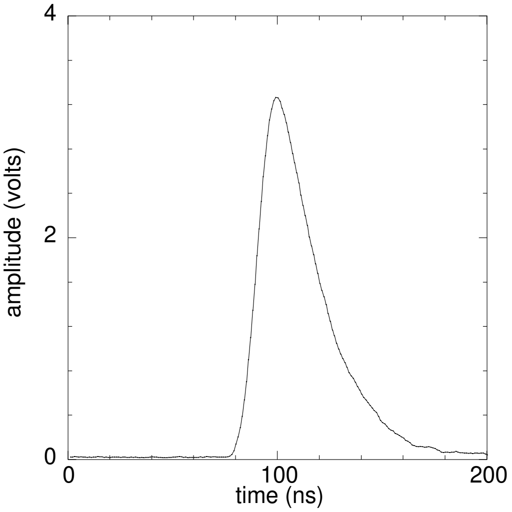

Figure 3.3: A unipolar TILECAL pulse [54].

and TILECAL detector cells is not the same. A typical current waveform coming from the LAr detector looks like a triangle with a drift time of 400 ns. In order to make the pulse faster to minimise the pile-up effect, it is shaped by bipolar shapers with a shaping time of $\sim$ 50 ns. It is worth mentioning that due to this shaping the pulse is sampled within 5 bunch-crossings before crossing the zero baseline. The accommodation of the pulse within 5 sampling points has an important impact on the trigger architecture and algorithms. The pulse before and after shaping is shown in Figure 3.2.

The signals coming from TILECAL, produced by PMTs based on scintillation light are quite fast with respect to the LAr signals. Their FWHM[1] value is $\sim$ 15 ns. Before being transmitted to the trigger system, the TILECAL signal is also shaped in order to be similar to the LAr waveform. A typical pulse coming from the TILECAL detector is unipolar pulse of $\sim$ 50 ns FWHM with amplitude proportional to the input charge, as shown in Figure 3.3.

After shaping the calorimeter signals are combined in the trigger towers. Each trigger tower is formed by analog summation of a variable numbers of calorimeter cells varying from a few up to sixty, depending on the calorimeter type and region. This analog summation is done separately for electromagnetic and hadronic calorimeters by the on-detector electronics. The granularity of the TTs is typically 0.1×0.1 in η, ϕ in the pseudorapidity range of $|\eta| < 2.5$ and gets coarser to 0.2×0.2 in the range $|\eta| > 2.5$ and up to 0.4×0.4 in the FCAL region. The analog signals after summation are sent to the Calorimeter trigger via twisted-pair cables with various length from 40 m to 70 m. Each cable carries 16 differential signals.

Before reaching the Pre-Processor inputs the analog differential signals arrive at the Receiver System [52] which is physically located in USA15 cavern as well as the Calorimeter Trigger. At this stage the gain can be adjusted in order to calibrate the signals to the correct E_T scale and for attenuation in the cables. The main functions of the Receiver

---

[1] FWHM – a full width at half maximum.

System can be summarised as follows:

- Signal processing. Gain fine adjustment of the analog signal in the calibration sequence in order to bring it to the specified level on the voltage scale: 2.5 V corresponds to E_T=250 GeV. The gain adjustment is implemented using variable gain amplifiers (VGAs) in the system.
- Signal ordering. The signals come to the receiver depending on the hardware structure of the calorimeters. The signal ordering implies changing the order of the incoming signals according to the requirements for trigger architecture.
- Monitoring function. It provides the outputs for monitoring the calorimeter signals.

The Receiver system consist of 8 crates, 6 for the LAr calorimeters and 2 for the TILECAL. Each crates is populated by 16 receiver boards. Each of the receiver module is 9U VME board carrying 64 channels organised in 4 blocks of 16 channels (0.4×0.4 in $\eta \times \phi$). These channels are re-ordered in 4 analog output cables, which are dedicated as the inputs to the Pre-Processor Module (PPM), which is the main electronic component of the Pre-Processor system.

The amplitudes of the TT signals should be linear up to the maximum transverse energy of $\sim$ 256 GeV, which can be digitised by the PPr system. Thus, the analog signals coming to the PPr can be subdivided in two categories:

- **Non-saturated signals.** The signals whose amplitude is below 256 GeV. The trigger linearity in this energy range is an important requirement.
- **Saturated signals.** The signals whose amplitudes exceed the upper level of the PPr FADC[2] window are cut-off at this saturation level.

3.2.2 Pre-Processor tasks

The Pre-Processor is the first processing stage of the Calorimeter trigger. The main tasks of the Pre-Processor system can be formulated as follows:

- **Analog signal reception and conditioning.** The analog linear differential signals with amplitudes of ± 1.25 V received by the PPr must be converted to the unipolar ones. Then the gain and the offset of the unipolar signal should be adjusted to match the input-voltage window of 2 – 3 V of the FADC.
- **Digitisation and Timing.** After the signals are conditioned they are digitised at a 40 MHz sampling frequency by FADCs with 10-bit resolution. The programmable delay with 1 ns resolution is applied to the FADC clock phase in order to sample at the analog pulse peak. The coarser delay with 25 ns resolution is applied to the signals to synchronise their propagation time in cables with different length.
- **Bunch-Crossing Identification (BCID).** The BCID is a major task of the PPr. It implies the determination of the position of the signal maximum and assignment to it the corresponding E_T value. The flexible BCID logic implemented in PPr provides three different BCID algorithms in order to guarantee efficient BCID in the wide energy range of 0-256 GeV and for saturated signals. These algorithms will be described in more detail in the next chapter.

---

[2] Flash Analog-to-Digital Converter

- **Transverse energy calibration.** The Look-up-table (LUT) maps the 10-bit data into 8-bit data with 1 GeV resolution as it's required by the subsequent processors. In addition the LUT performs E_T fine calibration and pedestal subtraction, the later can be used to suppress noise.

- **Pre-summing of the jet elements.** According to the JEP algorithms requirements, the PPr has to provide pre-summed clusters with granularity 0.2×0.2 in $\eta \times \phi$ called jet elements. The summation of the TT signals in jet elements done by the PPr also reduces the number of links to the JEP. Four 8-bit E_T values from the TT are summed to form a jet element. The 10-bit sum is truncated to a 9-bit value with a resolution of 1 GeV.

- **Serial data transmission to the subsequent processors.** The PPr delivers the processing results via serial LVDS links at a rate of 480 Mbit/s to the subsequent trigger processors.

- **Readout and monitoring.** The PPr system provides a readout data stream. The raw data and BCID results are stored in pipeline memories waiting for the Level-1 Accept signal. Upon L1Accept reception these readout data are sent to the DAQ. The PPr system leaves the possibility to monitor each trigger tower by counting the event rates in a given channel higher than the E_T threshold, and histogramming the E_T spectra for a given bunch-crossing window. Monitoring of the background activity during data taking and in between as well as calorimeter performance can be done using PPr monitoring data. These monitoring data can be readout independently of the L1A signal.

3.2.3 System implementation

The Pre-Processor covers the entire ATLAS calorimetry acceptance range of $|\eta| < 4.9$. The main building block of the PPr system is Pre-Processor Module. The PPM is designed to pre-process 64 analog input signals from the ATLAS calorimeters. The PPr is built as an eight crate system. Each crate hosts 16 PPMs. It should be emphasised here that the PPr, CP and JEP systems are structured in quadrants in azimuth as required by the trigger algorithms. For the PPr system each PPM covers one quadrant (0-90^o) which corresponds to 4×16 in $\eta \times \phi$ trigger space in the pseudorapidity range $|\eta| < 2.5$. Thus to cover the full azimuth angle four PPMs are required. This is not the case for the endcap and forward region with TT's of coarser granularity, where one needs two and one PPM, respectively, to cover the full azimuth range.

The PPM performs complex processing of the analog trigger tower signals, which can be subdivided in the analog processing and digital processing. After reception of differential analog signals, Analog Input (An-In) boards of the Pre-Processor convert them into unipolar signals and adjust a zero baseline for each input signal. The rest of the signal processing takes place in the Multi-Chip Module (MCM). After digital processing signals are sent to the LVDS Cable Driver (LCD) card where they are routed to the subsequent subsystems. The readout is done by means of REM_FPGA which prepares data for transmission via Rear G-Link Transmission Modules (RGTMs) to the ReadOut Drivers (RODs). Temperatures of all units on the PPM, as well as board internal supply-voltages are read out by a CAN-controller. The entire data space of the module is accessible through VME.

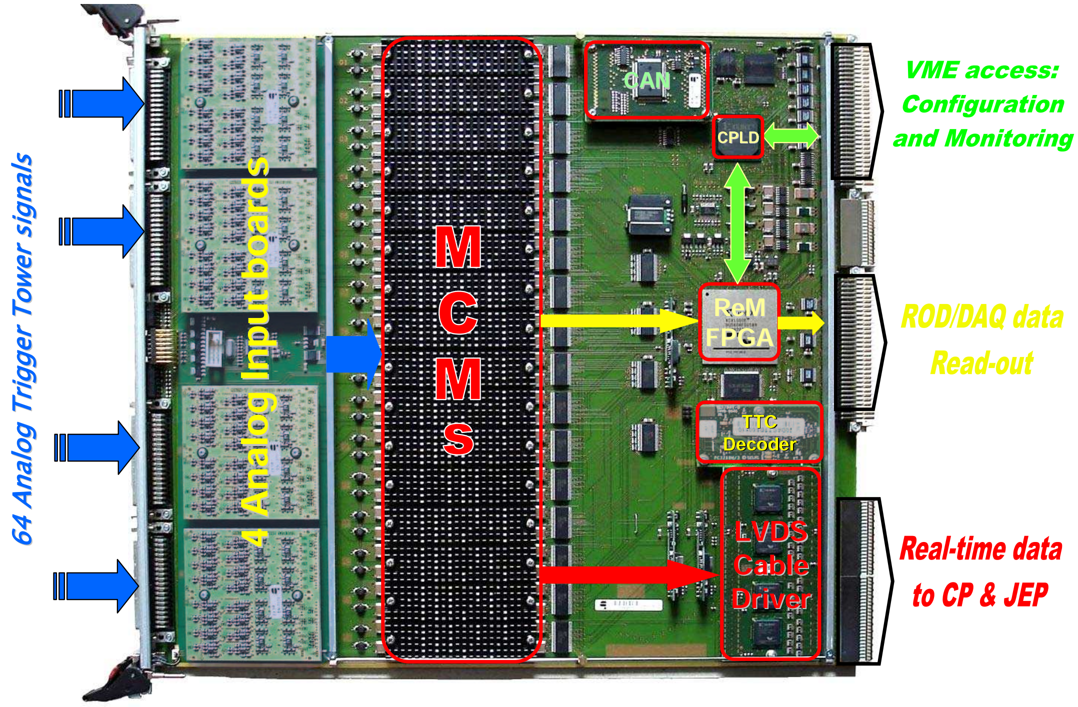

Figure 3.4: Pre-Processor Module.

The 64-channel PPM is realised as a 9U VME (standard 367x400 mm) Printed Circuit Board. Each PPM carries 23 daughter boards, where the actual signal processing takes place. The PPM together with its daughter boards is shown in Figure 3.4. The list below gives the description of the main functional blocks on the PPM:

- **The 4 Analog Input Board (AnIn).** Each AnIn receives 16 analog signals with amplitude of 0-3 V directly routed from the PPM connectors. It performs the analog signal processing. The operational amplifier on board converts the differential input signal to the single-ended and adjusts the gain of the signal by factor 0.43 to fit the input-voltage window of 1 V of the FADC on the Multi-Chip Module. The programmable 8-bit Digital-to-Analog Converter (DAC) with a 2.4 mV/step resolution adjusts the incoming signal offset by adding the DC-level offset in a range of 1.65 – 2.26 V.

  Additional comparator-based signal analysing logic and another 8-bit DAC with a resolution of 4 mV is implemented on AnIn. The binary state of the comparator output indicates whether the rising edge of the analog signal has crossed the programmable threshold provided by DAC. Thus the comparator marks the bunch-crossing when the signal exceeds the threshold by sending the binary output to the MCM. This mark can be used later by the BCID logic and is referred to as “External BCID” algorithm. The SPI [3] Bus is used to program DAC offsets and DAC thresholds.

---

[3] Serial Peripheral Interface Bus

- **The 16 Multi-Chip Module (MCM).** The MCM is a key component of the PPM. It holds the main functionality of the Pre-Processor System, namely the digitisation, calibration and Bunch-Crossing Identification of calorimeter signals. Each MCM provides 3 output serial data streams. The MCM architecture and functionality will be described in the next chapter.

- **The LVDS Cable Driver (LCD).** The LCD board receives 48 serial signals at 400 MBit/s from 16 MCMs. The LCD FPGAs perform routing and duplication of the signals as required by the algorithms in CP and JEP. In order to improve the quality of the signals, they are pre-compensated before sending by the circuitry implemented at the output of the LCD. The serial signals are transmitted over 11 m long shielded parallel 4-pair cable assemblies of type AMP to the subsequent subsystems.

- **The ReM_FPGA.** The ReM_FPGA is the master FPGA on the PPM. The entire configuration of the PPM and data readout is controlled by ReM_FPGA.

  One of the major tasks of the ReM_FPGA is to provide a VME Interface to the PPM periphery in order to perform register configuration, readout of the configuration and event data from MCMs. It communicates with AnIn via the SPI Bus, with TTC via I^2C and with the MCM via I^2C Bus and Serial Interface.

  Another task of the ReM_FPGA is to collect, merge and format the event readout data from MCMs in order to prepare them for transmission to a ROD via a G-link.

- **The Controller Area Network (CAN).** The data corresponding to the operational conditions, like temperatures measured by diodes on the MCMs, voltages and currents of power-supplies for different components on PPM, are collected by a Controller and transmitted via CANBus to the Detector Control System (DCS).

- **TTC Decoder (TTCdec).** The TTCdec receives the global signals like "LHC Clock", "L1 Accept ", "Bunch-Counter Reset" etc. distributed in serial format from the TTC and redistributes them to the various components on the PPM.

3.3 Cluster Processor

3.3.1 Cluster Processor algorithms

In order to perform identification of an isolated e/γ or hadronic τ decays as well as define the transverse energies of these trigger candidates, a trigger algorithm based on the window of 4×4 trigger towers in both em and hadronic calorimeters is applied. The algorithm scans the full trigger space. It slides the window in the η and ϕ directions by one tower. Each window can be divided in two main parts: core and isolation ring. At each step several sums of tower E_T values are calculated within a window:

- Four em. clusters within the 2×2 core of trigger towers. Each cluster is summed over two towers vertically or horizontally. For the τ algorithm four clusters are formed by summing each em two-tower cluster with the hadronic core.

- A sum of 12 em towers in the em isolation ring around the em core.

- A sum of 12 hadronic towers in the hadronic isolation ring around the hadronic core.

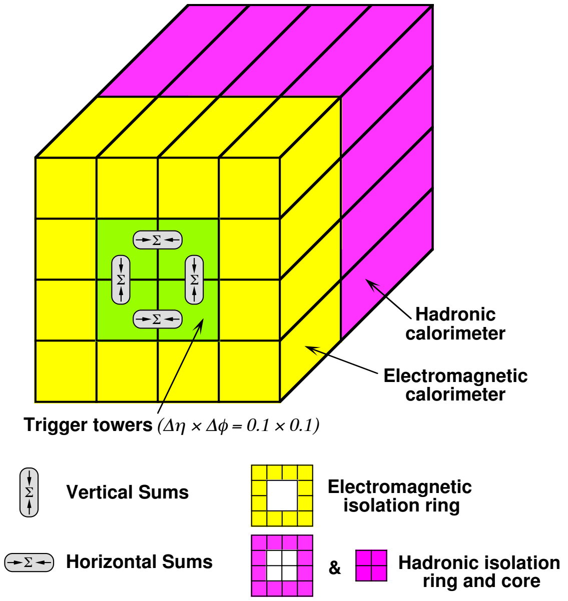

Figure 3.5: Cluster processing algorithm based on a window of 4×4 towers in both em and hadronic calorimeters [56].

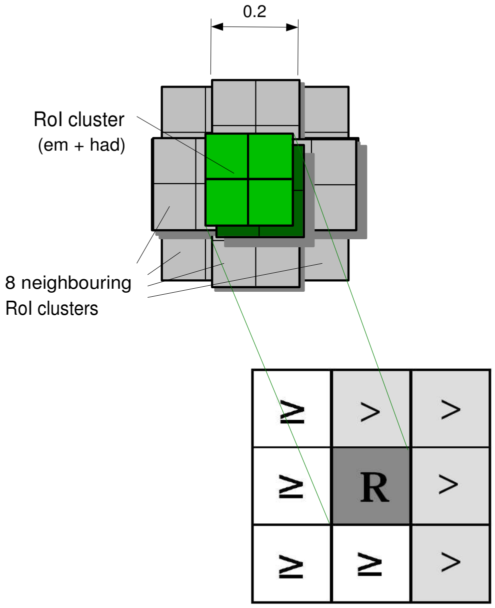

Figure 3.6: Local E_T maximum test applied to the RoI cluster of a 0.2×0.2 candidate and neighboring cluster candidates [57].

- A sum of four towers in the hadronic core is used as additional isolation region for the e/γ trigger
- A RoI cluster is the sum over four em. towers in the em core and four hadronic towers in the hadronic core.

These sums are shown in Figure 3.5. The trigger object is found within a window, if the following trigger conditions are met:

- at least one of the trigger cluster must be above predefined trigger threshold.
- The em and hadronic isolation sums must be below their corresponding isolation ring threshold.
- For the e/γ trigger only, the sum for the hadronic core must be below the hadronic core isolation threshold.
- The central RoI cluster must be more energetic than the 8 neighboring RoI clusters (see Figure 3.6), that can be formed within the same window. If this condition is met then the central RoI cluster is a local E_T maximum.

The last condition is an important one. The algorithm steps by one tower as a result it produces the overlapping neighboring windows, which may in principle satisfy all cluster and isolation criteria. In order to prevent multiple-counting of windows, the requirement

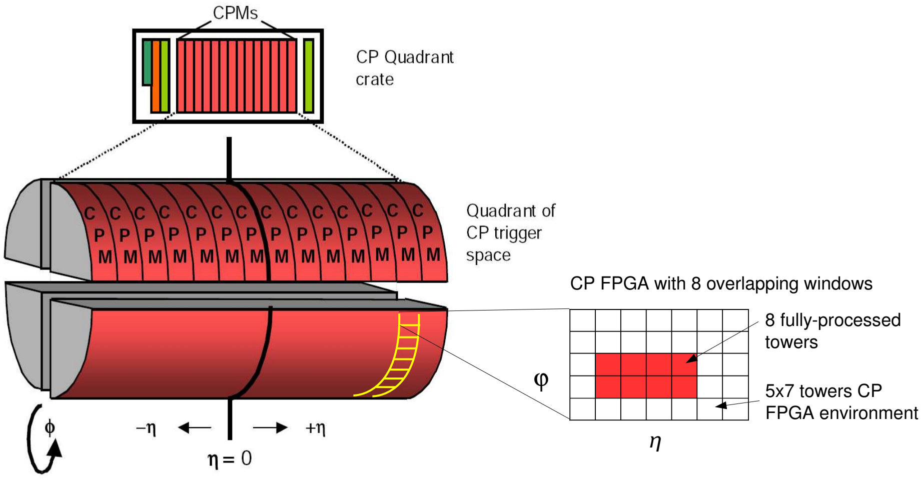

Figure 3.7: Quadrant crate architecture of the CP system (left) and organisation of trigger towers in one CP FPGA (right) [57].

to the RoI to be a local E_T maximum as shown in Figure 3.6 is implemented. The RoI is set to be a local E_T maximum, if it is more energetic ($>$) than its four neighbors on one edge and the same energetic or more ($\geq$) on the other edge.

There are 16 sets of trigger thresholds available. Eight thresholds are used for e/γ trigger only, while the other eight are used by both e/γ and τ triggers. The objects which have passed the different sets of thresholds are counted up to a maximum number 7, which corresponds to 3 bits of multiplicity value. Finally the multiplicities are sent to CTP.

3.3.2 System implementation

The Cluster Processor covers only the pseudorapidity range of $|\eta| < 2.5$. The granularity of the trigger towers in this range is 0.1×0.1 in $\eta \times \phi$, which corresponds to a 50×64 array of trigger towers to be processed by CP system.

The CP system consists of 4 crates. Each crate covers one quadrant in ϕ along the whole η range as shown in Figure 3.7. Each crate hosts 14 Cluster Processor Modules. One CPM can process 4×16 array of trigger towers. The trigger algorithms are implemented in the main processing units of the CPM called CP FPGAs. There are 8 CP FPGAs on the CPM. Each CP FPGA processes 8 towers which corresponds to 8 overlapping windows. Thus, to process 8 towers and form 8 overlapping windows, the CP FPGAs need information from the neighboring 5×7 towers which form the CP FPGA environment as shown in Figure 3.7. As a consequence, each CP FPGA has to share trigger tower data with adjacent CP FPGAs on the CPM. The CPM must share the data with other CPMs which process data in regions adjacent in η within the same crate or at the quadrant edges the data can be required from other CP crate. This data sharing is done by duplicating information at Pre-Processor level and sending it to the CPMs in both crates or via CP crate backplane in case data sharing between two CPMs.

The CPM is a 9U PCB. The main functionality of the CPM is provided by two FPGA

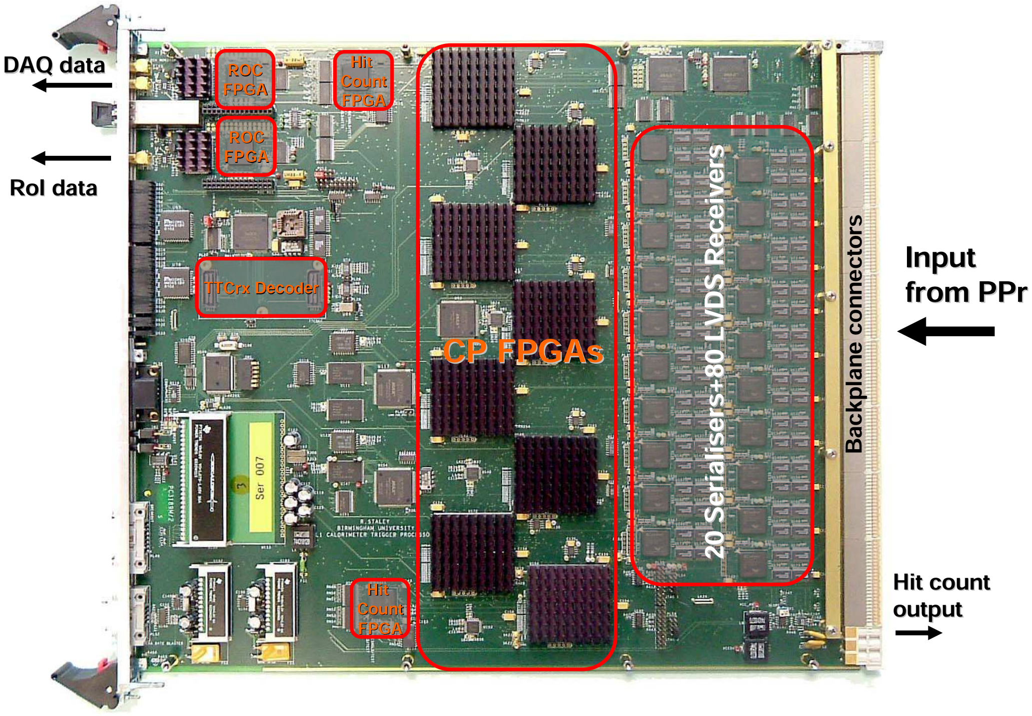

Figure 3.8: Cluster Processor Module.

types on board: Serialiser and CP FPGA. The CPM board with notations for electronic components is shown in Figure 3.8. Each CPM receives data from 80 em and 80 hadronic towers at a 400Mbit/s rate over 80 serial links from the Pre-Processor. The signals from serial links are deserialised and then reserialised to 160Mbit/s by 20 Serialisers for distribution to the CP FPGAs and for fanout to the neighboring modules across the crate backplane. The CP FPGAs process the data and send the hit[4] results to the hit-count FPGAs which sum the hits from all CP FPGAs for each threshold set (3-bit count per threshold set) on the CPM and send them to the CMM.

The CP FPGAs and Serialisers and hit-count FPGAs are also the sources of the readout data. The readout data are sent to the readout controller logic (ROC) implemented in two FPGAs – one for DAQ data and one for RoI data. The readout controllers initiate the readout upon the L1Accept signal and transmit the data via serial G-links to the RODs.

3.4 Jet/Energy-sum Processor

3.4.1 Jet/Energy-sum algorithms

The main tasks for the Jet/Energy-sum processor are: identification of hadronic jets and determination of their E_T, missing E_T and total E_T calculation. These tasks are performed by two algorithms: jet algorithm and energy/sum algorithm. The jet trigger algorithm is based on a window of 2×2 "jet elements" which have a granularity of 0.2×0.2 in $\eta \times \phi$ and are summed in depth between em and hadronic calorimeters.

---

[4] A cluster being passed a particular threshold is referred to as hit.

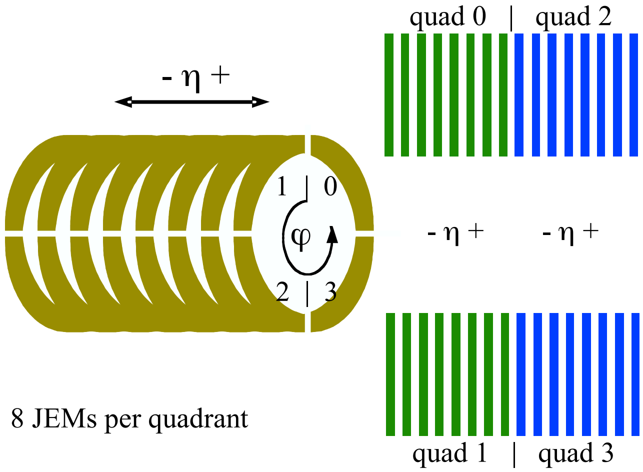

Figure 3.9: JEP channel map [58].

The jet algorithm has two components:

- A 2×2 jet RoI (0.4×0.4).
- A trigger cluster which is summed over windows of 2×2, 3×3 and 4×4 jet elements.

The two requirements should be met in order to accept the trigger object for a given threshold set:

- The RoI cluster is a local E_T maximum as was defined in section 3.3.1
- The trigger cluster E_T should pass the jet threshold. The choice of the threshold depends on the window size.

The jet algorithm supports eight jet threshold sets. Each threshold set is a combination of the E_T threshold and window size to be used to calculate a trigger cluster. For each threshold set a multiplicity of the objects passed is calculated up to limit of 7, and sent to the CTP. The energy/sum algorithm calculates the total transverse energy $\sum E_T$ from the sum over all jet elements. The missing transverse energy E_T^{miss} is determined from a vector sum. Each jet element involved in the E_T^{miss} calculation is converted to x and y projections by multiplication with $\cos\phi$ and $sin\phi$, respectively. The vector results x and y are transmitted to the merging logic on CMMs along with scalar transverse energy for summation. The missing E_T is calculated with a precision of 0.25 GeV, and total transverse energy with a precision of 1 GeV.

3.4.2 System implementation

The JEP consists of 32 JEMs which are located in two JEP crates. Each crate hosts 16 JEMs and processes two opposing quadrants in azimuth as shown in Figure 3.9. The jet algorithm covers the range up to $|\eta| < 3.2$ which is the end of the endcap calorimeter acceptance. The forward region of $3.2 < |\eta| < 4.9$ will be covered by 4 JEMs with a modified FCAL jet algorithm. Each JEM fully processes 4×8 core array of jet elements in the $\eta \times \phi$ space. But again, as in the case of the CPM, the JEM processor requires overlap

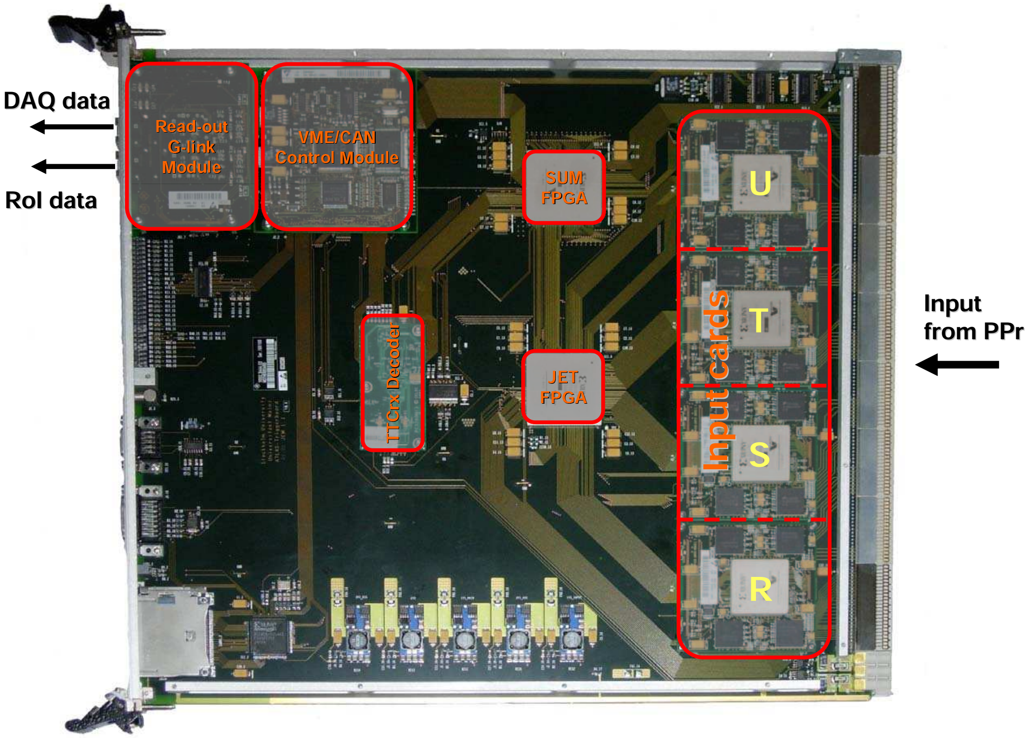

Figure 3.10: JET/Energy-sum Module.

data from the neighboring 45 jet elements to perform the “declustering” procedure and uniquely define the RoI. The JEM board is shown in Figure 3.10. There are 88 input channels on each JEM in order to receive data coming over serial links at 400Mb/s from the electromagnetic and hadronic PPMs. The four input daughter boards perform the deserialisation of the input data and sum the em and hadronic values in order to produce 10-bit jet elements. All data processing algorithms are implemented in two FPGAs. The jet algorithm is performed in the jet processor FPGA, and the sum algorithm in the sum processor FPGA. The data from neighboring jet elements are copied from the neighboring JEMs via fan in/out (FIO) links at 80Mbit/s on the crate backplane. The output result of the jet processor is a data stream which consists of eight 3-bit multiplicities and one odd-parity bit, which makes a 25-bit result data word to be transmitted via backplane links to the CMM. The sum processor provides three energy sums – 12-bit transverse energy, 12-bit E_x and E_y vector values, which are all compressed to 8-bit values and transmitted as a 25-bit data word to the CMM.

The readout data divided in the RoI and DAQ streams are sent via a readout controller ROC, located on a readout daughter module (RM) at 800Mb/s over serial links to the RODs.

Chapter 4

The functional tests of the PPr Multi-Chip Module

The Multi-Chip Module is the smallest exchangeable unit of the Pre-Processor. Being a complex electronic device it holds the main functionality of the Pre-Processor System, namely the digitisation, calibration and bunch-crossing identification of calorimeter signals. The correct functionality of the MCM has a dramatic impact on the performance of the whole ATLAS trigger system.

A series of thorough functional tests have been carried out on a few MCMs assembled for test purposes. The aim of these tests can be summarised as follows:

- Check the correct functionality and reliability of the MCM.
- Develop the testing software which includes all the test procedures in a single package.
- Develop the strategy for testing large scale MCM production.

The test procedures of the functional blocks of the MCM will be described in this chapter, and results of these tests will be presented.

4.1 The Pre-Processor Multi-Chip Module

The MCM is the main functional block of the PPM. Almost all signal processing tasks are performed inside the MCM. Each MCM processes four trigger tower signals. The MCM is designed as a compact electronic component which holds 9 chips in non-packaged form. The MCM production technique will be described later. Here it should be mentioned that the non-packaged chips on the final MCM used in the experiment are reliably protected by "glob-top"[1] coverage against damage. A fully assembled MCM substrate is shown in Figure 4.1. The chips on the MCM and their corresponding tasks can be summarised as follows:

- Four Flash ADCs (AD9042, Analog Devices)

---

[1] Glob-top is a type of electronic packaging for protection of the components against environmental, mechanical and electrical damage. It represents an encapsulate deposited over chip and its wire bonds.

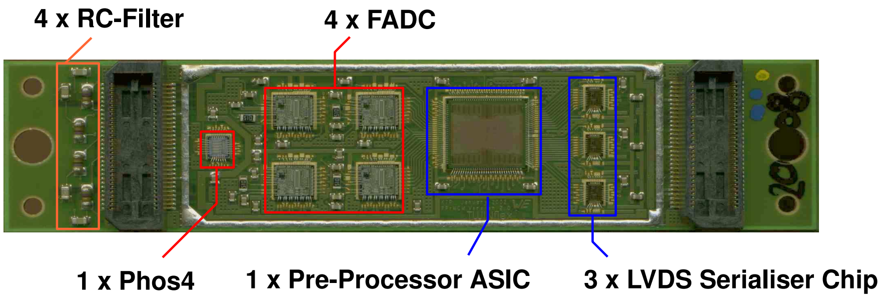

Figure 4.1: The Pre-Processor Multi-Chip Module.

  - these FADCs digitise the input signals with 10-bit resolution and a sampling frequency of 40 MHz. The input signal coming from the AnIn board is adjusted to fit the FADC digitisation range of 1 V or $V_{ref}\pm0.5V$, where $V_{ref}=2.5$ V is the FADC reference voltage. As shown in Figure 4.1 the MCM holds a low pass filter which is implemented to reduce high frequency noise and to correct for possible FADC gain deviations. Thus, taking into account that this low-pass filter reduces the voltage of the incoming signal by 20%, the range of the incoming signal is mapped to a 1.2 V window to compensate for loss of amplitude in the filter.

- Timing chip (PHOS4, CERN Microelectronics Group)
  - the PHOS4 delays the FADC clock with respect to the system clock in steps of 1 ns within a LHC clock cycle;
- Pre-Processor ASIC[2] (PPrASIC)
  - Each PPrASIC processes four digital channels and provides readout. Further tasks are: real-time bunch-crossing identification, channel synchronisation, final transverse-energy calibration, pedestal subtraction, pre-summing of jet elements, bunch-crossing multiplexing, serial data transmission;
- Three LVDS serialiser chips (DS92-LV1021, National Semiconductor)
  - The LVDS serialiser chips transmit 10-bit data words to the subsequent processors at a rate of 400 Mbit/s;

4.2 The Pre-Processor ASIC

Among the chips on the MCM, the Pre-Processor ASIC is the central component, because it performs the ATLAS-specific digital data processing for four trigger towers. The Pre-Processor ASIC is a custom-designed chip, designed at KIP and fabricated by AMS (Austria Micro Systems).

The PPrASIC is shown in Figure 4.2. The physical properties of the PPrASIC are briefly summarised as follows:

---

[2] An application-specific integrated circuit

- The size of a the PPrASIC is 8.370 × 8.375 mm^2.
- The design is realised as a 0.6 μm CMOS[3] process.
- Each PPrASIC contains logic and memories covering four signal-channels (950 000 transistors equivalent).
- The number of PPrASICs per wafer is 192.
- The total memory per PPrASIC is 8125 bytes.

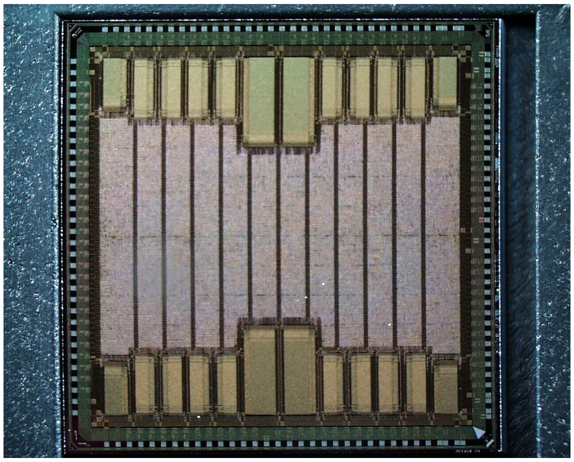

Figure 4.2: The Pre-Processor ASIC die.

The block diagram of the PPrASIC for one channel with notations for the main configuration registers is shown in Figure 4.3 A brief overview of the PPrASIC functionality is given below, whereas each functional block will be described in detail in section 4.4.

The blocks where the actual real-time data processing takes place are colored blue. The logic responsible for data monitoring and readout during processing is depicted by green blocks. The FADC input data are latched by the PPrASIC at the negative or positive edge. The choice of the latching edge is determined by the PHOS4 settings. The latched data and external BCID bit are sent to the PPrASIC FIFO block, where they can be delayed for a few bunch-crossings for synchronisation with the data in other channels. After the data are synchronised in the FIFO, they are propagated to the core of the PPrASIC functionality. This core consists of the functional blocks, which are associated with the BCID logic. The 10-bit data enter the finite-impulse response filter (FIR). The FIR filter corrects the pulse shaping distorted by noise and improves the signal-to-noise ratio. The FIR filter is a digital pipeline with five registers. These registers contain the coefficients which are applied to the samples coming into the FIR filter. Moving through the FIR pipeline the samples are multiplied by the coefficients and summed to form the FIR filter 16-bit output. The 16-bit words are truncated to 10-bit words in order to fit the Look-up-Table (LUT). The bits to be truncated are defined depending on the FIR filter settings. The processing of the 10-bit data in the LUT includes the pedestal subtraction, conversion of 10-bit words to 8-bit words, as well as transverse energy calibration.

In parallel to the described data flow the data are analysed by the BCID algorithms in the Peak Finder block for a non-saturated pulse and in satBCID block for a saturated

---

[3] Complementary Metal-Oxide Semiconductor

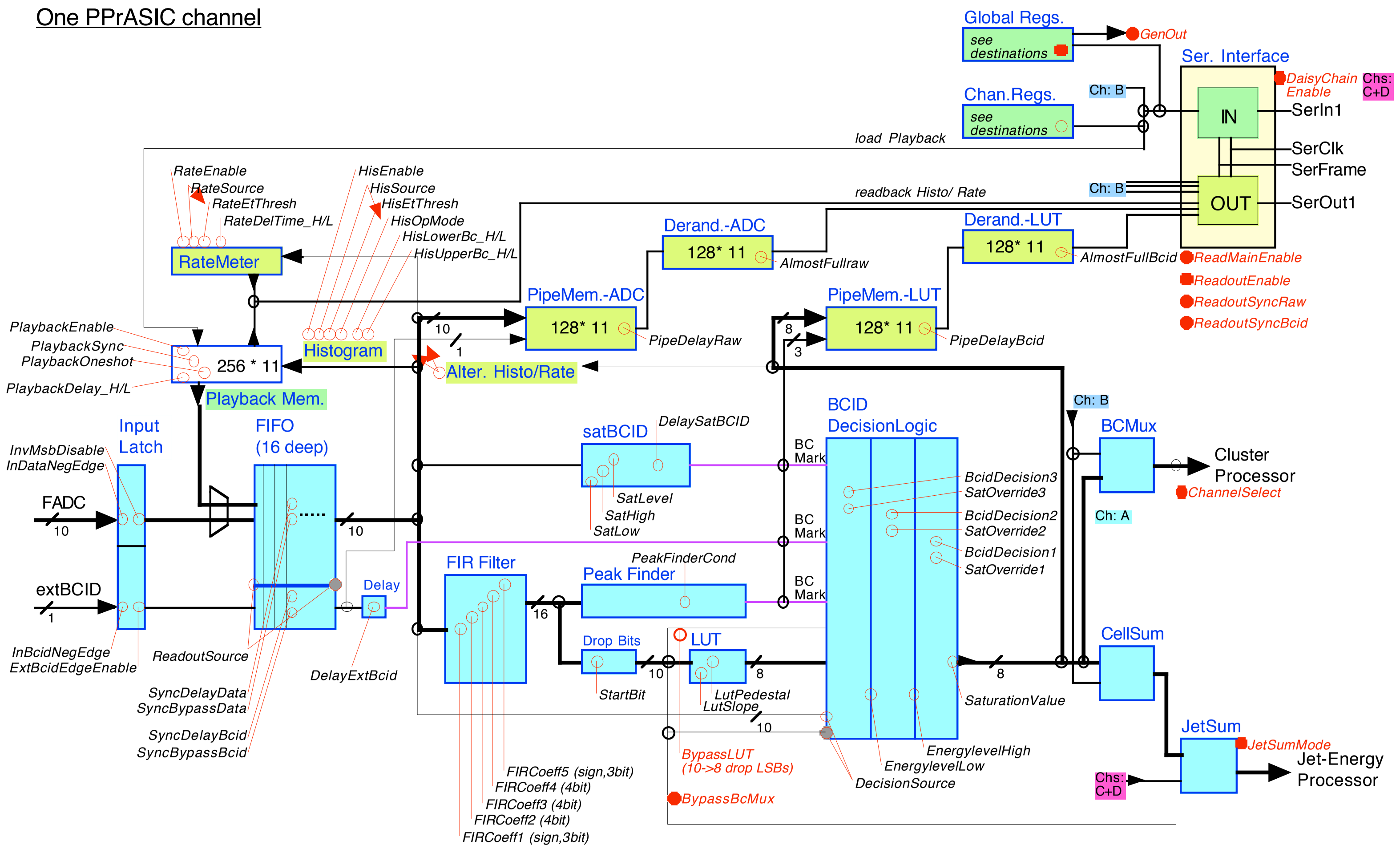

Figure 4.3: Block diagram for one PPrASIC channel [71].

pulse. The results coming from these algorithms are 2 single bit values called "BC Marks". The "BC Marks" point to the bunch-crossing containing pulse maximum found by these algorithms. Not only these two algorithms produce the BCID results. The additional external BCID bit is the output from the third BCID algorithm, which is implemented outside the MCM, on the AnIn board.

The input data for the BCID DecisionLogic block are three "BC Marks" indicating the bunch-crossings found by BCID algorithms and LUT data. This block assigns the LUT results to the bunch-crossing marked by the one of the BCID algorithms according to the configuration. The accepted BCID result is 8-bit output data from this block. The output data from two channels are propagated to the BCMux block where the BCID results are multiplexed into a single 10-bit output, which contains 8-bit BCID result, parity bit and additional flag bit. Thus four multiplexed channels on the PPrASIC form two output streams to the Cluster Processor. The multiplexing scheme significantly reduces the number of connections between Pre-Processor and Cluster Processor. In addition, the data from four PPrASIC channels pre-summed together in the 10-bit Jet Elements form the third stream to the Jet Processor.

The PPrASIC holds also readout blocks, that fetch the data at different stages of processing and transmit them to the DAQ system or to the local VME-based facilities. There are two pipeline memories implemented in the PPrASIC for readout purposes. The FADC pipeline memory contained in the block PipeMem.-ADC in Figure 4.3 continuously accepts and stores raw 10-bit FADC data, while the LUT memory PipeMem.-LUT stores the 8-bit BCID results together with 3 "BC Marks". Both memories have the same length of 128 words which corresponds to 3.2 μs. This length is quite sufficient to cover the decision latency in the Level-1 trigger. Upon the Level-1 Accept the data corresponding to the accepted event are fetched and copied from pipeline memories to the buffers, which hold the data until they are readout via a serial interface implemented on the PPrASIC.

The PPrASIC contains two serial interfaces – one per pair of processing channels. The interfaces provide access to the the PPrASIC readout and read-back data[4]. The information provided by the RateMeter and Histogramming blocks is also readout via serial interface. The RateMeter accumulates the data and calculates the event rate, while the Histogramming block fills the memory with energy histograms. Both blocks accumulate the data for a predefined programmable number of bunch-crossings. The readout procedure of these blocks is done independently from the Level-1 Accept, as they provide non-event based data i.e. these data can not be assigned to a single bunch-crossing.

4.3 MCM test environment

4.3.1 MCM test setup

The test environment is based on the VME-infrastructure, which provides computer-controlled input data generation and output data capture. The following requirements for the MCM testing environment have been formulated and later on been implemented in the hardware infrastructure:

- Provide the source of analog signals as input to the MCM.

---

[4] Data containing current PPrASIC configuration information, register settings, PPrASIC memories content are referred to as read-back data. These data can be written in the PPrASIC or read out via serial interfaces.

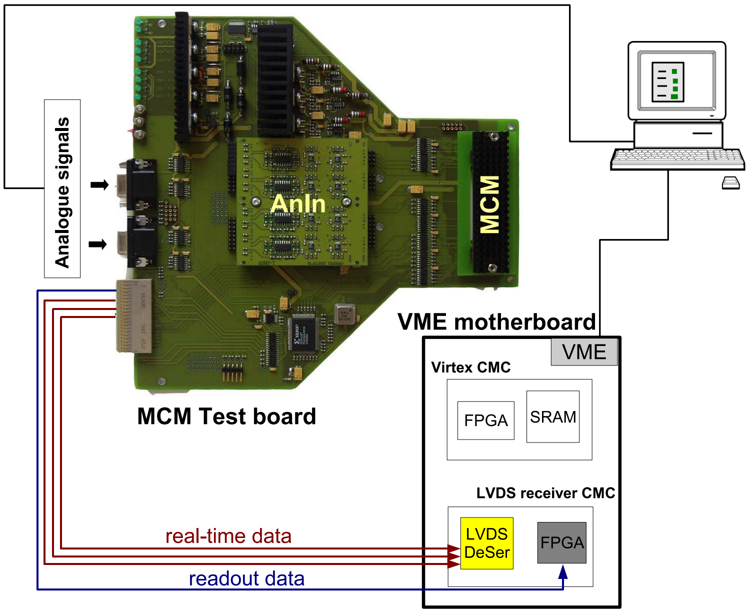

Figure 4.4: MCM test-setup.

- Provide the clock at the LHC frequency of 40.08 MHz.
- Provide the access to the MCM readout and real-time data.
- Provide the artificial L1 Accept signal in order to perform readout of the PPrASIC.
- Synchronise real-time data with L1 Accept in order to perform a comparison of the readout and real-time data coming at the same clock tick.

The hardware infrastructure consists of:

- a **VME crate** with a general purpose motherboard holding two daughter boards: LVDS receiver Common Mezzanine Card (CMC) and Virtex CMC,
- a specially developed **MCM Test Board**,
- a standard graphics card of a personal computer used as **analog signal generator**.
- a **computer**, on which the test software is running.

The MCM test-setup is shown in Figure 4.4.

MCM test board

The main block of the test setup is the MCM Test Board. It emulates the MCM environment on the PPM and holds two components of the final Pre-Processor Module: an Analog Input Board and the MCM to be tested. It also contains the power block where the appropriate voltages for the MCM are generated, four differential amplifiers, which convert the incoming unipolar signal to the differential input for the AnIn board, and the timing block. The timing block consists of the PLL[5] and a 40 MHz quartz clock. The task

---

[5] Phase-locked loop

of the PLL is to generate a stable 40 MHz clock for the whole test system synchronous to the graphics card clock. For this purpose the analog signals generated by the graphics card are used as reference frequency by PLL. The quartz clock is implemented in order to provide a clock for the MCM, independent from the input signal from the graphics card.

The SPI bus provides a communication to the DAC registers on the AnIn board, in order to set the threshold value for External BCID discriminator and offset for the pulse. The I^2C bus controls the PHOS4 settings on the MCM and the ADC on the test board which provides power and temperature monitoring of the MCM.

VME crate system

The access to the MCM output data is provided by the VME crate system. The system consists of the VME crate which hosts a general purpose motherboard. The motherboard carries two CMC cards and a FPGA (Xilinx XC4010XL). This FPGA is connected to the VMEbus through a 32 KByte Dual-Ported Memory module (DPRAM). The XC4010XL can be loaded by the computer via the DPRAM with instructions and data. It can either transfer or receive data from CMCs and acts as a controller and configuration unit for the FPGAs located on CMCs. The LVDS receiver CMC carries four deserialiser chips (DS92LV1024) for transformation of the LVDS serial data stream back into 10-bit parallel data words and FPGA (XCV50E) to handle readout and configuration data. The Virtex CMC card carries FPGA XCV300 and a 1MB Static RAM (SRAM) accessible through the XCV300 for buffering fast data of the real-time path.

The analog pulses from the signal generator are sent to the analog input of the Test Board where they are transformed from unipolar to differential form. The An-In board conditions the pulses and sends them to the MCM for further processing. The MCM generates readout and serial real-time data as described above. The output of the real-time path is received by the LVDS deserialiser chips on the receiver CMC. The data of the readout path are received by a XCV50E, on the same CMC card. The data received by the LVDS receiver CMC are transmitted to the Virtex CMC card and buffered in 1MB SRAM waiting to be read out. Finally the data from both, the real-time and the readout path, are sent via XC4010XL on the motherboard to a Dual Ported RAM (DPRAM). This memory is read out via VME Bus and the data are transmitted to a computer, where they are analysed.

4.3.2 Analog pulse generation with a graphics card

The choice in favour of a graphics card as signal generator was done because it provides an easy and flexible way to generate the required analog signals for MCM testing. The generation of the input signals to the MCM test board is performed by the standard graphics card Matrox Millennium G450 DH. Different analog pulses required to test different functions of the MCM can be easily simulated by card programming. The card provides independent signal outputs to the two monitors via two VGA[6] connectors. Each analog output comprises three analog signals (red, green, blue) and two digital signals for horizontal and vertical synchronisation. The amplitude range for each analog signal coming from the card is 0 - 700 mV. This range can be programmed with an 8-bit word. Thus, the amplitude accuracy one can achieve is 2.7 mV per step.

---

[6] Video Graphics Array

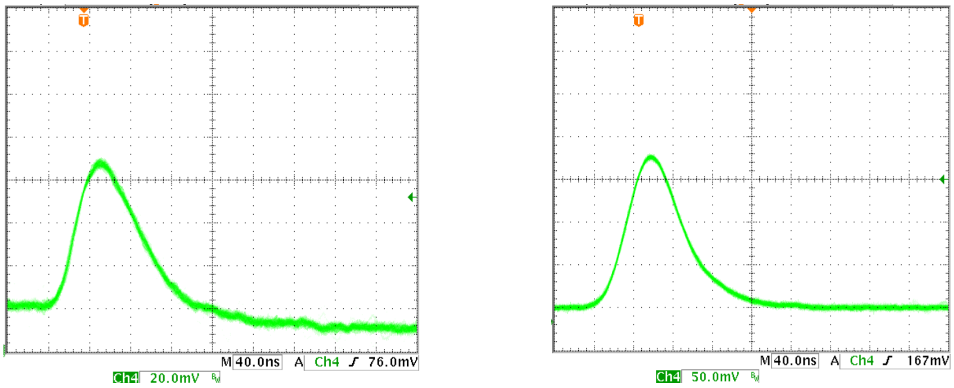

a) b)

Figure 4.5: HEC and TILECAL pulses simulated by the graphics card: a) HEC pulse induced by the electron of 148 GeV; b) TILECAL pulse induced by the electron of 180 GeV.

Having a clock pixel rate of 200MHz, the graphic card is able to address a single pixel within 5 ns. Thus, to simulate a rising edge of the calorimeter pulse of ∼ 40-50 ns, eight to ten pixels have to be programmed.

The digital signal for horizontal synchronisation is used as a reference for the AnIn PLL to produce a 40 MHz clock. However, the PLL has a jitter which is about 2-3 ns, resulting in jitter of the 40MHz clock. Thus the FADC sampling position can be set with an accuracy of 2-3 ns. As a consequence it introduces a significant uncertainty on the measurements using the analog pulses.

The signal generator is programmed to generate the expected pulse shapes, based on data obtained from test-beam studies and special test vectors. In the test beam several HEC, Tile and EMBarrel modules were assembled. Electron, pion and muon test-beams were used for studies as well as calibration signals produced by the calorimeter pulse systems. A few hundred analog calorimeter signals were recorded during test beam runs on a oscilloscope Tektronix TDS3034. For each pulse a file was written with 10000 voltage values which correspond to a signal amplitude with a time resolution of 200 ps in case of HEC and TILECAL pulses. As the time resolution of the graphics card is 5 ns the mean value of the voltages in a range of 5 ns was used to program the graphics card.

The pulses generated by the graphics card using the data from test-beam and read out from the inputs of the An-In board with an oscilloscope are shown in Figure 4.5. On both plots the pulse amplitudes in mV are drawn against a time scale. A single unit of time has a 40 ns length. The HEC pulse induced by an electron of 148 GeV is shown in Figure 4.5a), while the TILECAL pulse caused by a 180 GeV electron is shown in Figure 4.5b). One can see that both signals generated with the graphics card have shapes similar to the original calorimeter pulses shown in Figures 3.2 and 3.3 in section 3.2. A rise time of ∼ 50 ns for the pulses generated by graphics cards shown in Figure 4.5 is close to the expected rise time of the calorimeter pulses. The similarity between original calorimeter pulses and simulated ones gives a good reason to use the graphic card as programmable pulse generator for MCM testing. A detailed study of the pulses generated by the graphics

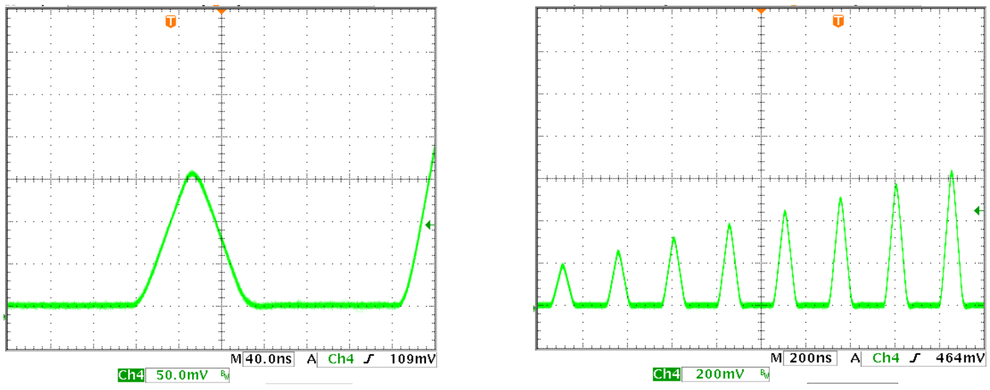

a) b)

Figure 4.6: The artificial triangular pulse with peaking time of 50 ns a) and a ramp of these pulses b).

card can be found in [60].

Based on the analysis of the shapes of HEC and TILECAL pulses an artificial triangular pulse has been constructed. This pulse has the same peaking time of $\sim$ 50 ns as the original calorimeter pulses. In order to study the PPrASIC performance in the whole dynamic range of trigger tower signals up to saturation level this artificial pulse has been linearly scaled. A single triangular pulse and the ramp of the scaled pulses are shown in Figure 4.6.

4.3.3 Level-1 Accept generation

The content of the PPrASIC pipeline memories can be read out only upon the Level-1 Accept signal receipt. The L1Accept signal generation is implemented in the hardware. The period of L1Accept generation equals to 8.3 ms, and the L1Accept signal can be associated to any clock tick within this period. The real-time data writing procedure to the 1MB memory on the CMC card is synchronised with the L1Accept. This synchronisation gives an important possibility to make a comparison between readout output and real-time output using the identical data. Many developed MCM tests use this comparison in order to localise a possibly malfunctioning block on the MCM.

4.4 Functional tests

4.4.1 The DAC and FADC dynamic range

The tests described in this section have been carried out in order to check the linearity and measure the dynamic range of the AnIn board DACs and MCM FADCs. These tests include a number of analog and digital measurements like voltage scan, DAC scan, FADC scan etc. All voltages have been measured with a digital voltmeter.

The 8-bit DAC on the AnIn board can be programmed with a 2.4 mV/step resolution. In Figure 4.7 the AnIn output voltage is depicted as a function of the DAC offset applied

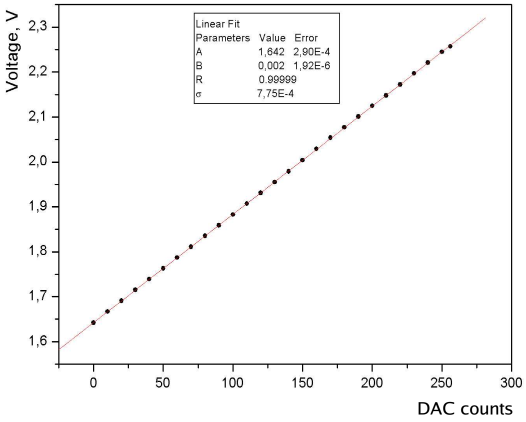

Figure 4.7: The AnIn output voltage as a function of the DAC offset applied to the incoming DC signal.

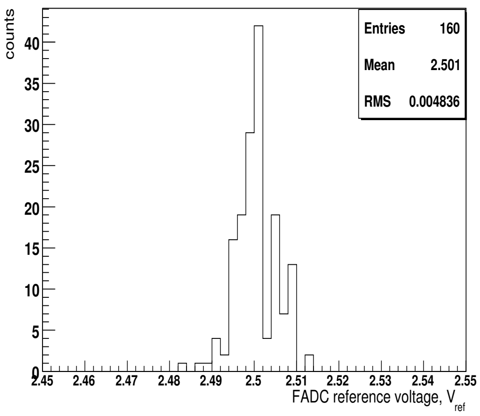

Figure 4.8: FADC reference voltage distribution for 41 MCMs.

to the incoming DC voltage. Figure 4.7 shows the DAC linearity in its dynamic range i.e. within 1.65 – 2.26 V.

The FADC voltage reference V_{ref} is an important FADC characteristics, which can affect the FADC gain error and offset error. The voltage reference for 160 FADCs is shown in Figure 4.8. The plot shows that V_{ref} is 2.5 V and has an error less than 0.4%. Figure 4.9a) depicts the FADC counts versus MCM input voltage. One has to take into account that the input voltage to the MCM is set to be 20% above the FADC window of 1 V, because of the presence of low-pass filter on the MCM balcony. It is seen from the plot – while the FADC voltage range is 2 – 3 V, the MCM input voltage window is 1.9 – 3.1 V.

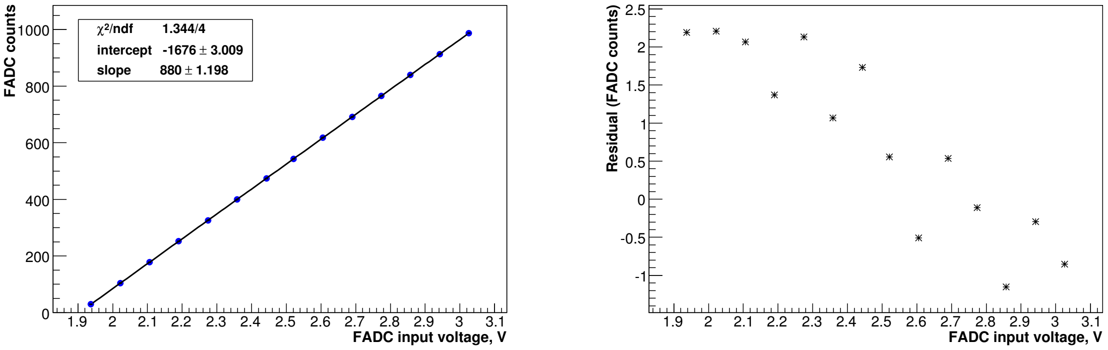

a) b)

Figure 4.9: a)FADC counts vs. MCM input voltage. b) Residuals from a linear fit.

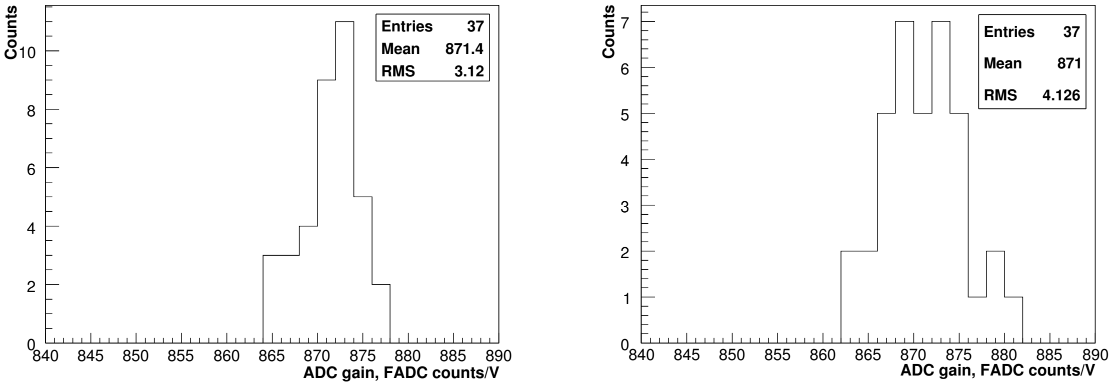

a) Channel 1

b) Channel 3

Figure 4.10: FADC gain distributions: a) for MCM channel 1; b) for MCM channel 3.

Figure 4.9b) shows the residuals from a linear fit.

The FADC gain has been measured for first and third channels in 37 MCMs. Gain distributions are shown in Figure 4.10. The gain error is smaller than 1% in the full dynamic range for both channels.

4.4.2 The PHOS4

The main function of the PHOS4 is to shift the FADC digitisation strobe in 1 ns steps within one bunch-crossing, in other words to perform fine-tuning of timing. This fine-tuning will allow the FADC to sample the pulse at its maximum. As a consequence of this

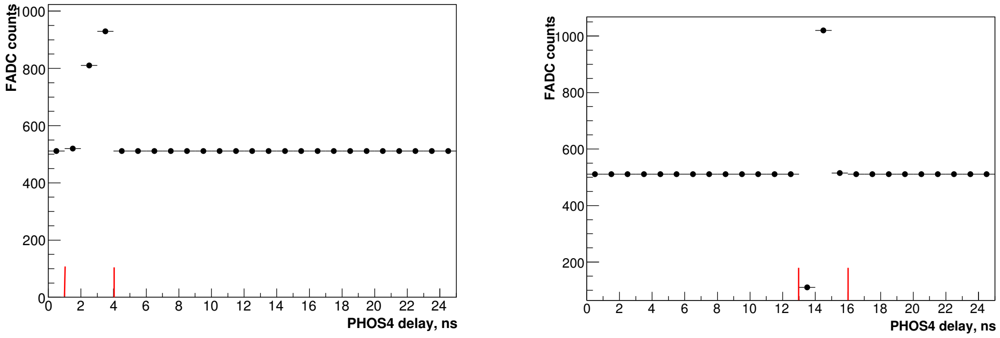

a)

b)

Figure 4.11: PHOS4 scan: a) FADC data latched with positive PPrASIC edge; b) FADC data latched with negative PPrASIC edge.

tuning the sampled digital data could be latched by the PPrASIC at the time when they are in transition from 0 to 1. During the transition the data don't have any fixed value, in other words they are unstable. In order to overcome this problem the PPrASIC can be configured to latch the data at the rising edge (positive edge) or half a tick later at the falling edge (negative edge). Assuming that FADCs have the a fixed time delay, one can determine the region of unstable data and apply the combination of PPrASIC latching edge and PHOS4 delay in order to avoid this region. The aim of the PHOS4 test is to find this combination.

The appropriate input signal for the PHOS4 test is a DC offset in the middle of the FADC range, i.e. the signal which corresponds to 511 FADC counts. The probability of the MSB bit changing in the presence of small noise is higher than for lower or higher DC values. Thus, the choice of the signal exactly in the middle of the FADC range increases the sensitivity of the test.

The PHOS4 scan is performed for positive and negative latching edge of the PPrASIC. The results are shown in Figure 4.11. Table 4.1 summarises the PHOS4 positions with transitory data:

Table 4.1: PHOS4 delays which produce unstable data for positive and negative PPrASIC latching edge.

Edge	**PHOS4 Delays, BC**
Positive	1,2,3
Negative	13,14,15

4.4.3 The FADC

The goal of the FADC test is to check that all the bits in a 10-bit data represent input voltage correctly. A severe signal corruption can happen if one or a few bits, especially MSBs, do not flip and stick at a fixed 0 or 1 state. The test described below has been developed in order to identify these "stuck" bits and to sort out faulty FADCs.

The test procedure consists of two steps:

- Accumulation of the FADC data.
- Analysis of the data: calculation of the flips for each single bit and comparison of the results with expected values.

The analog pulse used in the FADC test is shown in Figure 4.12. The choice of this input signal makes the test procedure quite simple and can be understood from the following considerations. The waveform consists of two parts: top flat DC offset in the middle, and two bottom flat DC offsets on the sides. The pulse is generated repetitively. By sampling the data at the top offset the FADC produces the maximum digital output code of 1023 or 11 1111 1111 in binary format. By sampling at the bottom the FADC produces 0 output. Thus, all bits are forced to flip. Comparing the number of flips for some predefined number of samples with expected values one can determine the hanging bit position.

The detection of FADC failures can be done by monitoring the PPrASIC output data streams: readout and real-time. As was described in section 4.2 the PPrASIC FADC

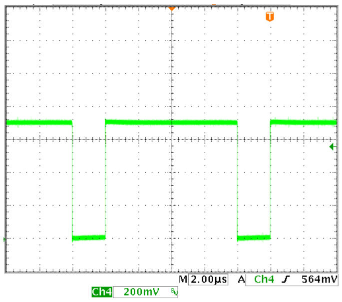

Figure 4.12: Analog pulse for FADC test.

pipeline memories contain the 10-bit FADC data which can be read out via the serial interface. In order to get 10-bit FADC data in real-time path one has to configure the PPrASIC to run in transparent (bypass) mode. In this mode the PPrASIC delivers FADC 10-bit data instead of 8-bit BCID results.

The comparison between the readout data and real-time data also gives a possibility to exclude the FADC as a faulty block in the processing chain and to point another block as a faulty one. For example, a situation can happen where the readout data are correct, but the real-time data are incorrect. It is obvious in this case that the FADC delivers correct data and the faulty functional block which corrupts the real-time data could be the serialiser chip on the MCM. The confirmation of this assumption has to be done by the other tests which are dedicated for the detailed testing of the real-time output data.

4.4.4 The Serialisers

The performance and quality of MCM serialiser cable drivers have been tested using the common quantitative estimation method called Bit Error Rate Testing (BERT). BERT is applied in order to count the number of erroneous bits received during digital data transmission. The Bit Error Rate (BER) is defined as the ratio of erroneous bits to the total number of bits transmitted:

$$BER = \frac{N_{error\ bits}}{N_{bits}} \tag{4.1}$$

The common limits for the BER measurements are set to the following values [61]:

- One or less errors per $1 \times 10^{+12}$ bits sent.
- One or less errors per $1 \times 10^{+14}$ bits sent.

Since the BER is a statistical quantity, the exact BER value can be measured only with infinite number of bits transmitted. In reality only estimation of BER can be done with a given CL[7]. It is obvious that the more bits transmitted the higher accuracy for the BER estimation can be reached. According to [62] the measurement time needed to reach the desired CL can be calculated as follows:

$$t = -\frac{(1 - CL)}{pR}, \tag{4.2}$$

where the t is the time of measurement, p is the limit of measurements to be reached, R is the transmission bit rate.

---

[7] Confidence Level

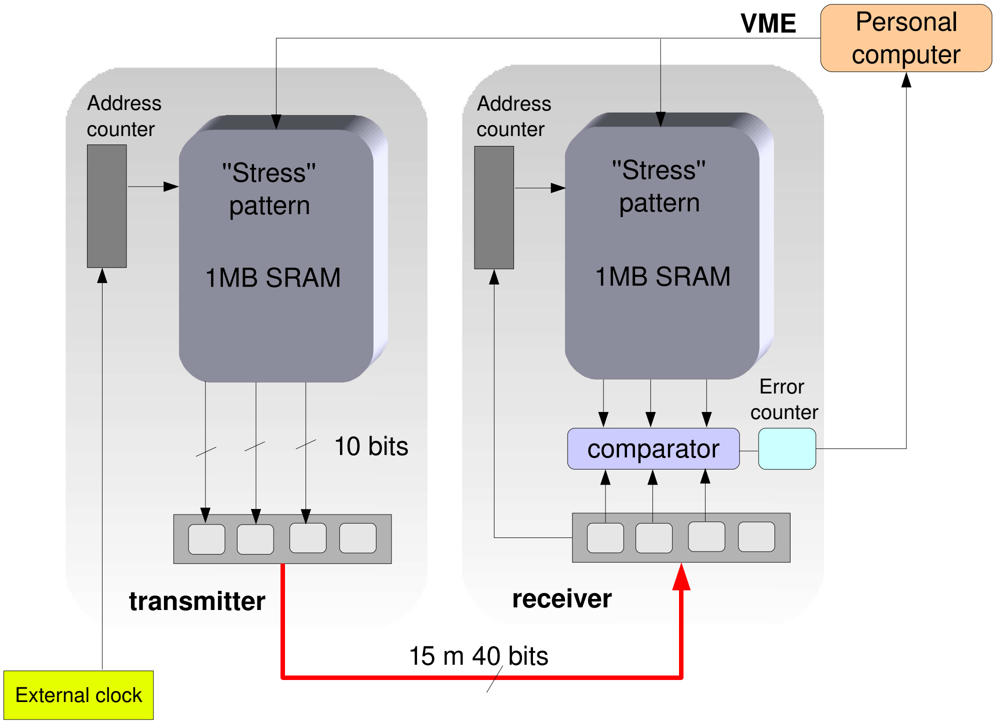

Figure 4.13: The LVDS comparison scheme.

The test VME infrastructure used for LVDS tests is similar to the MCM testing set-up with several distinctions. It consists of two general purpose motherboards. Each motherboard carries two CMC daughter boards. The CMC card on one motherboard acts as a LVDS transmitter. It carries four serialiser chips, a pre-emphasis circuit which improves the data integrity and FPGA (XCV50E) which fanouts the four incoming signals in the 16 outgoing ones acting as a prototype of the LCD card. The serial signals are transmitted via 15 m long shielded parallel 4 twin-pairs cable assemblies. The LVDS receiver board using four deserialiser chips (DS92LV1024) receives the LVDS serial data stream and transforms it back into parallel data. There is a 1 MB SRAM on both receiver and transmitter side which is filled with test patterns.

The test procedure is based on a hardware comparison of sent and received data. At the beginning two SRAMs are filled with the same “stress” pattern generated by the software running on a personal computer. This “stress” pattern consists of the following words in hexadecimal format:

- 0xAAAAAAAA
- 0x55555555
- 0xFFFFFFFF
- 0x00000000
- Pseudo-random pattern

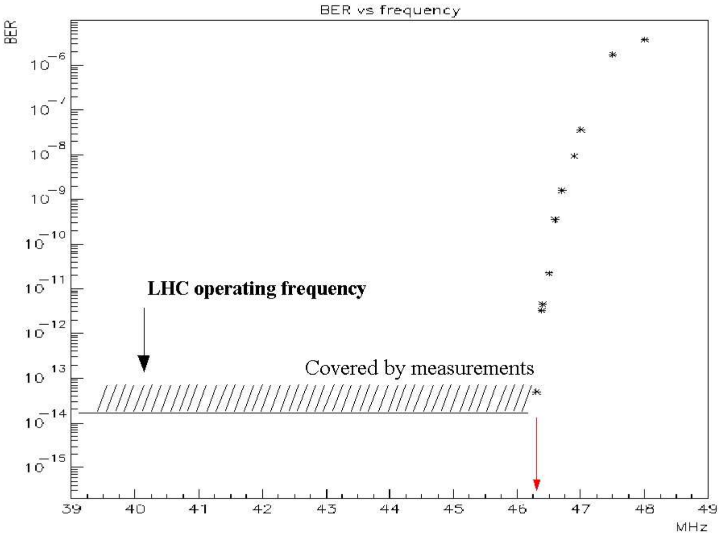

Figure 4.14: BER for 4-fold fanout.

After the “lock” of the LVDS link is established and memories are loaded, the 10-bit data are transmitted via a 15 m long cable. The SRAM has a 32-bit width, that is why only a 30-bit comparison is possible. The scheme of data comparison is shown in Figure 4.13. The transmitter generates a clock signal using an external clock as reference. The frequency range from 39 MHz to 49 MHz to be studied in the test is defined by this external clock. The incoming 40-bit data are deserialised and compared with data in the receiver memory by a comparator. In case an error occurs, the error counter is incremented. Two series of measurements of BER against frequency have been carried out with a 2-fold fanout and a 4-fold fanout. The intention was to find the critical point on the clock scale where the BER starts to increase and to make sure that at the LHC working frequency (40.08 MHz) the BER is sufficiently small.

The duration of measurements has been calculated taking into account that for BER we have to reach the limit of less than 1×10^{-14} within CL=95%. The result for 4-fold fanout is shown in Figure 4.14.

One can see that the measured BER remains lower than the limit of 10^{-14} at the LHC frequency and beyond. A rapid increase of BER starting at clock frequencies higher than 46 MHz is observed.

4.4.5 The PPrASIC

Power

The MCM is supplied with three different power levels for different electronic components:

- **Digital power supply:** Digital V_{cc}= +3.3 V. Powering the PPrASIC, the serialiser chips, PHOS4.
- **Analog power supply:** Analog V_{dd}= +5.0 V. Powering the FADCs.
- **Analog power supply:** Analog V_{cc}= +3.3 V. Powering the serialiser chips.

A diode on the PPrASIC provides temperature measurements. The three MCM voltage and current values as well as the temperature of the PPrASIC are digitised by ADC (MAX128) on the test board and can be read out via an I^2C bus.

The power test checks that the voltage and current values are within the reference boundaries. For the current values these boundaries are defined to be ±15% from the nominal current values. The power test is the first test carried out in the MCM serial testing procedure. The existance of some serious electrical problems, like short circuit on the MCM is indicated by the power test.

Registers and Memories

All configuration data are written into the PPrASIC registers. The registers can be read and written via the serial interface. Each PPrASIC channel is configured separately with a set of 58 channel registers. In addition to the four sets of channel registers, there are two blocks of global registers – one block per one serial interface. There are 8 registers in each block.

The register test includes several procedures. All checking procedures follow a similar action list:

- Load test pattern to the all registers.
- Read back the registers.
- Perform a comparison between captured register values and expected ones.
- Increment error counter if an error is found.

A list of tests performed on each register:

- Checking the default register settings.
- Read/write test-pattern given in hexadecimal format as 0xffff.
- Read/write test-pattern given in hexadecimal format as 0x5555.
- Read/write test-pattern given in hexadecimal format as 0xAAAA.
- Read/write zero test-pattern.

The register test is passed if all register values match the expected ones in all testing.

The PPrASIC contains four different memory blocks per channel. These memory blocks can be summarised as follows:

- **Lookup Table memory**. The LUT is a 1024×8 bit memory for fine calibration of data and mapping of 10-bit words to 8-bit words.
- **Playback/Histogramming memory**. This 256× 11 bit memory is used by the Histogramming Block for storing the accumulated data. The memory can also be used in playback mode, when no data acquisition takes place for playback of 10-bit digital data and an external BCID bit.
- **Pipeline memory for raw data**. The 128× 11 bit memory is used as storage for FADC data which can be read out via a serial interface.

- **Pipeline memory for BCID results**. The 128× 11 bit memory is used as continuous storage for BCID results which can be read out via serial interface.
- **RateMeter memory block**. This read-only memory is filled with RateMeter output data.

The LUT and Playback memories are tested with four test-patterns. The procedure is similar to that in the register test. As a first step the test-patterns are loaded into the memories, then the memories are read out and the content is compared to the expected one. The procedures are given below:

- "Walking-ones" test. The test starts by setting the LSB of the single word in the memory to 1, while holding other bits at zero. For each step in a cycle the 1 moves to the next higher bit in the word.
- "Walking-zeros" test. The same as the above "walking-ones" test, but here, the zero "walks".
- Pseudo-random pattern test. For the pseudo-random pattern generation the Linear Feedback Shift Register (LFSR) technique is implemented in software.
- Checkered test. The memories in this test are loaded with the checkered patterns like 010101010.

The readout pointer in pipeline memory of the PPrASIC moves at every bunch-crossing from one position in the memory to the next. In the debugging mode the pipeline memory can be completely read out. Before reading the whole content of the pipeline memory, it has to be stopped first. Every time the readout pointer stops at a different position, which can not be pre-defined. Taking in to account this condition the following test-patterns are used to test pipeline memories:

- Checkered test-pattern.
- Address test-pattern 1..128.
- Zero and 11111111111 test-patterns.

The FIFO

The FIFO[8] is a data buffering block implemented in the PPrASIC to perform coarse alignment in time of the incoming data. The trigger algorithms require that all incoming TT signals originating from the same bunch-crossing must be synchronised to each other, in other words they should come at the same time to the trigger stage. The differences in cable lengths is the main factor that makes the incoming signals asynchronous to each other. The FIFO equalises the signal propagation in time.

The FIFO depth is 16 clock ticks. Depending on the register **ReadoutSource** the input data to the FIFO can be 10-bit FADC data and an external BCID bit or playback memory data. The FIFO delay for these input data is programmable with a resolution of one bunch-crossing. By default the FIFO has a one bunch-crossing delay for any input data. The FIFO can be bypassed by setting the registers **SyncBypassData** and **SyncBypassBcid**.

The FIFO test sequence consists of several steps and can be described as follows:

---

[8] FIFO – First-In-First-Out

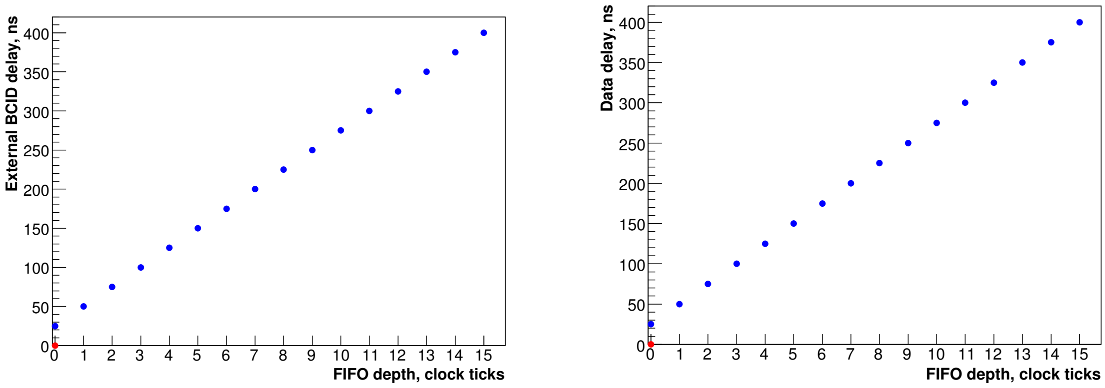

a) b)

Figure 4.15: FIFO depth: a) External BCID bit delay as a function of FIFO depth. b) 10-bit data delay as a function of FIFO depth.

- Load the playback memory with a test pattern which consists of:
  - two 10-bit data words, which cover all possible bit flips. These words are in binary format 10 1110 1110 and 01 0001 0001.
  - an 11-bit data word in order to check the external BCID bit: 100 0000 0000.
- Program the FIFO depth and check for delayed data and the delayed external BCID bit for each step.

The results of this FIFO scan for 10-bit data and external BCID bit are shown in Figure 4.15. The red point denotes no delay and corresponds to the FIFO bypass mode. The plots show that FIFO works properly.

The FIR filter and Drop-bits module

The main task for the FIR filter is to prepare non-saturated pulses for the Peak Finder BCID algorithm by weighting the samples. For each bunch-crossing the FADC data from two following and the two previous bunch-crossings are held and multiplied with weights, that are stored in five registers. All five registers are 4-bit wide. While the middle three registers can contain values of the coefficients in a range from 0 to 15, the first and the last registers cover the range from -7 to +7, thus they can contain also negative coefficients. A detailed description of the FIR filter and its implementation in the PPr system can be found in [59, 63]. The five weighted samples are summed and stored in a 16-bit output word. The 16-bit output data are propagated to the Peak Finder block and to the Drop Bits block. The Drop Bits block defines the 10-bit word out of the 16-bit data coming from FIR Filter. The start position of this 10-bit word can be adjusted by cutting the LSBs of the 16-bit word. The number (0–6) of LSBs to be cut is defined by the register **StartBit**.

The FIR Filter and Drop Bits blocks are tested with two pulses which are loaded into the playback memory:

- A simple symmetric pulse in decimal format: 1 10 100 10 1.
- An asymmetric pulse covers all bits flips in decimal format: 75 341 1023 682 269.

The combinations of the pulses, coefficients and Drop Bits value checked in the test is given in the Table 4.2. For each combination the PPrASIC output data are compared with the expected values.

Table 4.2: The combinations of the pulse, coefficients and Drop Bits value tested.

Pulse	FIR Coefficients	Drop Bits
1 10 100 10 1	00100	0
	1 1 1 1 1	0
	1 0 2 0 1	0
	1 2 3 2 1	0
	0 1 3 1 0	0
	-1 1 1 1 -1	0
	-3 2 5 2 -3	0
	-7 0 15 0 -7	1
	7 15 15 15 7	2
	7 15 15 15 7	3
	7 15 15 15 7	4
	7 15 15 15 7	5
	7 15 15 15 7	6
75 341 1023 682 269	7 15 15 15 7	6
	4 9 14 12 3	5
	-6 8 13 6 -4	5

Bunch-crossing Identification Logic

Before the description of the tests, a short introduction to the BCID algorithms and BCID logic is given below.

The typical LAr and TILECAL pulses have a peaking time of 40-50 ns, which means that calorimeter pulses are several times longer, typically 100 ns, compared to the bunch-crossing period of 25 ns. In order to make a decision for every bunch-crossing the trigger needs to “know” the transverse energy in each trigger tower uniquely associated to a given bunch-crossing. This is achieved by the BCID logic implementation in the Pre-Processor system.

The main task of the BCID logic is to recognise the pulse and assign it uniquely to the bunch-crossing at which the interaction occurred and extract the associated transverse energy. This task is absolutely non-trivial, taking into account the demanding requirement to the BCID logic to be efficient in the entire energy range, provided by the ATLAS calorimetry.

The pulse shapes are quite different for non-saturated pulses with small amplitude and for saturated pulses. The main distortion effect for low energetic pulses is noise coming from pile-up events and electronics, while the pulses corresponding to high E_T deposits are affected by saturation. Saturation can happen at any stage of analog signal processing in front-end electronics. At the PPr stage the analog pulse is cut off digitally by the FADC window limit, which corresponds to $\sim$ 250 GeV. The task of the BCID in this case is to restore the peak position of the truncated pulse. In order to handle the non-saturated and saturated pulses separately, two different BCID algorithms are implemented in the PPrASIC.

The non-saturated BCID algorithm combines FIR Filter and Peak Finder processing stages. The weighted samples after the FIR Filter come to the Peak Finder. The Peak Finder algorithm analyses three successive data samples and gives a positive result for the sample S_n if the following condition is satisfied:

$$S_{n-1} < S_n \geq S_{n+1}, \tag{4.3}$$

where S_{n-1} and S_{n+1} are the samples in the previous and the following bunch-crossings.

The saturated BCID algorithm is implemented in the SatBCID functional block. Based on the fact that larger saturated pulses reach the saturation level faster than the smaller ones, the algorithm analyses the slope of the pulse rising edge, assuming that the shape of the rising edge is not distorted by the signal saturation. The algorithm is activated when the saturation level is reached by any sample. It takes two samples from the previous bunch-crossings to the bunch-crossing, where the saturation has been detected, and compares them to threshold values. As a result the algorithm produces 1-bit output, which shows the correct bunch-crossing. The simple logic of the saturated BCID algorithm is shown in Table 4.3. The Table 4.3 shows the identified BCID bunch-crossing (two right most columns) depending on the fulfilled saturation and threshold conditions (first three columns). The S_{sat} is the sample where the saturation found, and S_{sat-2}, S_{sat-1} are two previous samples, which are compared to the two low and high thresholds – s_{low} and s_{high}. The identified bunch-crossing t_{sat} corresponds to the S_{sat} sample,while the t_{sat+1} is the next bunch-crossing. A detailed description of the saturated BCID implementation can be found in [66].

Table 4.3: Logic of the saturated BCID algorithm. Three first columns indicate saturation level and threshold conditions which have been fulfilled ("1") or not fulfilled ("0") or ignored ("X"). The two most right columns show the identified bunch-crossing ("1") and no BCID result ("0") [66].

S_{sat} $\geq$**sat. level**	$S_{sat-2} > s_{low}$	$S_{sat-1} > s_{high}$	t_{sat}	t_{sat+1}
0	X	X	0	0
1	1	1	1	0
1	0	1	0	1
1	X	0	0	1

The values of the saturation level as well as low and high threshold are programmable via PPrASIC registers. The settings of these registers are a matter of the saturated BCID algorithm calibration and can differ depending on the calorimeter type and region.

The aim of the saturated BCID test is to determine the correct functionality of the logic implemented according to Table 4.3. In order to check all conditions in Table 4.3

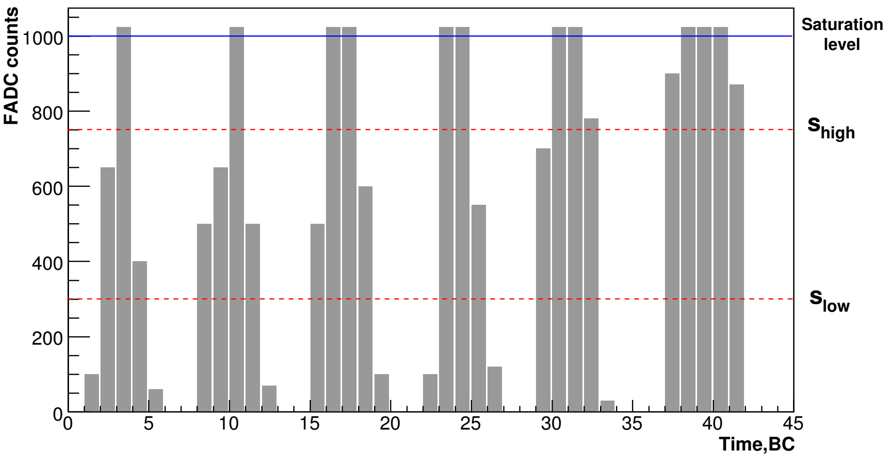

Figure 4.16: An example of saturated pulses used for testing the saturated BCID algorithm.

with different saturation level and thresholds values, 10 different saturated pulses have been loaded into the playback memory. An example of pulses used in the test is shown in Figure 4.16.

In the testing procedure the result of the saturated BCID algorithm is compared to the expected one. The tests have shown the correct functionality of the algorithm.

The three "BC Marks" indicating the bunch-crossings found by BCID algorithms enter the BCID DecisionLogic block. The BCID logic divides the whole energy range into three sections:

- High-energy range.
- Middle-energy range.
- Low-energy range.

The borders between these sections can be adjusted by setting two 10-bit registers **EnergylevelLow** and **EnergylevelHigh**. For each section an 8-bit register **BcidDecision** sets a combination of the BCID results which defines a positive BCID decision for a given bunch-crossing. The combinations of 3-bit results ("BCID marks") from the BCID algorithms, which is used for construction of the 8-bit value for the **BcidDecision** register is shown in Table 4.4.

The construction of the 8-bit decision word is done by setting the bits which correspond to the required BCID result combination. The bits in the 3-bit words are AND'ed. That means for example that the second combination 0 0 1 is "True" only if the external BCID algorithm delivers the result, and it is "False" in any other case. These 3-bit combinations are OR'ed in an 8-bit word. If any of the combinations contained in an 8-bit word is "True" the BCID logic produces a positive decision and assigns the LUT result to the current bunch-crossing. For example, setting the decision word to value 1100 1100 configures the BCID logic to give a positive decision as far as the saturated BCID algorithm delivers a result with any combination of results from other algorithms. If the 8-bit word is set to 0000 0001, the BCID logic will generate a positive decision when there are no BCID

Table 4.4: A combination of 3-bit results from the BCID algorithm which is used for construction of the 8-bit decision word. The first column contains bit numbers in an 8-bit decision word, "PF" denotes the Peak Finder, "SB" denotes the saturated BCID algorithm, "EB" stands for the external BCID algorithm.

	Bits	**PF**	**SB**	**EB**
	0	0	0	0
	1	0	0	1
	2	0	1	0
$\downarrow$ OR	3	0	1	1
	4	1	0	0
	5	1	0	1
	6	1	1	0
	7	1	1	1
			AND $\longrightarrow$	

results from the algorithms at all. This example shows that the BCID logic is very flexible and has to be configured with care.

The BCID logic has been tested using the 30 most probable configurations for each energy range and 21 different pulse types. Each configuration is a set of BCID decision word, external and saturated delay number, decision source type. Digital playback data and analog source have been used. The BCID logic test provides a good possibility to test also three BCID algorithms as they deliver the input data to the BCID logic block.

The thorough tests of the BCID algorithms and BCID logic have provided the evidence of their correct functionality. Later on, the BCID logic test has been implemented in the MCM production test package.

Based on the BCID test procedure described above another BCID test has been developed. The input for the PPrASIC in this test is provided by the analog source, which generates a ramp signal as shown in Figure 4.6b). About 1.4×10^6 analog pulses are processed during the test, and BCID results from each pulse are tested using real-time data path.

The Jet pre-summing and Bunch-crossing Multiplexing

The task of the JetSum block is to form the jet elements. Four 8-bit BCID results are summed together in somewhat different ways, depending on the chosen mode. The format of the 10-bit data words produced in these modes is given in Table 4.5.

All pre-summing modes have been tested using the pulse ramp shown in Figure 4.17. The height of the pulses have been set to predefined values in order to check every bit flip in a 10-bit word. For each pre-summing result also the parity bit [9] is checked.

---

[9] The parity bit implemented in the PPrASIC is an odd type. This bit is set to 1 for zero data. It is set to 1 if the number of ones in 10-bit word is even and to 0 if number of ones is odd.

Table 4.5: Jet pre-summing modes.

Mode	**Non-saturated sum**		**At least one channel saturated**
0	sum < 511	sum ≥ 511	Parity bit is 0, other 9 bits are 1
	9-bit sum + parity bit	9 bits are set to 1 + parity bit	
1	Truncation LSB, add parity bit		Parity bit is 0, other 9 bits are 1
2	10-bit sum, No truncation		All 10 bits are 1

The bunch-crossing multiplexing mechanism implemented in the BCMux block multiplexes the 8-bit BCID results for two channels onto one output. Thus, only two output data streams are used for four channels. The format of the data word for a single bunch-crossing is given in Figure 4.18.

The word comprises the 8-bit BCID result accompanied by the BCMux flag and an odd parity bit as LSB. The multiplexing cycle starts when the BCID result appears in any of the two channels. The output results of multiplexing are sent in two consecutive bunch-crossings. The BCMux flag unambiguously indicates the channel which corresponds to the bunch-crossing containing the BCID result. The three combinations of the BCMux flag which are set in two consecutive words cover the three possible cases which can happen:

1. The BCID result in channel 1 is one tick earlier than the BCID result in channel 2.
2. The BCID result in channel 1 and channel 2 are in the same bunch-crossing.
3. The BCID result in channel 2 is one tick earlier than the BCID result in channel 1.

These three cases and the corresponding BCMux flag combinations are shown in Figure 4.19. These cases have been simulated using the playback memory of the PPrASIC. The tests have shown the correct output to the Cluster Processor for all three cases.

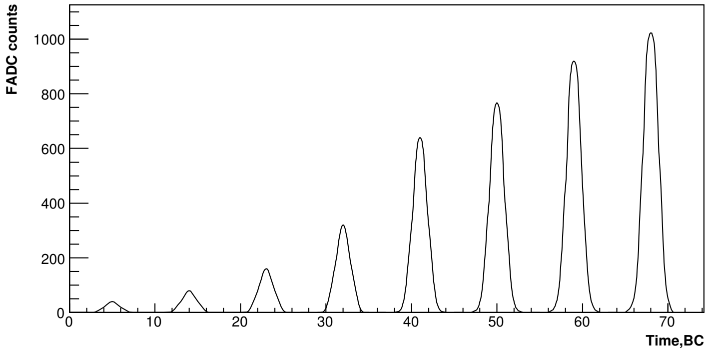

Figure 4.17: Pulse ramp loaded into the playback memory which is used in the pre-summing test for all MCM channels.

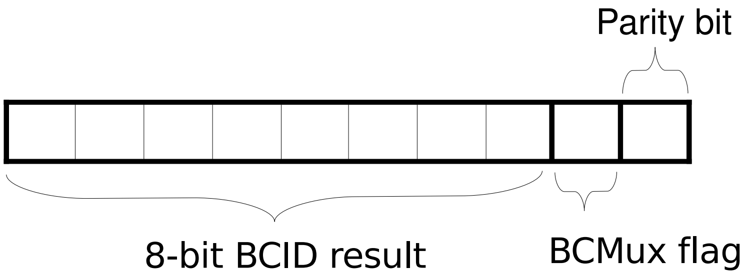

Figure 4.18: Format of data word in the output to Cluster Processor.

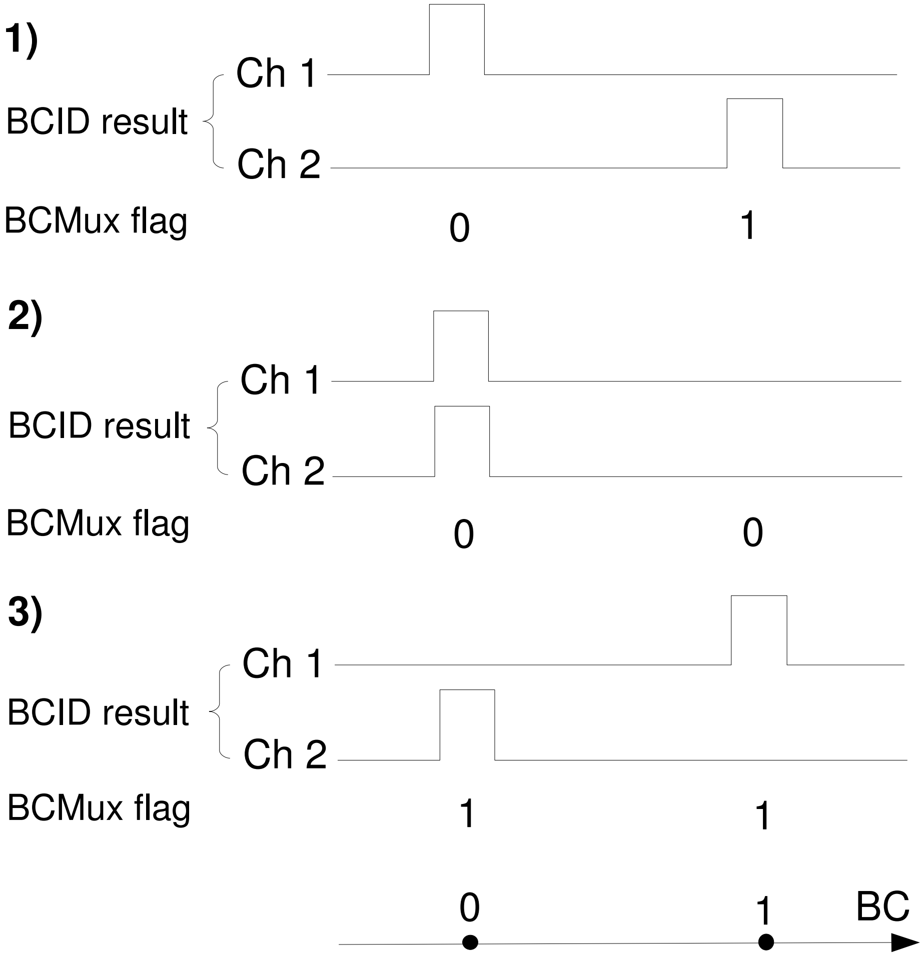

Figure 4.19: Three combinations of the BCMux flag bit in two consecutive bunch-crossings, depending on the BCID result time position for two channels.

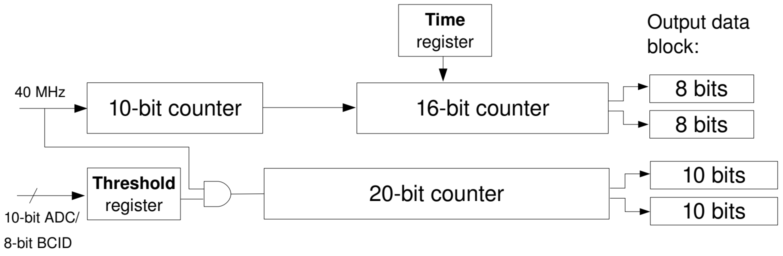

Figure 4.20: Rate-metering block diagram.

Rate-metering and histogramming

The monitoring block of the PPrASIC includes Histogramming and Rate-metering modules. There are 2 sources for Rate-Metering: FADC data and BCID results. The **Rate-Source** register controls which data will be accumulated in Rate-metering. The Rate-metering block diagram is shown in Figure 4.20. As soon as the Rate-metering module is activated by the **RateEnable** register, the data which exceed the threshold settings are counted by a 20-bit event counter. The number of bunch-crossings is counted by two timing counters. The 10-bit counter increments every bunch-crossing. As it reaches the limit of 10 bits the 16-bit counter is incremented. The Rate-metering block doesn't have any dead time, so every bunch-crossing is counted. The Rate-metering module stops counting and provides its data to be read-back in two cases:

- The event counter reaches overflow.
- The 16-bit time counter reaches the value set in the timing register.

A 16-bit threshold can be set in the timing register. This threshold defines the limit of the timing interval with an accuracy of $25.6 \mu s$. The flags "Rate-Metering available" in the Status word indicate that the data can be read. The format of the Rate-metering output data consisting of four words is also shown in Figure 4.20. It includes two 8-bit data words containing time interval value and two 10-bit words corresponding to the 20-bit event number. The Rate-metering block has been tested in all modes with different register settings. An example of one testing measurement is shown in Table 4.6. The FADC data have been used as input source. For the FADC source a DC level test pattern higher than a threshold has been used. The expected output for the event and timing

Table 4.6: Rate-metering register settings and expected and measured output results for FADC data in cases: 0 – timeout condition reached by the 16-bit timing counter, 1 – event counter overflow

Case	**Time register settings**	**Time interval, ms**	**Event counter output exp./meas.**	**Time counter output exp./meas.**
0	3220	~ 82	1000/1000	3220/3220
1	32200	~ 823	$2^{20}/2^{20}$	-/13725

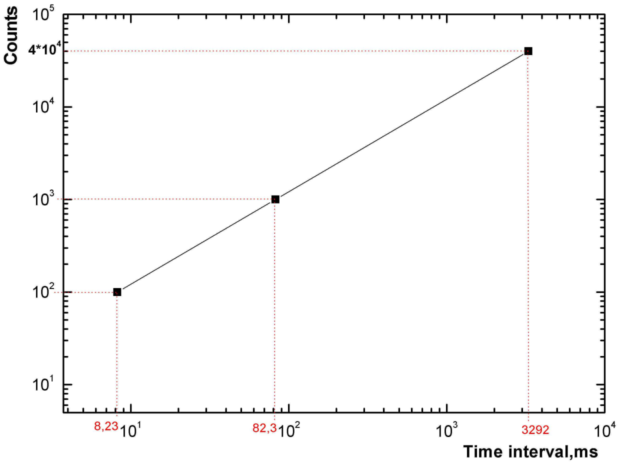

Figure 4.21: Rate-metering event output vs. timing intervals for FADC data source.

counters has been calculated knowing the input test patterns loaded into the graphics card. For the timeout case the sampling rate seen by the Rate-metering module has been 12/ms and for the overflow case 2989/ms.

The events measured by the Rate-metering in three different time intervals in case of timeout condition are shown in Figure 4.21. One can see a proper linear behaviour of the rate-metering module. For tests of Rate-metering with BCID results as input source, a ramp of triangular pulses has been used. The results show correct functionality, too. The Rate-metering module has also been successfully tested using the playback memory, loaded by the ramp and DC level testing patterns. The results are in agreement with the expectations.

The Histogramming module as well as Rate-metering can be fed by two sources of data – 10-bit FADC data or 8-bit BCID results. The 10-bit FADC data are mapped onto 256 locations in the memory by truncation. The three truncation modes implemented in the PPrASIC are given in Table 4.7. According to this table the higher the mode number is, the smaller the energy range the histogram covers with increasing accuracy as the number of bins remains the same.

In case the 8-bit BCID data are used, no truncation is applied. Being activated by the two registers – **HisEnable**, **PlaybackEnable**, the Histogramming module accumulates

Table 4.7: Histogramming modes.

Mode	Truncation	Range, GeV	Resolution, GeV
0	2 LSB	0 - 256	1
1	1 MSB, 1 LSB	0 - 128	0.5
2	2 MSB	0 - 64	0.25

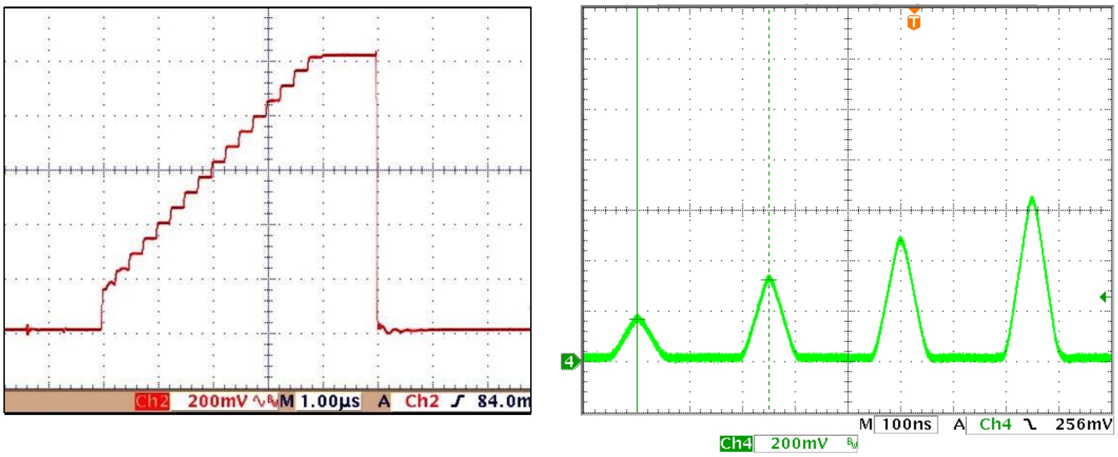

a) b)

Figure 4.22: Analog pulse shapes used in tests of the Histogramming module in two different modes: a) histogramming of the FADC data; b) histogramming of the BCID results.

the data using the same memory as for playback data. The lower limit for the pulses to be histogrammed is set by a programmable threshold written in the register **HisEtThresh**. The time interval during which the histogramming is performed is defined by four 6-bit registers. Two of them designate the 12-bit value of the lower limit, and another two designate the 12-bit value of the upper limit of the timing window. The values of these registers are compared to the 12-bit bunch-crossing counter running permanently in the PPrASIC. The Histogramming is active if the bunch-crossing counter value is within the limits defined by these registers. The input signal is histogrammed by incrementing the corresponding bin. If the FADC data are outside of the histogramming range, the very last bin is incremented in this case. As the playback memory has the 11-bit width, the maximum number of counts in a single bin which can be reached is 2047. As soon as overflow is reached in any of the bins, the histogramming stops and the histogrammed data are ready for readout. The *Histogram Available* bit in the read-back Status word indicates the state of the histogramming block. Histogramming will be activated again only after the memory is read back and cleared.

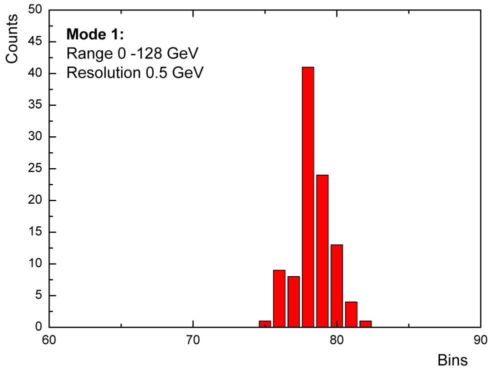

Figure 4.23: Energy histogram of a single step with integral value of 100 counts.

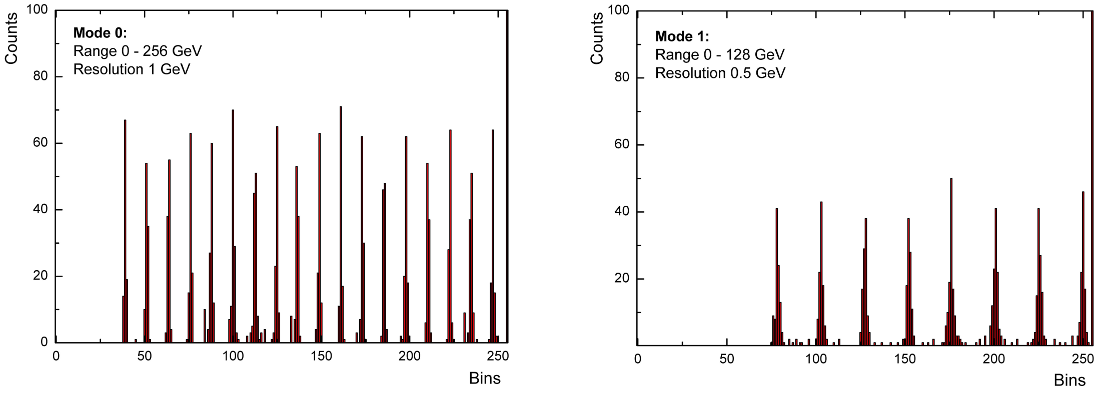

a) b)

Figure 4.24: PPrASIC histogramming in a) mode 0 and b) in mode 1.

The Histogramming module has been tested with both sources of data: raw 10-bit FADC data and 8-bit BCID results. In the FADC mode the step waveform has been taken as input signal as it is shown in Figure 4.22a). This form of the signal has been chosen because of the fact that the Histogramming module has a 10 of bunch-crossings dead time. Setting the step size to 10 bunch-crossings one can expect to have a histogram entry for every step in the signal. The analog pulse ramp has been used as a signal in the BCID mode, is shown in Figure 4.22b). It has been chosen to provide BCID results which are 10 bunch-crossings apart from each other.

The histogramming result for a single step in the step function is shown in Figure 4.23. The number of analog signals generated is equal to the integral value of this histogram. Thus, knowing the exact number of these waveform produced one can test the histogramming module by checking the bin position for each step in the waveform and the number of counts for this step. This approach to the Histogramming testing has been implemented later in the automatic histogramming test.

All modes of the Histogramming module have been successfully tested. Examples of histogramming outputs in modes 0 and 1 are in agreement with expectations shown in Figure 4.24. An automatic test developed and implemented later in the testing software package analyses the content of bins, estimates the correct position of the histogram peaks, checks the threshold settings and limits of bunch-crossing window in all operating modes.

4.5 Results and conclusions

A thorough testing of all functional MCM blocks has been performed. All logic blocks in the PPrASIC have been examined with different test-patterns in all possible modes. The functional tests have confirmed the correct MCM functionality. In order to perform production testing of ~4000 MCMs, all developed testing procedures were combined in the testing software package.

Chapter 5

Large scale tests and production of the Multi-Chip Module

5.1 Tests and test software

A multitude of separate tests were combined in a software package specially developed for the production tests. The tasks of the test software are: a complete test of all functions of the PPrASIC and MCM in an automatic mode, a detection of nonfunctional blocks on the MCM, a provision of a test environment for further investigation of the faulty MCMs. The last two functions are required for the repair cycle where the faulty chips have to be identified and replaced.

The test software consists of three main packages:

- The configuration package.
- The analog signal handler package.
- The test-handler package.

The first package is responsible for register settings used in the tests; the second package contains the pulse library and generates the analog test vectors; the third package configures and runs the tests. The sources of input data can be two-fold: analog or digital. The analog test patterns are used mainly to test the FADCs, BCID algorithms, and histogramming built into the PPrASIC. The digital patterns - pre-loaded in the PPrASIC playback memory - serve to test the digital part of the MCM. The readout and real-time data captured in the memories are compared to each other and to the pre-calculated expectations. Tests of certain functional MCM blocks with both analog and digital input allow to determine any malfunctioning blocks in great detail.

During production tests the software has been used in three main testing modes:

- **PPrASIC Wafer test.**
- **Full MCM Quality Assurance test.**
- **Debugging mode.**

In the "Wafer test" mode only PPrASIC functional blocks are tested. In addition, the software controls wafer-probe station manipulations, namely stepping from die to die. The single Wafer test takes 1 minute per die; testing a whole wafer in one go needs 5 hours.

Figure 5.1: The PPrASIC test-hardware mounted in the wafer-probe station.

In the “Full MCM Quality Assurance test” mode all dice on one MCM are successively tested. This takes 2.5 minutes per MCM. In the “Debugging mode” the software provides an interface which allows the user to configure manually a test procedure with user-defined test patterns. This mode is used in MCM repair cycles, when a complex analysis of the malfunctioning MCM blocks has to be done.

The test software was written in the C++ language using Qt libraries. A graphical user interface provides a test menu-guide for the user. The menus for main testing modes are attached in Appendix B.

5.2 PPrASIC wafer tests

Each PPrASIC die is subject to a full functional test before placement on the MCM substrate. The PPrASIC wafers were tested in the KIP “clean-room” using test-hardware and the wafer-probe station to facilitate stepping from die to die. The MCM test board mounter in the wafer-probe station is shown in Figure 5.1. The test set-up for the wafer test is similar to the set-up described in Chapter 4, with some modifications on the MCM side. For the wafer tests the MCM Test board carries a “Needle Card” connected via an adapter to master MCM with missing PPrASIC. The master MCM holds all other components, while at the PPrASIC place there is an empty hole. The PPrASIC pads are

Table 5.1: Wafer yields and PPrASIC functional errors in three “Production Runs”.

Run	Wafers	Yield	Power errors	Memory errors	Logic errors
1	20	57%	19%	11%	13%
2	14	41%	16%	20%	22%
3	11	26%	14%	38%	22%

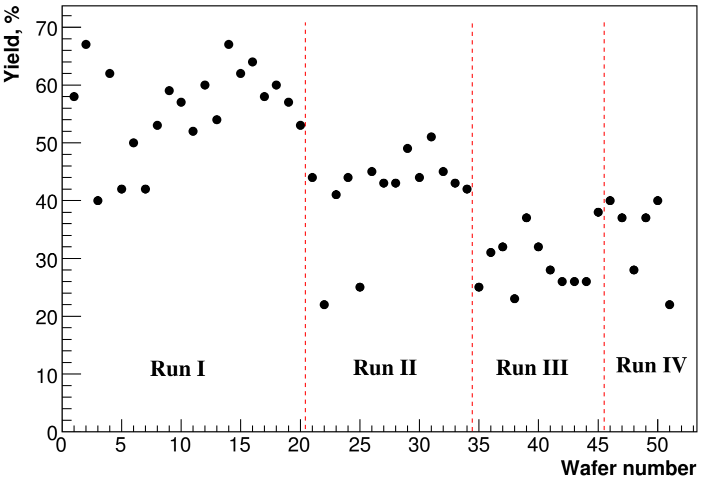

Figure 5.2: Yield of the wafers in the production runs.

bonded to the adapter, which is connected to “Needle Card”. The “Needle Card” has pins to contact all the pads on the PPrASIC die on the wafer.

For each wafer undergoing the test procedure, a wafer map is generated. It contains the test results for each single die using an 8-bit color code. Those dice that passed the test are marked as “Known Good Dice” (KGD) and delivered to the company. There the wafers are cut into individual dice, from which all identified KGD are selected and available for further use. The wafer production has been split in four “Production Runs”. In each “Production Run” a block of wafers has been produced at Austria Micro Systems (AMS) [68] and delivered to KIP for testing. 51 wafers with 9792 PPrASIC dice were produced and tested. Out of this number 4099 dice were found to be KGD, giving a yield of 42%. In Table 5.1 the yield for three “Production Runs” and distribution of errors for

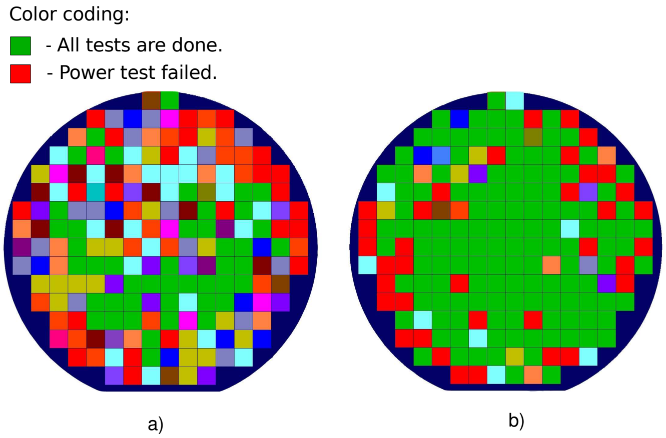

Figure 5.3: Wafer maps: a) The worst wafer from the production; b) The best wafer from the production. The color coding displays the dice passed the test (green) and dice failed (other colors).

the PPrASIC dice is given [64]. The yield distribution for all four "Production Runs" is shown in Figure 5.2. Figure 5.3a) shows the worst wafer with a yield of 22% and Figure 5.3b) shows the best wafer with a yield of 68%.

The KGD have "green" color code, while the other colors represent the combination of errors in the MCM test. For example the "red" color shows that the "Power test" failed etc.

5.3 Multi-Chip Module manufacturing

The base of the MCM is a multilayer high-density printed circuit board (PCB) with microvias for layer-to-layer contact. The PCB has 4 copper layers, 2 epoxide Prepreg[1] layers and 1 FR4 laminate layer. The copper layers of the PCB are interleaved with Prepreg layers and a FR4 core in the center. The FR4 material is made of epoxy resin that saturates woven fiberglass. The required micro vias are formed by laser drilling. The combination of this semi-flexible PCB sticking to a 0,8 mm copper plate - to realise an effective heatflow - is manufactured by Würth Elektronik company [69] . This technology is listed by the brand name TWINflex®.

All "foot-prints" of dice on the substrate contain a copper-area, covered by a thin gold layer in the center. These areas are studded with so-called "thermal vias" (no electrical function), whose purpose is solely the conduction of dissipated heat to the copper-plate. All nine dice are placed and fixed using heat-conducting glue. A wire-bonding machine connects the pads on the dice to the pads on the substrate. After bonding is done, the "glob-top" coverage is applied to the vulnerable components on the MCM to protect them from environmental, mechanical and electrical damage. The MCM substrate is covered with a brass-lid; it is soldered onto a copper-frame in the top-layer and serves as a electro-magnetic shield against imposed noise from hostile surroundings. And finally a metal body made of studded metal (enlarged surface) is glued to the copper-plate to provide exchange of dissipated heat with the surrounding air-flow in the electronics crates [65].

Components such as capacitors and resistors are connected to the multi-layer structure using surface-mount technology (SMT). On either end a 60 pin SMD connector from SAMTEC (BTH030) connects the MCM to the Pre-Processor Module [67].

5.4 Large scale production

The MCM large scale production consists of two major stages: component dice production and assembly of the MCM. At the first stage all components produced have to be tested before being placed on the MCM substrate. This allows elimination of the faulty dice in the first production stage. At the second stage, the complete MCM-assembly is made in several steps with intermediate testing of the MCM functionality. This strategy allows to detect faulty components and assembly failures at early stages of the production, thereby improving the initial production yield.

5.4.1 Production cycle

As the MCM was fully designed and developed at KIP, the first few modules were produced at KIP. They were used for initial functional tests as was described in the previous chapter.

---

[1] An intermediate material which consists of a fabric preimpregnated with a resin.

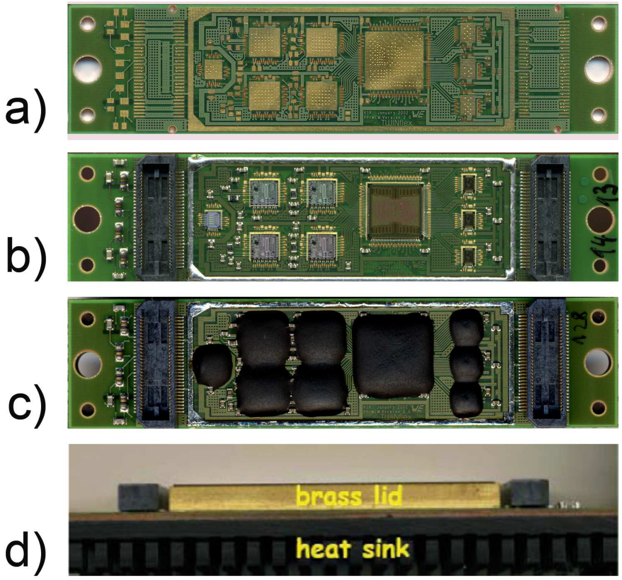

Figure 5.4: MCM assembly steps: a) MCM substrate; b) MCM with all dice bonded on substrate; c) MCM with glob-topped dice; d) MCM with brass and heat sink (side view)..

Such in-house MCM production helped to understand the production problems and to develop strategies for the large scale MCM production.

The rest of the MCM production was done by industry. The MCM substrates were produced by WÜRTH Elektronik, while mounting of dice and SMD components, wire-bonding, and encapsulation was done by HASEC[70]. Figure 5.4 shows the MCM assembly at different production steps. Those were:

- production of a 4-layer FR4 substrate backed by a 0.8mm copper plate,
- **electrical test of the routing-tracks**,
- **bonding test,**
- passive components soldering applying SMT technology,
- chip mounting,
- ultrasonic wire-bonding,
- **MCM Quality Assurance tests at KIP** ,
- application of glob-top over the 9 active chips,
- encapsulation of MCM hermetic brass lid; gluing of a heat sink for dissipated heat exchange,
- **MCM Quality Assurance tests at KIP**.

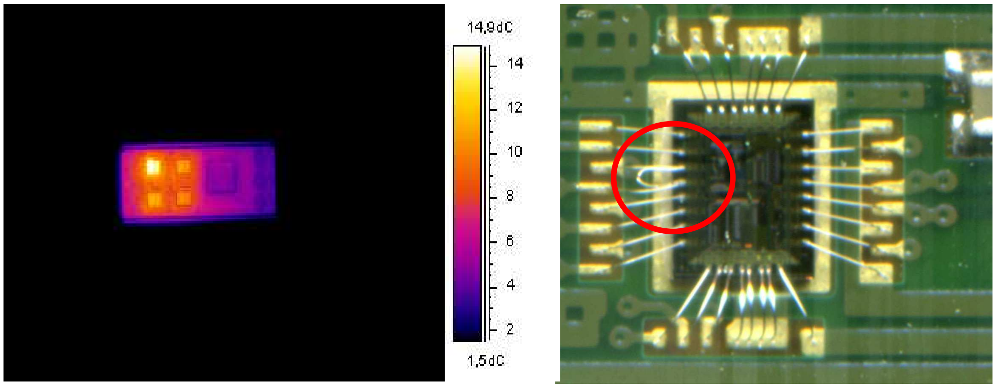

Figure 5.5: Investigations of faulty MCM with infrared camera (left) show the short-circuit in FADC.The bound fault (right) in serialiser chip is visible by microscope.

5.4.2 Repair procedure

The uncovered MCM failed the first quality assurance test undergo a detailed investigation. Different kinds of failures (short-circuits, faulty chips, bond faults etc.) make the investigation process rather complicated. In cases where the software alone is not sufficient to find the problem, an analysis using a microscope, an infrared camera and an oscilloscope is carried out. Figure 5.5 shows the examples of identified problems. On the left of Figure 5.5 the powered MCM is examined by infrared camera. A short-circuit in FADC causes the hot spot which is easily seen. On the right one can see the microscope picture of the bond fault. After further investigations all faulty MCMs for which nonworking chips could be determined, undergo a repair cycle at the mounting company.

5.5 Production results

At the time of writing the MCM production is fully accomplished. The number of functioning MCMs identified during production cycle is 3012; the number of MCMs, which were found faulty is 776. Currently more than 200 MCMs have been successfully repaired. All test results as well as supplementary information for each single MCM are stored in the database accessible via WWW.

Chapter 6

Performance tests of the fast shower simulation model

This chapter is devoted to the ATLAS fast simulation. It gives an overview of an improved version of fast simulation of the ATLAS calorimeter – the fast shower (FS) parametrisation package. The results of the validation tests of the fast simulation performance with shower parametrisation and comparison to a detailed full simulation based on inclusive jet production are presented.

6.1 The ATLAS offline simulation framework – Athena

Athena is ATLAS offline simulation framework based on the GAUDI [72] architecture originally developed by the LHCb collaboration. This architecture has been extended in ATLAS by including the ATLAS-specific enhancements. All the event processing tasks including simulation and reconstruction in ATLAS are carried out within Athena framework.

Figure 6.1 shows the simulation chain of an event implemented in Athena. The full detector simulation based on GEANT 4 performs a detailed simulation of particle interactions in detector medium, the digitisation stage simulates the detector readout electronics. The input to the reconstruction layer can be MC generated data or real data. The reconstruction layer implies a set of procedures which identify the physics objects (single particles, jets, E_T^{miss} etc.) and calculate their kinematic parameters (energies, momenta, etc.) based on the information provided by the real detector or detector simulation. Taking into account the non-compensating type of the ATLAS calorimetry, passive material, electronic noise and other instrumental effects, different calibration methods are implemented in software at reconstruction stage and finally applied to the identified physics objects, depending on the type of these objects.

The results of the data processing in Athena can be written in different formats for further user analysis. The main formats of data files are ESD and AOD:

- ESD - Event Summary Data. ESD contains the detailed output of reconstruction (calorimeter cells, towers tracking information, jet constituents, detailed MC truth information).

- AOD - Analysis Object Data. AOD can be produced based on ESD and contains refined reconstruction information like identified particles e, γ or reconstructed jets.

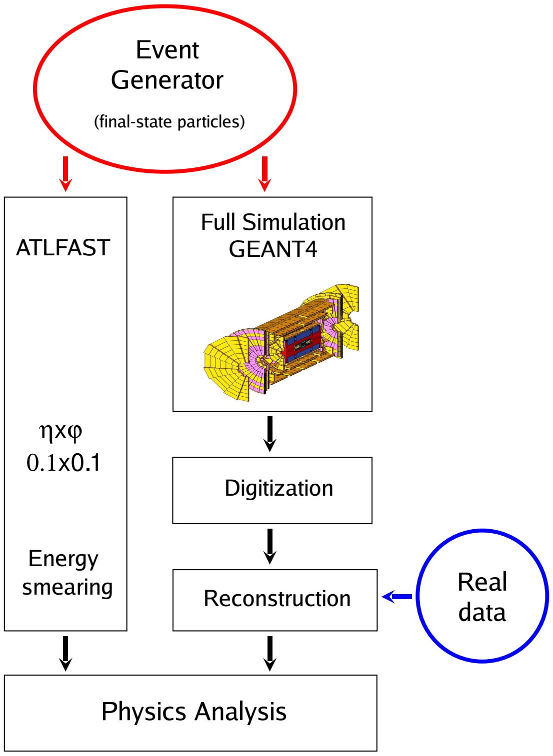

Figure 6.1: Simplified scheme of the simulation chain in the in Athena framework.

6.2 The ATLAS fast simulation package

ATLFAST performs a fast simulation of the ATLAS detector. It is an important tool for high-statistics studies, estimation of signal and background rates.

Based on simple detector geometry description with one layer, ATLFAST does not simulate the interactions of the incoming particle with the detector. The reconstruction layer is also skipped in the fast simulation. Instead, ATLFAST smears the true energy of the particle according to the resolution functions parametrised on the basis of the full simulation.

The main ATLFAST characteristics can be summarised as follows:

- **Input data:** stable particles from the event generator;
- **Calorimeter cell map:** granularity of $\Delta\eta \times \Delta\phi = 0.1 \times 0.1$ up to $|\eta| < 3.2$ and $\Delta\eta \times \Delta\phi = 0.2 \times 0.2$ for $3.2 < |\eta| < 5.0$.;
- **Calorimeter response** is set to one for all regions of the calorimeter map. No crack region simulation is implemented;
- **Solenoidal magnetic field:** 2T;
- **Output final state physical objects:** electrons, photons, muons, jets, taus, missing transverse momentum p_T^{miss};

A detailed description of the initial ATLFAST package and its improved version can be found in [73] and [74], respectively. A brief overview of the main ATLFAST processing steps is given below.

Stable particles are propagated through the magnetic field and contribute their energies to the calorimeter cells.

The cells with transverse energy higher than a threshold of 1.5 GeV act as seeds for cluster reconstruction. This cluster reconstruction is based on the cone algorithm with a cone size R=0.4. The sum of the transverse energies of the cells within the cone is the energy of the cluster. If the cluster energy exceeds a threshold of 5 GeV, the cluster is stored in a list of clusters for the current event. At the next stages the type of the reconstructed cluster is identified and the cluster is assigned to an electron, photon, muon, tau or jet.

For electrons generated in the event the reconstructed cluster is associated if its separation from the electron direction in $\eta \times \phi$ space is less than $\Delta R = 0.15$. Electrons are identified as isolated if the energy in a cone of size $\Delta R = 0.2$ around them is less than 10 GeV and no further clusters reconstructed within a cone radius of $\Delta R = 0.4$ around the electron direction. The energy of the identified electron is smeared according to the resolution functions. If the transverse energy of the electron is above the threshold of 5 GeV, then the electron is recorded and the associated cluster is removed from the cluster list. Similar reconstruction procedures are applied to photons.

In case of muons, the resolution function is applied to the true muon momentum. This function depends on the p_T, η and ϕ of the muon. The muons with smeared momentum higher than $p_T > 5$ GeV which pass the isolation criteria, similar to those of electrons, are stored; muons which do not pass the isolation criteria are marked as non-isolated and also stored.

Clusters which are not assigned to electrons or photons are associated to jets. The energy of these clusters summed up with the energy of the non-isolated muons forms the jet energy. Then the jet energy is smeared according to the resolution functions. Jets with energies exceeding a threshold of 10 GeV are recorded. Taus and b-jets are identified by applying τ- and b-tagging procedure. To identified taus and b-jets the tagging efficiencies obtained from full simulation are applied.

The missing transverse momentum p_T^{miss} is calculated by summing the transverse momenta of identified isolated photons, electrons, muons, taus, jets and non-isolated muons which are not added to any jet. Cells not associated to any cluster are added to the p_T^{miss} calculation as well.

Although the ATLFAST produces reasonable simulations, compared to the full simulation results, the simplified calorimeter model with one layer and Monte Carlo based approach set limits for more realistic detector simulation.

In order to overcome these and other deficiencies an improved calorimeter fast simulation has been developed, based on the parameterisations of showers.

6.3 A shower parametrisation model for ATLFAST

A model of electromagnetic and hadronic shower parametrisation [75] recently implemented in the ATLAS fast simulation framework ATLFAST describes the longitudinal and lateral shower profile. It also provides a more detailed description of the calorimeter geometry, including electromagnetic and hadronic layers, as well as crack regions. The new approach improves significantly the fast simulation of the ATLAS calorimeter.

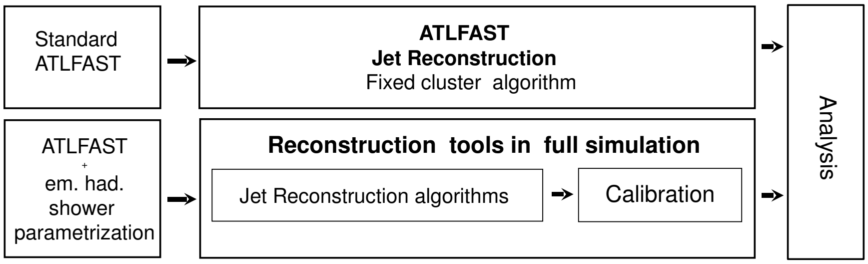

Figure 6.2: The block diagram of the jet reconstruction for improved fast simulation. The implementation of the shower parametrisation and double calorimeter map allows to use reconstruction algorithms from the full simulation.

The calorimeter response and resolution for single photons and charged pions has been extracted from the full detector simulation and parametrised as a function of energy and pseudorapidity. For both photons and charged pions the energy range from 200 MeV up to 200 GeV over the full pseudorapidity range $0 < |\eta| < 4.9$ has been covered. In addition the energy sharing between electromagnetic and hadronic calorimeter is parametrised for the given energy range. For the particles with energies higher than 200 GeV the sharing is done as for particles of 200 GeV, and response and resolution are determined by extrapolation of the obtained parametrisation functions.

Shower profiles have been parametrised based on the data generated at two pseudorapidities $|\eta|$=0.2 and $|\eta|$=2.0, in order to cover the barrel and end-cap regions, respectively. For electromagnetic and hadronic showers the parametrisation procedures are different. In case of electromagnetic showers, the distribution of the shower energy in the cell[1] matrix of 2×3 in $\eta \times \phi$ around the hit cell is parametrised. Taking into account the fact, that only a small energy fraction of the em. shower is deposited in the hadronic calorimeter, the total hadronic energy is deposited in a single cell of a hadronic layer behind the hit cell.

In case of hadronic showers, the distribution of the shower energy in a wider 4×5 calorimeter cell matrix is parametrised. The matrix is divided in 2×3 core region and surrounded by a ring of 14 cells which are considered as a halo of the hadronic shower. Different parametrisation procedures are applied for each region.

The parametrisation also distinguishes between two shower types, depending on the shower starting point: late showers which starting point is in the hadronic calorimeter and early showers initiated by the hadrons which undergo their first nuclear interaction in the em calorimeter. For the late showers the total energy deposited in the em calorimeter is put in the single hit cell and the hadronic energy in the 4×5 cell matrix, while for the early showers the em energy is deposited in the cell matrix in both em and hadronic layers.

6.3.1 Jet reconstruction

An important consequence of the implementation of the new calorimeter model with shower parametrisation in the fast simulation is the possibility to apply a wide range of reconstruction and calibration tools as in full simulation. The reconstruction chains in

---

[1] Each cell has a size of 0.1×0.1 in $\eta \times \phi$.

case of jets, for standard ATLFAST and ATLFAST in FS mode are shown in the block scheme in Figure 6.2. Instead of using the simple jet reconstruction procedure based on the fixed cluster algorithm in standard ATLFAST, a list of jet reconstruction algorithms implemented in **JetRec**[2] package can be applied. A simplified list of steps in the ATLAS jet reconstruction can be expressed as follows:

- Jet algorithms (cone, K_T etc.) are applied to jet constituents (calorimeter towers, topological clusters or particles) as described in Section 1.3.2.
- For reconstructed jets at the electromagnetic scale[3] one of the calibration procedures is applied.

The jet reconstruction and calibration procedures will be described in some detail in the next chapter, here it should be mentioned that the "H1-style" calibration is used by default. Applying this calibration the jet energies are calibrated to the hadronic scale[4].

A parametrisation of the response at the em scale includes the effect of non-compesation of the ATLAS calorimeter, presence of dead material and crack regions in fast simulation. Thus, a more realistic calorimeter description requires the application of the calorimeter calibration procedure as well. A full jet reconstruction chain including the calibration procedure has been attached to the fast simulation in the FS mode as shown in Figure 6.2. The details of the implementation can be found in [76].

The studies of the fast simulation performance for jets carried out in order to show that the implemented new model together with reconstruction and calibration layer provides a more realistic fast description of the ATLAS calorimeter will be described in the rest of this chapter.

6.4 Fast Shower model validation using di-jet events

6.4.1 Data sample preparation

The production cross-sections of high p_T jets in QCD events are several orders of magnitude smaller than cross-sections for low p_T jets. Thus, to provide enough statistics for QCD events in any jet p_T range, their generation is done in eight p_T regions. These p_T regions cover the whole jet p_T range expected at LHC. Each region is defined at generator level by setting kinematic cuts for the hard scattering process. These cuts set the bounds for p_T values of the produced jets. However the p_T distribution of the produced jets is not restricted by the kinematic region defined by the cuts. The processes like ISR, FSR, fragmentation and underlying event smear the p_T boundaries of the produced jets. The kinematic cuts for eight p_T regions, corresponding dataset names and the jet production cross-sections are given in Table 6.1.

The jet datasets J1, J2, J4, J5, J7 fully simulated with Athena version 10.0.1 have been used for validation of the improved fast simulation. Each dataset contains 10000 events. The choice of this Athena version is explained by the fact that data simulated with it were used for parametrisation of the showers for fast simulation.

The reconstruction of the datasets for validation has been done using Athena 11.0.42 with the fast simulation in FS mode on. Thus, finally the produced n-tuples contain the

---

[2] JetRec is a package in Athena software, which is used for jet reconstruction in fully simulated events.

[3] An electromagnetic scale is discussed in some detail in the Section 7.1.1.

[4] The scale which is achieved after corrections for non-compensation of the calorimeter is referred to as hadronic.

output from the fast and full simulation for the given event as well as particle level data. An event-by-event comparison is done between the fast and the full simulation based on these n-tuples.

Table 6.1: QCD di-jet samples and their cross-sections in the ATLAS official production.

Dataset	p_T **Range,GeV**	σ, **cross-section, mb**
J1 Di-jet	17-35	1.39
J2 Di-jet	35-70	9.64^{-02}
J3 Di-jet	70-140	6.15^{-03}
J4 Di-jet	140-280	3.16^{-04}
J5 Di-jet	280-560	1.24^{-05}
J6 Di-jet	560-1120	3.44^{-07}
J7 Di-jet	1120-2240	5.29^{-09}
J8 Di-jet	>2240	2.21^{-11}

6.4.2 Validation results

Jet matching

Most of the jet performance and calibration studies require the comparison of the jet reconstructed after detector simulation to the same particle jet[5]. The particle jet is associated to the reconstructed jet after simulation if the angular distance ΔR_{match} between them is less than a matching cut which is typically 0.2:

$$\Delta R_{match} = \sqrt{(\eta_{Rec} - \eta_{Truth})^2 - (\phi_{Rec} - \phi_{Truth})^2} < 0.2, \tag{6.1}$$

where (η_{Rec}, ϕ_{Rec}) are the coordinates of the jet reconstructed after detector simulation and $(\eta_{Truth}, \phi_{Truth})$ are the coordinates of the jet at particle level.

An example of the distribution of ΔR_{match} between jets from fast simulation in FS mode and particle jets within $0 < |\eta| < 0.7$ in two E_T bins is shown in Figure 6.3a). One can see that ΔR_{match} is minimal for jets higher than 100 GeV and much less than 0.2, while for the jets with E_T lower than 100 GeV the distribution of ΔR_{match} is much broader. At these energies the jets are not so collimated, and many effects (out-of-cone, magnetic field, energy resolution etc.) which are suppressed at high energies start to play a significant role in the jet reconstruction, degrading its accuracy. The low energy range is the most difficult range for simulation and calibration. Similar distributions are observed also for fully simulated jets.

In Figure 6.3b) the distributions of $\Delta R'_{match}$ defined similar to eq. (6.1) between jets simulated with standard ATLFAST as well as with fast simulation in FS mode and fully simulated jets are shown. The difference in the ΔR_{match} distributions shows that the jets produced with the improved fast simulation are closer to the fully simulated jets.

---

[5] A particle jet is a jet reconstructed by applying the jet algorithm at generator level to stable particles before detector simulation.

In Table 6.2 the fractions of matched jets within ΔR_{match}=0.2 in several E_T bins are shown. The upper two rows show the fractions for FS and fully simulated jets to particle jets. One can conclude that FS jets are closer to the particle jets in the low energy ranges, as the fraction of jets contained within $\Delta R_{match} = 0.2$ is higher for FS than for full simulation.

The lower part of Table 6.2 shows the same fractions but for FS and standard ATLFAST vs. full simulation. The increased fraction of the FS jets which are within $\Delta R_{match} = 0.2$ in all E_T bins, compared to the standard ATLFAST, is clearly visible.

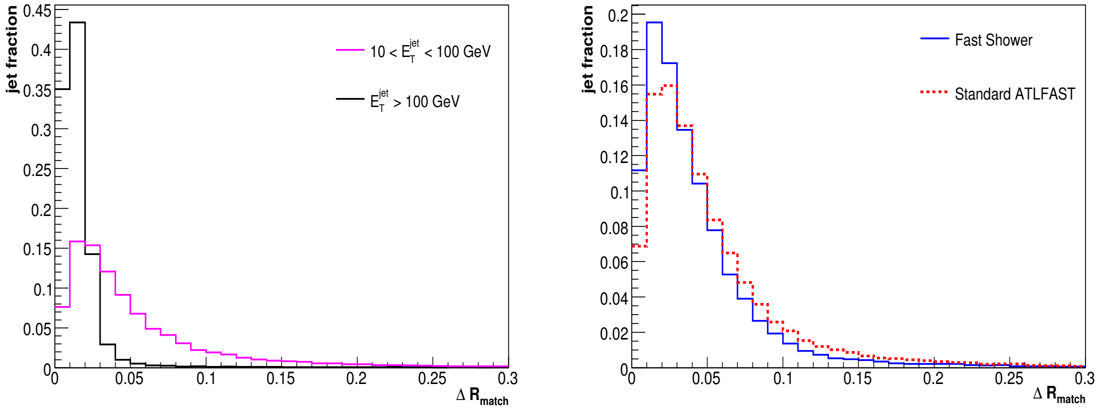

a) b)

Figure 6.3: Matching radius ΔR_{match}: a) ΔR_{match} between fast simulated jets and particle jets for E_T <100 GeV (pink) and $E_T > 100$ GeV (black); b) ΔR_{match} between fast simulated jets and full simulated jets with E_T <100 GeV for standard ATLFAST (dashed) and ATLFAST in FS mode (solid) within $|\eta| < .7$.

Table 6.2: Fractions of the jets matched in $\Delta R_{match} = 0.2$.

Fraction of jets matched in $\Delta R_{match} = 0.2$ in E_T bins (GeV)	E_T <20	20< E_T <50	50< E_T <100	E_T >100
Fast Shower vs. MC Truth	79%	96%	97%	99%
Full sim. vs. MC Truth	72%	93%	96%	98%
Fast Shower vs. full sim.	71%	96%	97%	99%
St. ATLFAST vs. full sim.	65%	86%	88%	98%

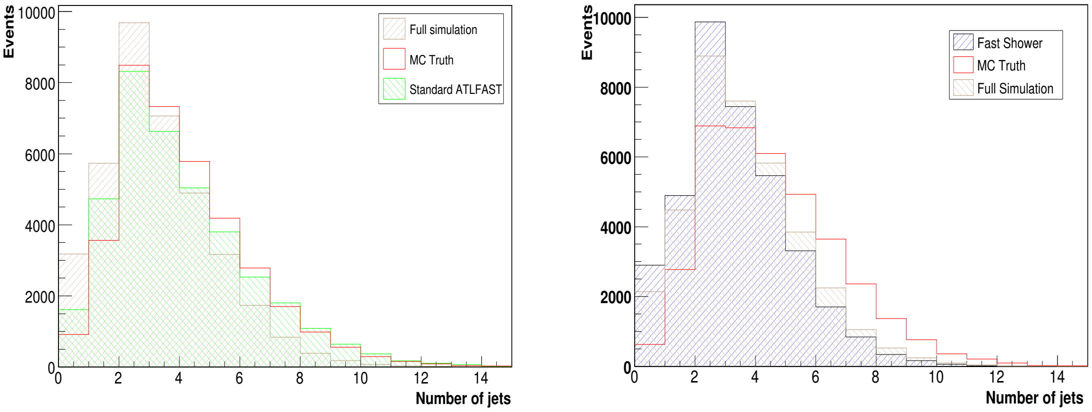

a) b)

Figure 6.4: Jet multiplicity comparison for jets with a cone R=0.4 in the η range of $0 < |\eta| < 4.9$: a) standard ATLFAST, full simulation, and particle jet multiplicities; b) fast simulation in FS mode, full simulation, and particle jets multiplicities.

Jet multiplicities

The comparison of multiplicities for standard ATLFAST jets, fully simulated jets and particle jets for jet cone R=0.4 is shown in Figure 6.4a). The multiplicity distribution of the standard ATLFAST jets is more similar to the multiplicity distribution of the jets at particle level, especially in the tail which contains the events with a high number of low energetic jets. This shows that the standard ATLFAST is much more dependent on the MC truth level. The jet multiplicity distribution for the FS jets look quite different as is shown in Figure 6.4b). It is closer now to the fully simulated jet multiplicity, rather than

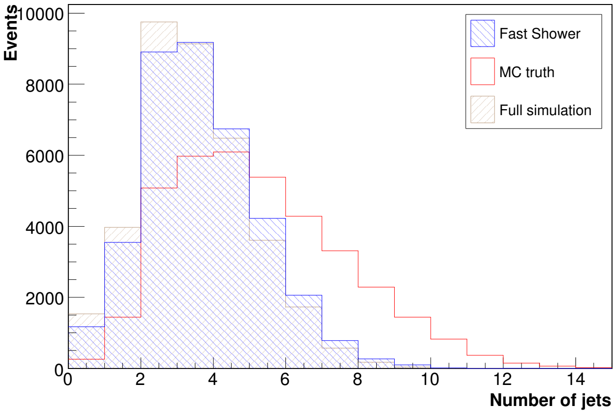

Figure 6.5: Multiplicities for Fast Shower, full simulation and MC Truth jets with a cone size 0.7.

to the multiplicity of the particle jets. Figure 6.5 shows the similarities in the multiplicities for jets with a cone radius R=0.7.

Jet energy response and resolution

The calorimeter response (see Section 2.2.2) is the main subject of almost all calorimeter performance studies. The linearity of the response in the full calorimeter acceptance and in the wide energy range is an important requirement for a good calorimeter. The initial response of the ATLAS calorimeter is far away from the linear especially for jets, which can be explained by the non-compensating nature of the calorimeter, presence of the crack regions, dead material and the complicated jet structure.

A detailed comparison of the response to jets in the improved fast simulation and the full simulation has been done in different η and energy bins. The size of the energy bins is not fixed for the whole examined energy range. It has been chosen so, that the statistics of the di-jet events in all the bins is kept at an equal level.

For each energy bin defined by the jet energy at particle level the distribution of the ratio between the energy of the reconstructed FS jet E^{Rec} and particle jet E^{Truth} is fitted by a Gaussian distribution. The same comparison procedure has been also repeated for the transverse energy. The distributions have been fitted with Gaussian in a range of $\pm 2\sigma$ around the peak. An example of such fitted distribution at the em and at the hadronic scale is shown in Figure 6.6. The mean values of these distributions are plotted versus the E^{Truth} (E_T^{Truth}) of the particle jet and will be shown in comparison studies in the next sections.

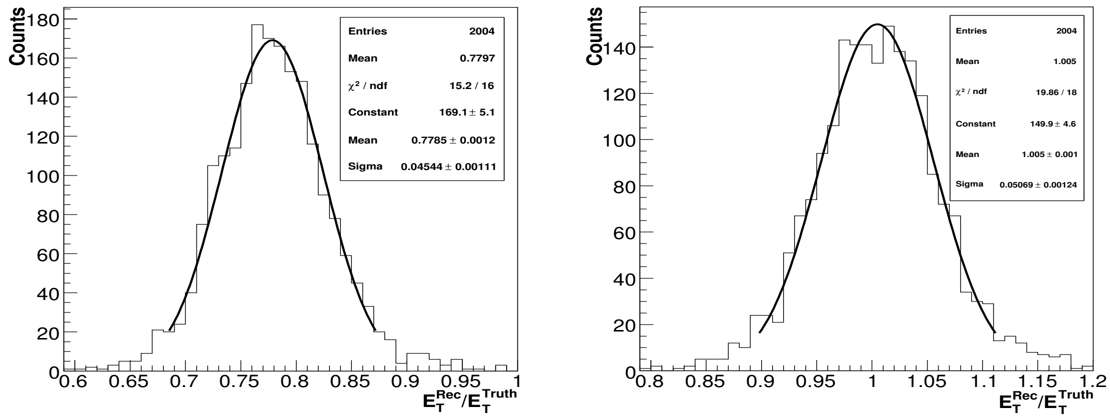

a) b)

Figure 6.6: The distributions of the ratio between transverse energy of the reconstructed jet E_T^{Rec} and particle jet E_T^{Truth}: a) Electromagnetic scale; b) Calibrated hadronic scale.

Electromagnetic scale

Response

The linearity in terms of ratios between the transverse energy of the reconstructed jet and particle jet as a function of transverse particle jet energy for standard ATLFAST and full simulation for jet cone R=0.4 are shown in Figure 6.7. The deviation from linearity is significant for ATLFAST especially at low energies, where the accuracy of the jet reconstruction is affected by significant out-of-cone effects caused by the magnetic field and presence of the ISR/FSR. The effects of initial and final state radiation are resolved to some extent by the split-and-merge procedure (see Section 1.3.2) which is missing in the ATLFAST reconstruction procedure.

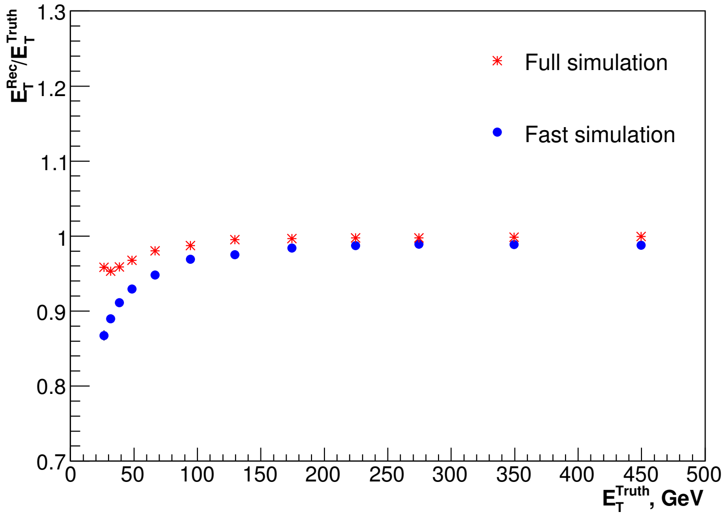

Figure 6.7: The ratios between transverse energy of the reconstructed jet and particle jet as a function of transverse particle jet energy for standard ATLFAST (blue) and full simulation (red) in $|\eta| < 0.7$.

The comparison of the distributions of the ratio between transverse energy of the reconstructed jet E_T^{Rec} and particle jet E_T^{Truth} for fast simulation in FS mode (blue) and full simulation (red) with default reconstruction algorithm in fast simulation and with applying jet reconstruction implemented in full simulation framework in the central η range are shown in Figure 6.8. The non-linear ATLAS calorimetry response at the em scale is clearly visible on these plots. In addition one still sees the deviations of the fast simulation distribution from full simulation results without applying the full jet reconstruction in Figure 6.8a). Figure 6.8b) shows that deviations become minimal after applying the same reconstruction scheme as done in full simulation.

The same distributions are shown at the em scale for different η ranges in Figure 6.9. The deviations are visible in the $2.5 < |\eta| < 3.5$ range which partly covers the endcap and forward regions. According to the [75] a detailed shower parametrisation has been done for $\eta = 0.2$ and $\eta = 2.0$, thus it could be that shower profiles for the higher η values are not described properly with the limitation of a cell granularity 0.1×0.1 by the current parametrisation, taking into account different calorimeter types and coarser granularity in the forward region as well as a significant amount of dead material in the transition region

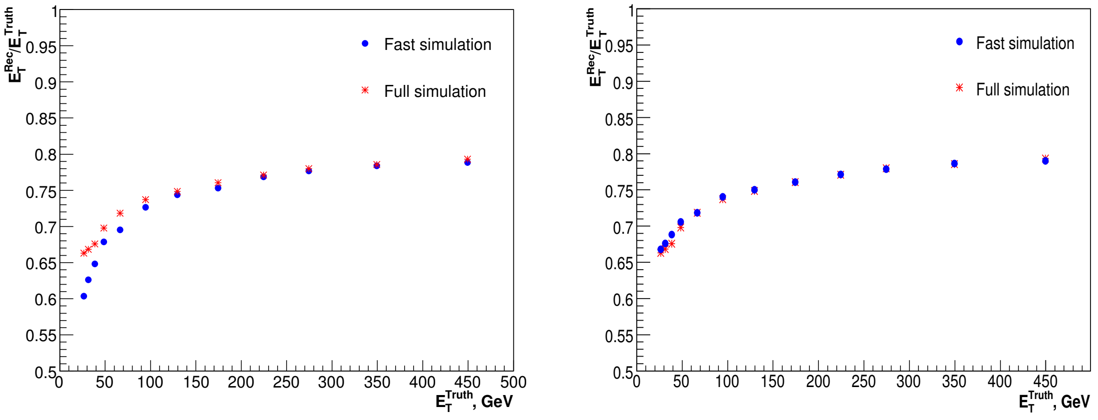

a) b)

Figure 6.8: The distributions of the ratio between transverse energy of the reconstructed jet E_T^{Rec} and particle jet E_T^{Truth} for Fast Shower (blue) and full simulation (red): a) with standard jet reconstruction in fast simulation; b) With jet reconstruction from full simulation applied to the fast jets.

between endcap and forward regions.

The ratios between transverse energy of the reconstructed jet and particle jet with a cone size $\Delta R = 0.7$ as a function of transverse energy of particle jets for fast simulation in FS mode and full simulation at em scale for different η ranges are shown in Figure 6.10. While for the central region the deviations between fast and full simulations are minimal, they become significant and larger than for jets with a cone $\Delta R = 0.4$ in the endcap and forward regions. The different behaviour for different cone sizes suggests that the jet profile is not perfectly described in the FS model.

In Figure 6.11 the same ratios for cone sizes R=0.4 and R=0.7 are drawn versus pseudorapidity for jet transverse energies in the energy range of 80–120 GeV. The non-linear calorimeter response as well as the main transition regions at η=1.5 and at η=3.2, where a significant amount of the dead material degrades the response, are clearly seen. While for cone radius R=0.4 rather good similarity between fast and full simulation is observed, a 2-3% discrepancy is visible for a cone radius R=0.7.

The ratios between energy of the reconstructed jet and particle jet with a cone size $\Delta R = 0.4$ and $\Delta R = 0.7$ as a function of particle energy for fast simulation in FS mode and full simulation at em scale for different η ranges are shown in Figures 6.12 and 6.13 respectively.

Resolution

The energy resolution is the one of the most important calorimeter parameters which defines the precision of the energy measurement for a given particle type. The absolute energy resolution is defined as a width of the distribution of the energies measured in the calorimeter for a given particle. Most of the fluctuations of the energy measurements in

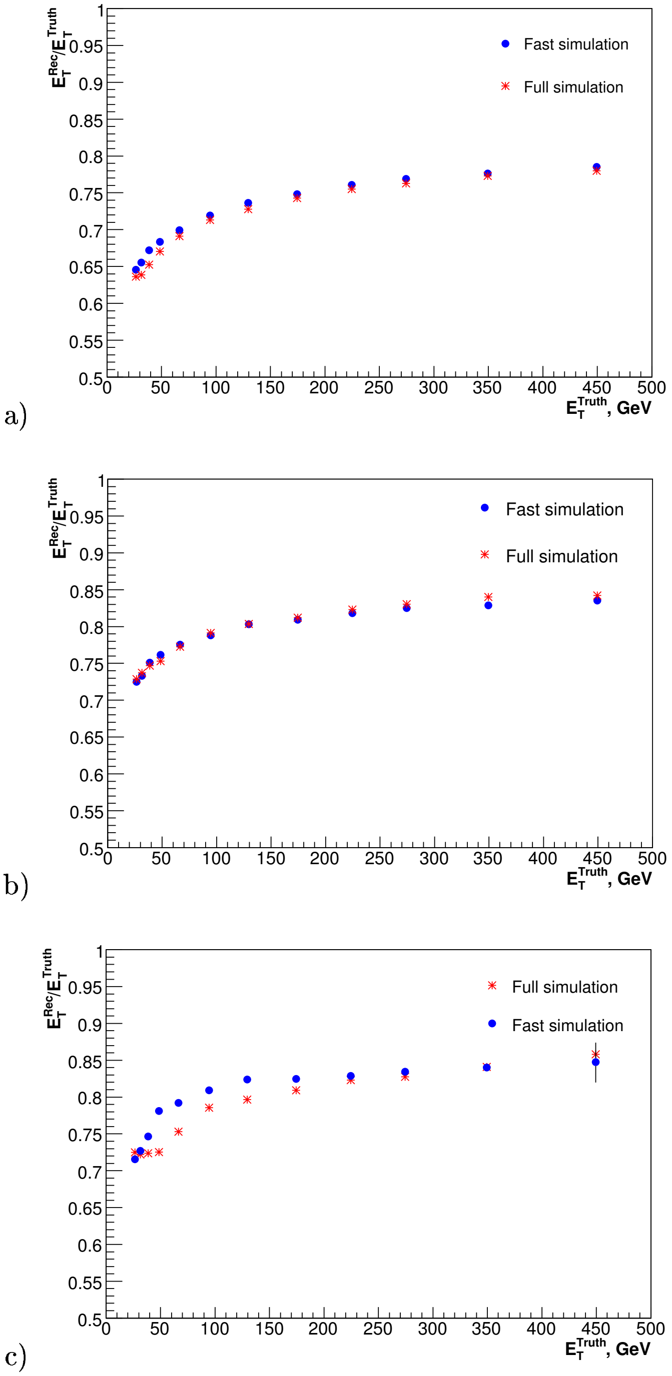

Figure 6.9: The ratios between transverse energy of the reconstructed jet and particle jet with a cone size $\Delta R = 0.4$ as a function of transverse energy of the particle jet for fast simulation in FS mode (blue) and full simulation (red) at the em scale for different η ranges: a) $0.7 < |\eta| < 1.5$; b) $1.5 < |\eta| < 2.5$; c) $2.5 < |\eta| < 3.5$.

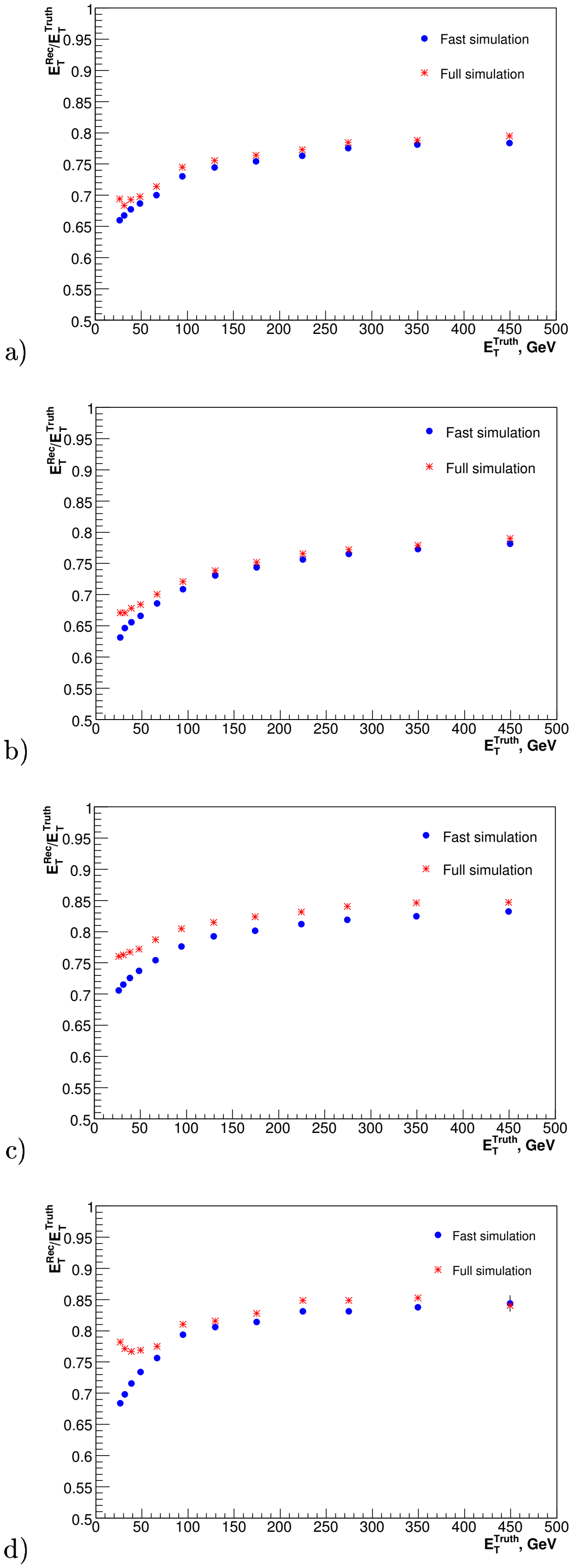

Figure 6.10: The ratios between transverse energy of the reconstructed jet and particle jet with a cone size $\Delta R = 0.7$ as a function of transverse energy of the particle jet for fast simulation in FS mode (blue) and full simulation (red) at the em scale for different η ranges: a) $0 < |\eta| < 0.7$; b) $0.7 < |\eta| < 1.5$; c) $1.5 < |\eta| < 2.5$; d) $2.5 < |\eta| < 3.5$.

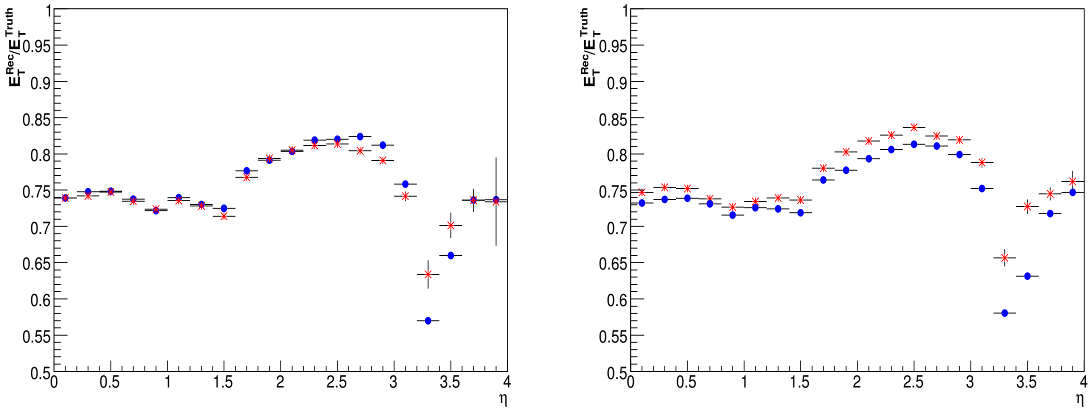

a) b)

Figure 6.11: The ratios between transverse energy of the reconstructed jet and particle jet as a function of pseudorapidity for fast simulation in FS mode (blue) and full simulation (red): a) Jets with a cone size R=0.4; b) Jets with a cone size R=0.7.

calorimeter come from the fluctuating number of the particles associated with the signal. These fluctuations are ruled by the Poisson statistics. Thus, the relative resolution based on these fluctuations can be defined as:

$$\frac{\sigma}{E} = \frac{a}{\sqrt{E}}, \tag{6.2}$$

where E is the incoming particle energy, σ is an absolute energy resolution, a is a parameter of the sampling term. Other fluctuation sources which significantly affect the energy resolution can be expressed by additional terms and added to the relative energy resolution expression eq.(6.2) quadratically as they are statistically not correlated. With these additional terms the resolution expression in eq.(6.2) can be rewritten as follows:

$$\frac{\sigma}{E} = \sqrt{\frac{a^2}{E} + b^2 + \frac{c^2}{E^2}} \tag{6.3}$$

The additional fluctuation sources are expressed by the following terms:

- **Constant term b** which includes the fluctuations which are basically associated with the instrumental effects like calorimeter imperfections, non-compensation, calibration errors etc. Typically the constant term dominates the calorimeter energy resolution at high energies.

- **Noise term** c/E represents the electronic noise contribution to the resolution.

The expression 6.3 will be used to parametrise the jet energy resolution as a function of jet energy in the studies presented in this chapter. The jet energy resolution for a given energy bin used in the comparison studies is defined as σ of a Gaussian fit of the distribution of E^{rec}/E^{Truth} normalised by the mean value of the fit, where E^{rec} is the

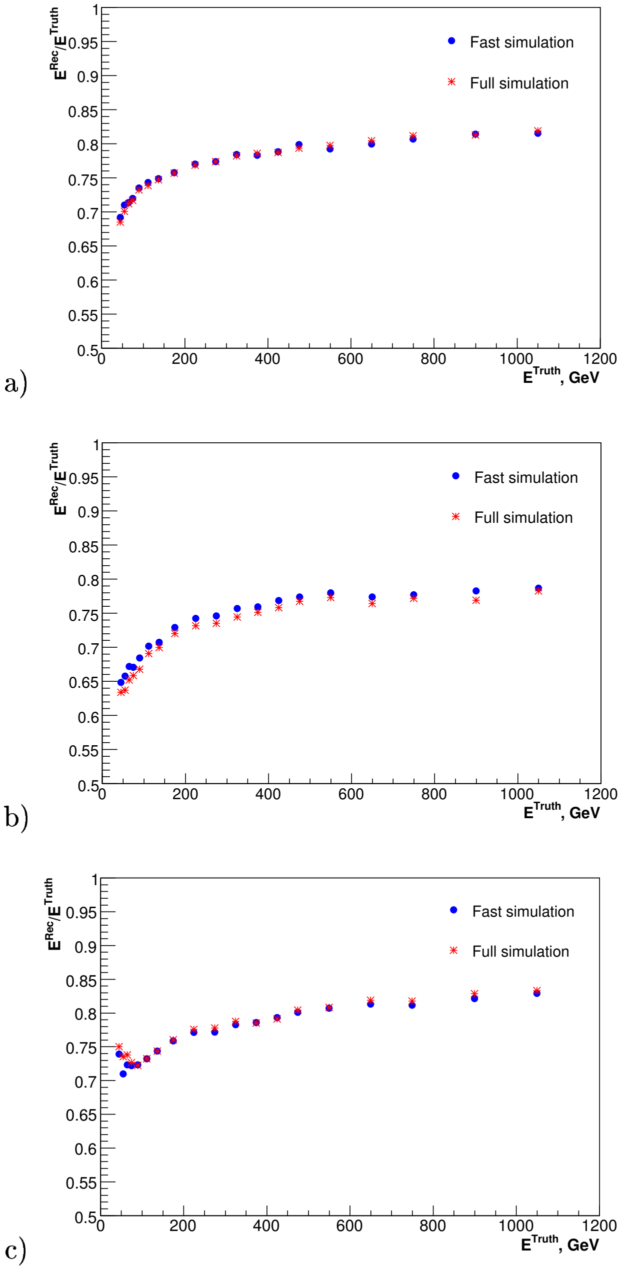

Figure 6.12: The ratios between energy of the reconstructed jet and particle jet with a cone size $\Delta R = 0.4$ as a function of energy of the particle jet for fast simulation in FS mode (blue) and full simulation (red) at the em scale for different η ranges: a) $0 < |\eta| < 0.7$; b) $0.7 < |\eta| < 1.5$; c) $1.5 < |\eta| < 2.5$.

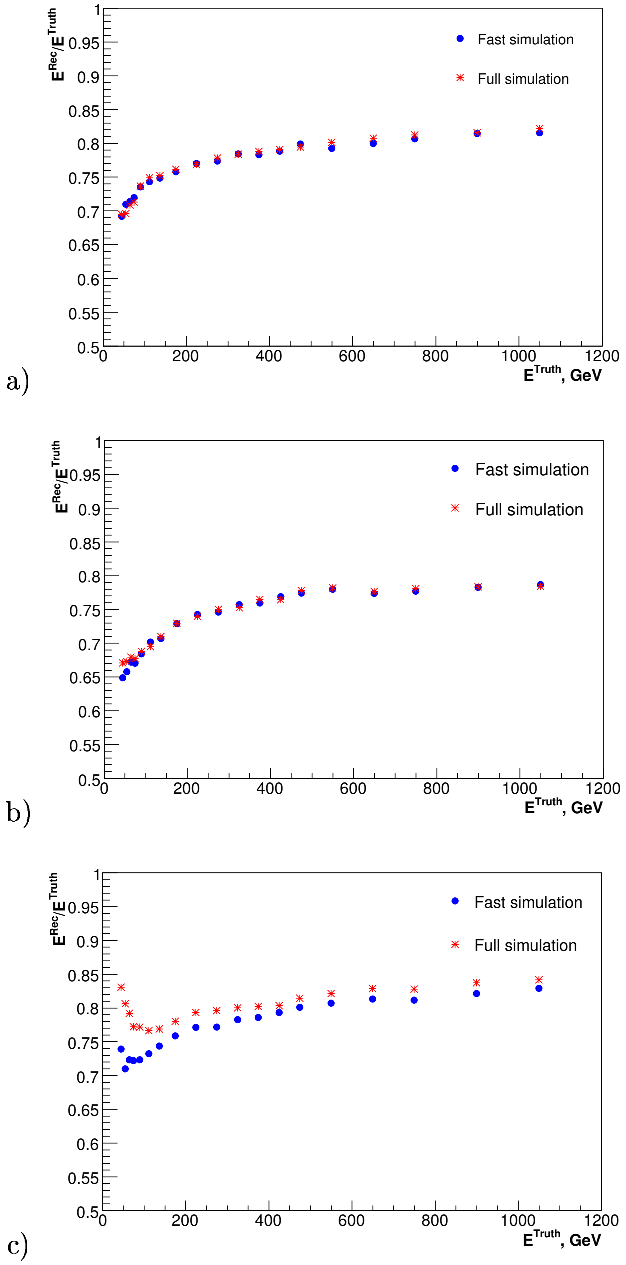

Figure 6.13: The ratios between energy of the reconstructed jet and energy of the particle jet with a cone size R=0.7 as a function of energy of the particle jet for fast simulation (blue) and full simulation (red) at the em scale for different η ranges: a) $0 < |\eta| < 0.7$; b) $0.7 < |\eta| < 1.5$; c) $1.5 < |\eta| < 2.5$.

reconstructed jet energy after simulation, and E^{Truth} is the energy of the jet at particle level.

Figure 6.14 shows the jet resolution plotted as a function of the particle jet energy in the central and endcap regions for fast and fully simulated jets with a cone size R=0.4. The resolutions for cone size R=0.7 are shown in Figure 6.15.

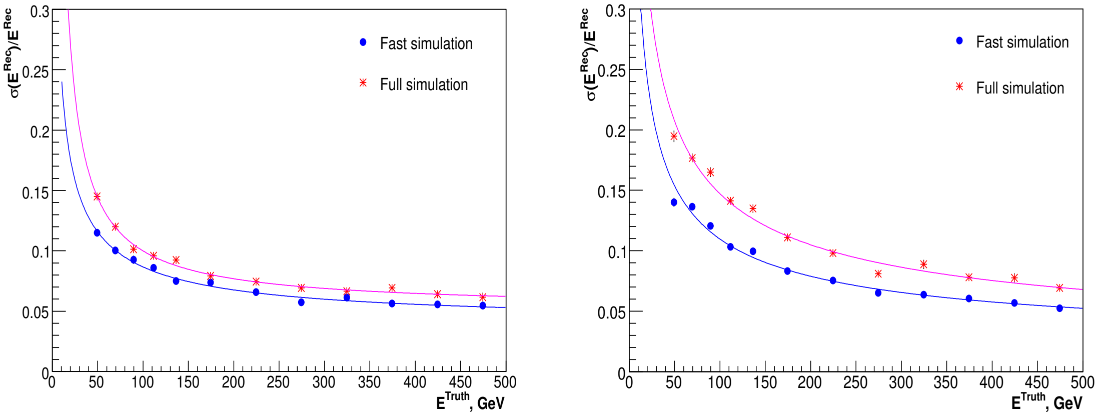

a)

b)

Figure 6.14: The jet energy resolution $\sigma(\mathrm{E}^{Rec})/\mathrm{E}^{Rec}$ as a function of the particle jet energy E^{Truth} for jets with a cone size R=0.4 in different η ranges: a) $0 < |\eta| < 0.7$; b) $1.5 < |\eta| < 2.5$.

The resolution predicted by the fast simulation in the central region is a few percent better than that one for full simulation. The deviations become essential in the endcap region for both cone types. One explanation of these deviations is that fully simulated samples used for the parametrisation do not contain electronic noise which is present in the fully simulated samples used for comparison.

The coefficients of the sampling, constant and noise terms of the fitting functions for energy resolutions shown in Figures 6.14 and 6.15 are given in Tables 6.3 and 6.4, respectively. The main differences are observed in the coefficients of the sampling terms and constant terms in end-cap region.

Table 6.3: Coefficients of the sampling, constant and noise terms for jet energy resolution in fast and full simulation. Jet with a cone size R=0.4.

η range	$0 < \|\eta\| < 0.7$			$1.5 < \|\eta\| < 2.5$		
Terms	**a, %$\sqrt{GeV}$**	**b, %**	**c, GeV**	**a,%$\sqrt{GeV}$**	**b, %**	**c, GeV**
Fast simulation	72.4	4.3	-	102.2	3.3	-
Full simulation	76.2	5.6	4.1	146.3	1.8	1.3

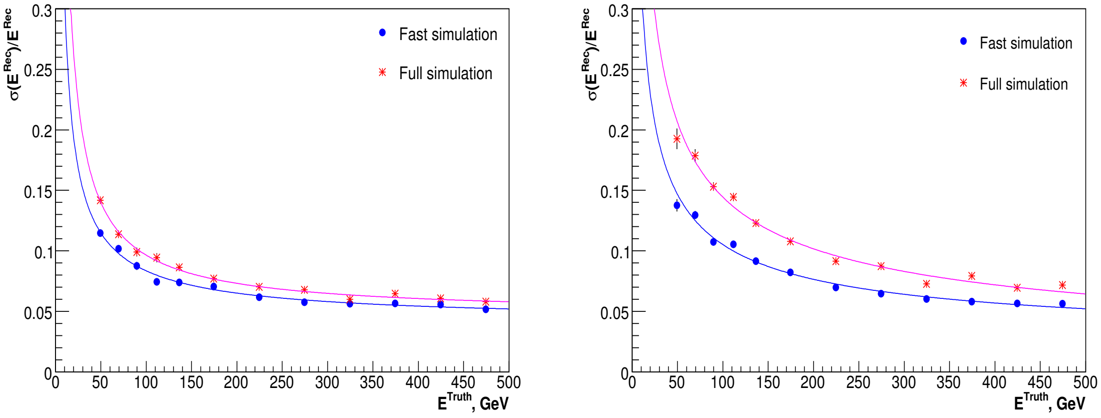

a) b)

Figure 6.15: The jet energy resolution $\sigma(\mathrm{E}^{Rec})/\mathrm{E}^{Rec}$ as a function of the particle jet energy E^{Truth} for jets with a cone size R=0.7 in different η ranges: a) $0 < |\eta| < 0.7$; b) $1.5 < |\eta| < 2.5$.

Table 6.4: Coefficients of the sampling, constant and noise terms for jet energy resolution in fast and full simulation. Jet with a cone size R=0.7.

η range	$0 < \|\eta\| < 0.7$			$1.5 < \|\eta\| < 2.5$		
Terms	**a, %$\sqrt{GeV}$**	**b, %**	**c, GeV**	**a,%$\sqrt{GeV}$**	**b, %**	**c, GeV**
Fast simulation	69.2	4.1	-	102.5	2.5	-
Full simulation	74.5	4.6	3.9	141.7	2.7	2.1

Similar comparison of the resolutions for transverse energies for jets with a cone size R=0.4 and R=0.7 is shown in Figures 6.16 and 6.17, respectively. One can see that the resolutions of transverse jet energies behave similarly to the the energy resolutions shown in the previous figures.

Hadronic scale

The linearity of the ratio of the reconstructed transverse jet energy after the “H1-style” calibration and transverse energy of the particle jet as a function of particle transverse jet energy for fast simulation in FS mode and full simulation is shown in Figure 6.18. The linearity is shown only for the central region in $0 < |\eta| < 0.7$. One can see that the “H1-style” calibration applied to the data at the em scale in the fast simulation corrects the response to the hadronic scale. The deviations from linearity do not exceed 2% up 100 GeV.

The jet energy resolutions after calibration in the central region for jet cones R=0.4 and R=0.7 are shown in Figure 6.19. The applied calibration significantly improves the energy

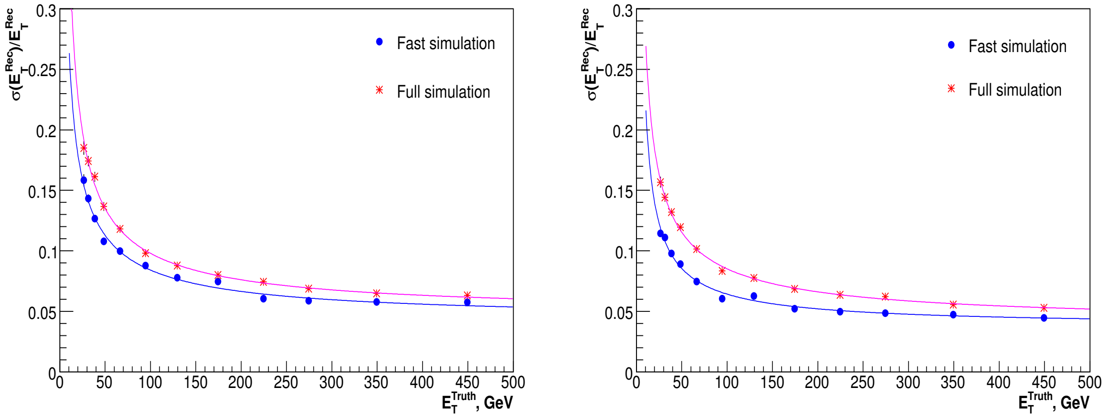

a) b)

Figure 6.16: The jet transverse energy resolution $\sigma(\mathrm{E}_T^{Rec})/\mathrm{E}_T^{Rec}$ as a function of the particle jet energy E_T^{Truth} for jets with a cone size R=0.4 in different η ranges: a) $0 < |\eta| < 0.7$; b) $1.5 < |\eta| < 2.5$.

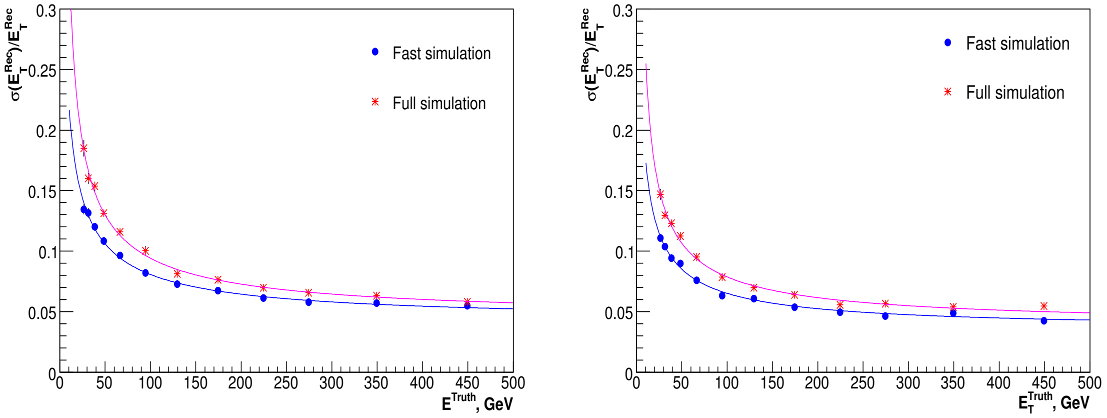

a) b)

Figure 6.17: The jet transverse energy resolution $\sigma(\mathrm{E}_T^{Rec})/\mathrm{E}_T^{Rec}$ as a function of the particle jet energy E^{Truth} for jets with a cone size R=0.7 in different η ranges: a) $0 < |\eta| < 0.7$; b) $1.5 < |\eta| < 2.5$.

resolutions for both fast and full simulations as expected. The summary of coefficients obtained by fitting the resolution distributions shown in Figure 6.19 are given in Table 6.5. The deviations in resolution are still essential. The resolutions in fast simulation are still better for the energies below ~ 200 GeV, compared to the full simulation, but getting

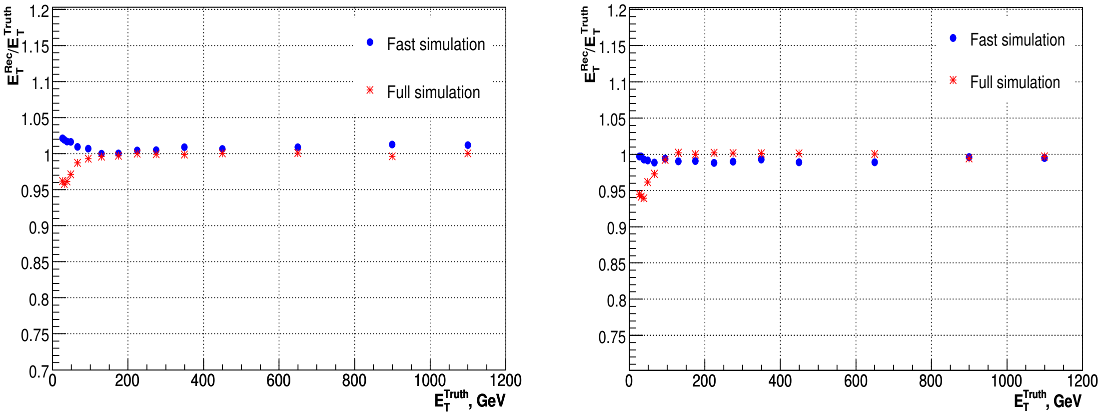

a) b)

Figure 6.18: The linearity of the reconstructed transverse jet energy and particle transverse jet energy as a function of particle transverse jet energy for fast and full simulations. The reconstructed jet is calibrated using "H1-style" calibration: a) For jets with a cone size R=0.4; b) For jets with a cone size R=0.7.

worse in the higher energy range which was not the case for the fast resolutions at the em scale shown in *e.g.* Figure 6.14. This behaviour may be explained by the contributions coming from calibration procedure. The calibration factors *i.e.* weights used to calibrate the jet energy are cell-based. At high energy a jet is more collimated and is "not resolved" in fast simulation, taking into account coarser granularity 0.1 × 0.1 in $\eta \times \phi$. Thus, the same weight is applied allover the jet. This leads to the observed deterioration in energy resolution for the jets in fast simulation.

Table 6.5: Coefficients of the sampling,constant and noise terms for calibrated jet energy resolution in fast and full simulation.

Terms	**a, %$\sqrt{GeV}$**	**b, %**	**c, GeV**	**a,%$\sqrt{GeV}$**	**b, %**	**c, GeV**
Fast simulation	65.6	3.2	0	59.1	3.3	0
Full simulation	63.2	2.4	4.2	55.7	2.4	3.1

6.5 Conclusions

The implementation of the fast shower parametrisation package in the fast simulation has provided a more realistic calorimeter description in the fast simulation. The analysis based on QCD jet events has shown a good agreement between fast and full simulation at the em scale for the calorimeter response, however the deviations have been observed in resolution. These deviations are most pronounced in the endcap and forward regions.

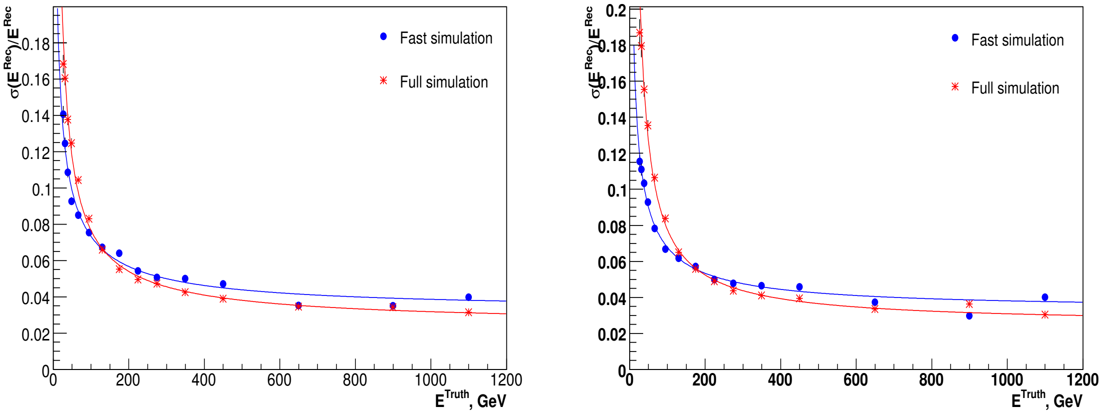

a) b)

Figure 6.19: The jet energy resolution $\sigma(\mathrm{E}^{Rec})/\mathrm{E}^{Rec}$ as a function of the particle jet energy E^{Truth} for fast and full simulation: a) for jets with a cone size R=0.4; b) for jets with a cone size R=0.7.

The calibration procedure applied to fast simulated data at the em scale provides a linear response at hadronic scale in the examined energy range (10 – 1200 GeV). Again, the main deviations at hadronic scale have been observed in the jet energy resolutions between fast and full simulation.

It has to be mentioned that the Fast Shower model does include only electromagnetic and hadronic layers and doesn't simulate in detail the longitudinal layer structure of the electromagnetic and hadronic calorimeters. In addition the granularity of the lateral cell size of 0.1×0.1 in $\eta \times \phi$ puts limitations for the detailed lateral energy simulation. Taking into account the limitations of the FS model it has to be mentioned that it provides reasonable realistic calorimeter description including calorimeter imperfections and crack regions. The presence of electromagnetic and hadronic layers together with coarse granularity which is identical to the granularity of the Level-1 Calorimeter trigger allows one to use it in trigger performance studies. The fast simulation in FS mode can also be used in high-statistics studies given the fact, that time required to process *e.g.* one dijet event including reconstruction in fast simulation in FS model is 0.4 s, while the full simulation needs for this about 15-20 min.

The FS model described in this chapter was the first step in the improvement of fast simulation with respect to the full simulation. Currently much more sophisticated calorimeter model in fast simulation which includes the multi-layer structure of electromagnetic and hadronic calorimeters is under intensive study [77].

Chapter 7

Calorimeter intercalibration using QCD jets

The accuracy for most of the measurements planned in the ATLAS experiment at LHC depends on the correct jet energy scale. This scale is affected on one hand by instrumental imperfections of the calorimeter system, and on the other hand by physics effects of *pp* scattering. Various *in situ* calibration methods will be used to check and correct for these effects. The calorimeter calibration procedure using dijet events is discussed in this chapter. The results of performance tests of this method, based on full GEANT4 simulations, are presented.

7.1 Jet reconstruction and calibration in ATLAS

A challenging task in any jet measurement is the determination of the absolute Jet Energy Scale (JES). The goal of many studies in ATLAS is to reach $\sim 1\%$ precision of JES. The systematic effects which contribute to the uncertainty of the JES are different, depending on the level of consideration. These levels (calorimeter level, particle level, parton level (see Section 1.3.2)) are depicted in Figure 7.1 which shows the evolution of the partonic system from hard scattering up to hadrons, whose energies can be measured in the calorimeter. The aim of the calibration procedure is to apply corrections for the jet energy in the calorimeter in order to recover the correct JES at particle level and finally at parton level. The effects which contribute to the uncertainty of the JES can be divided into two main categories:

- **Instrumental effects at calorimeter level.** These include initial scale, detector response non-linearity, non-compensation of the calorimeter, presence of dead material and cracks, longitudinal and lateral shower leakage, electronic and pile-up noise.
- **Physics effects at particle level.** These include jet algorithm effects (*e.g.* out-of-cone effects), initial and final state QCD radiation, presence of the underlying event, fragmentation, pile-up event (in the same bunch-crossing).

A non-trivial task for the calibration procedure in general is to disentangle instrumental effects from physics effects. The main approach to perform this separation is to apply various *in situ* (*i.e.* using ATLAS *pp* collision data) calibration methods at different reconstruction levels.

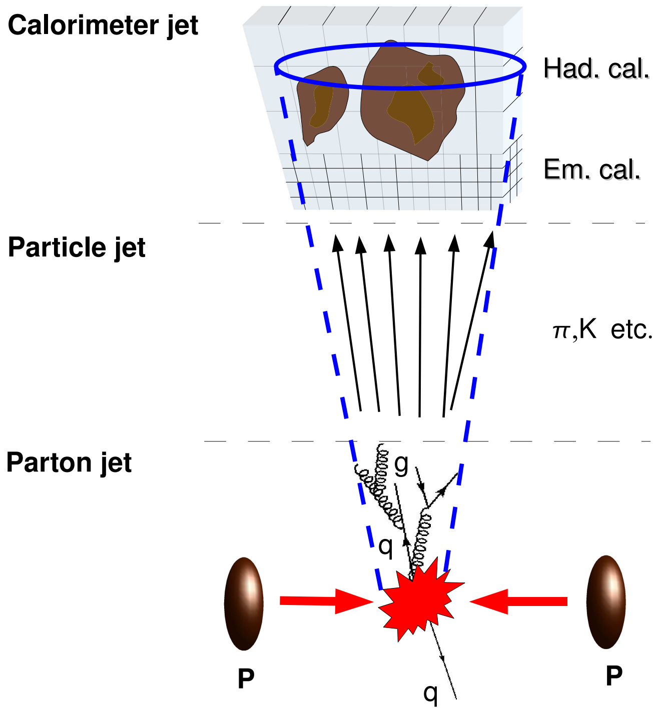

Figure 7.1: Evolution of the partonic system.

7.1.1 Electromagnetic scale

The input to the jet energy reconstruction and calibration procedures is the energy deposited in the calorimeter cells. This energy is measured at the electromagnetic (em) scale. The em scale is defined by the electron calibration constants c_e. These constants are obtained in test-beam measurements. The calibration constant c_e is defined as the average ratio of the signal $\mathcal{Q}$ of a given calorimeter, typically a charge, and the energy E_{dep} deposited by electrons inside the calorimeter at a certain beam energy [78]:

$$c_e = \frac{\mathcal{Q}}{E_{dep}}, \tag{7.1}$$

Thus, the energy reconstructed at the em scale for a given cell is defined by:

$$E_{em} = c_e \times q_i, \tag{7.2}$$

where q_i is the charge signal in a given calorimeter cell i. Obviously, the uncertainties of the calibration coefficients c_e and of q_i contribute to the error of E_{em}. Taking into account the intrinsic linearity of the electron signal, the calibration coefficients are supposed to be independent of the deposited energy. The presence of the upstream dead material introduces an uncertainty of E_{dep} especially at lower energies and as a result contributes to the error of c_e and the em scale. The measurement of the charge is affected by the imperfections in the readout electronics like gain variations in electronic components and detector instrumental effects. Various calibration systems implemented in the calorimeter provide a set of tools to monitor and correct for detector and electronics imperfections at readout level.

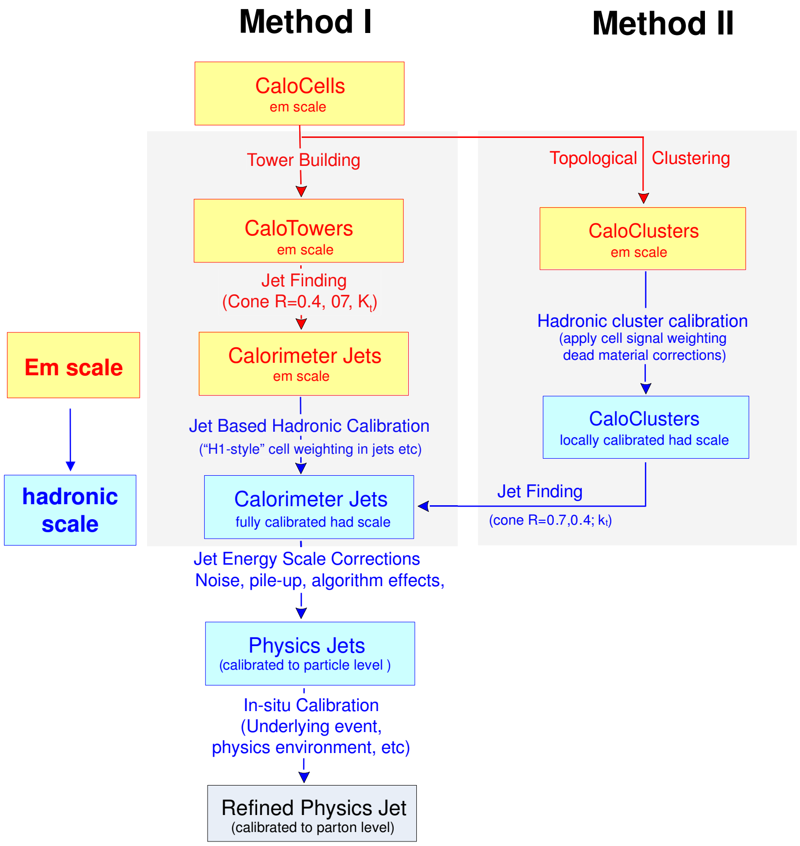

Figure 7.2: Simplified diagram of the calibration chain in ATLAS [79].

The *in situ* calibration using *e.g.* $Z \to e^+e^-$ events can provide a useful cross-check or additional corrections for the calibration performed by the systems at hardware level.

7.1.2 Reconstruction and calibration chain

The ATLAS jet reconstruction and calibration is a multi-step procedure. The main steps of this procedure are shown in Figure 7.2. Currently two different methods for jet reconstruction are adopted:

- Method I. The jet reconstruction is based on the projective calorimeter towers[1].
- Method II. The jet reconstruction is based on topological clusters.

The energy deposits in the calorimeter cells are the input data to both methods. In the first method, based on the cells, projective calorimeter towers with size 0.1×0.1 in $\eta \times \phi$ are built. Jet cluster algorithms applied to the towers produce calorimeter jets calibrated at em scale. To obtain jets at hadronic scale[2] several calibration methods can be applied. By default the "H1-style" calibration method is used.

---

[1] The boundaries of the projective towers point to the interaction vertex. The energy in calorimeter tower is calculated by summing up energy deposits of all cells (electromagnetic and hadronic) within this tower.

[2] A hadronic scale is achieved by calibration for effect of non-compensation in calorimeter. At hadronic scale the response to hadrons is equivalent to that of electrons.

The "H1-style" calibration is based on a technique which computes a set of weights to be applied to single cell energies in the reconstructed jet. The calibrated jet energy then can be expressed:

$$E_{calib} = \sum_i w_i \times E_i, \tag{7.3}$$

where w_i are the weights and E_i is the energy in a single cell. The cell weights depend on the energy density in the cell and the energy of the reconstructed jet. The energy density is higher for the cells which contain contributions from electromagnetic parts of the shower. Thus, the separation is done between cells with electromagnetic and hadronic contributions. The weights are computed by minimizing the resolution of the calorimeter jet energy with respect to that of particle jet closest in $\eta \times \phi$. Finally the procedure provides the weights which depend on energy and pseudorapidity. The calibration procedure allows us to recover the linearity at the hadronic scale and improve the jet energy resolution. The details of the implementation of the cell weighting calibration procedures can be found in [80][81].

Another approach for the jet energy reconstruction currently under intensive study in ATLAS is based on topological clusters. These clusters are formed from the calorimeter cells which satisfy the signal significance conditions, that means that they pass the signal-to-noise ratio threshold. This scheme naturally suppresses the noise contributions to the reconstructed energies. Then the clusters are calibrated to the hadronic scale, taking into account the effects of dead material in front of the calorimeters. Thus, the jets are built from pre-calibrated topological clusters [82].

As a result of the hadronic calibration, one obtains calorimeter jets at the hadronic scale. The calibration of calorimeter jets can be cross-checked, and corrections for the calorimeter instrumental effects are applied at this level by an *in situ* calibration. The calibration procedure based on QCD dijet events which provides a cross-check of the hadronic calibration for the calorimeter jets, and which can be applied to improve the jet energy scale, has been studied and is discussed in the next section of this chapter.

Finally, the particle jet obtained after the calibration steps described above has to be calibrated to the parton jet level and the absolute jet energy scale has to be determined. The absolute jet energy scale is being recovered by comparison of real data with MC predictions and by applying the *in situ* calibration methods based on the p_T balance between jet and γ or the Z boson in γ/Z+jet events. Also the hadronic decay $W \rightarrow$ jet+jet can be used to establish the absolute jet energy scale at parton level.

7.2 Calorimeter calibration systems overview

Several systems are implemented at the level of front-end electronics for calibration and monitoring of the calorimeters during data taking.

In the LAr calorimetry the calibration of the on-detector readout electronics is performed by the pulse injection system. Precisely known pulses which simulate the energy deposits in the cells are injected at the very beginning of the readout electronics chain and used to check the response of the electronics, linearity of the gain, noise level etc. The aim of the LAr calibration system is to calibrate the readout electronics to a precision better than 0.25% [53].

The calibration system shown in Figure 7.3 in the TILECAL is subdivided into three parts:

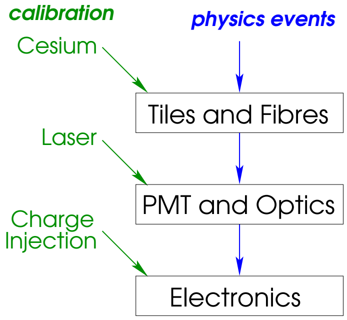

Figure 7.3: Diagram of the TILECAL calibration and monitoring systems.

- **Cesium source system.** The core of the system is movable radioactive source, which passes through every scintillator tile. The system allows to check the quality of the optical response and its uniformity, to equalize the signal response from all cells and to monitor it in time.
- **Laser system.** The main purpose of the laser system is to calibrate and monitor the response of the PMTs with an accuracy better than 0.5%. The laser pulses produced in the system are close to the scintillating light produced by the particles. The system allows one to measure the gain stability and response linearity of the PMTs.
- **Charge injection system (CIS).** The system is designed to calibrate the relative response of the PMT readout electronics. The system allows to control and correct the channel-to-channel variations in the gain of the electronic chain.
- **Minimum bias events.** The MB event rates which are expected to be uniform in the azimuthal angle ϕ will be used to monitor the calorimeter response, dead and hot channels continuously during physics runs.

All calibration systems will be periodically used in ATLAS. For example, it is foreseen to use the CIS and laser system between LHC fills or even interleave physics data with so-called mono-CIS calibration events, which contain the signal with a fixed amplitude injected in gaps between bunch trains in the LHC beam (see Section 2.1).

7.3 *In situ* calorimeter calibration procedure

The goal of the above described calibration systems is to calibrate and to monitor the calorimeter response with a precision better than 1%. The results from the test-beam with electrons show that the cell-to-cell non-uniformity in response after a cesium calibration is better than 3%.

The next step in the calibration procedure is *in situ* calibration with physics data. The *in situ* calibration validates the calibration provided by the hardware systems and applies additional corrections to achieve a higher precision. The study of the calorimeter calibration method described below is inspired by the calibration approaches used at the Tevatron CDF and D0 experiments [85].

The method is referred to as calorimeter intercalibration method. The objective of the method is calorimeter uniformity in response in ϕ and η directions. Naturally the calibration procedure is divided into two steps:

1. ϕ-intercalibration
2. η-intercalibration

The ϕ - intercalibration is based on the fact that the energy flow in the transverse plane for a perfect detector should have a uniform distribution in the azimuthal angle ϕ. The ϕ-intercalibration can be applied at different levels of consideration. The basic approach is to apply the method at the cell or calorimeter tower level at the em scale. Counting the occupancies in the calorimeter towers in a given η-wheel (an example of an η-wheel is shown in Figure 7.4 above a given E_T threshold as a function of ϕ, one can estimate the deviations of the energy scale in single calorimeter towers and then propagate them to the cell layers if the statistics is high enough. At tower or cell level the occupancies are unified, and the corresponding calibration constants are extracted.

Another approach is to perform a ϕ-intercalibration at the jet level. At jet level there is the possibility to use the power of p_T balancing methods. In these methods the momentum conservation in the transverse plane is used to intercalibrate *e.g.* two opposite sectors in calorimeter. The studies performed with p_T balancing methods have shown some difficulties in the application of those for ϕ-intercalibration. The difficulties can be explained by the fact, that using the p_T balance one always calibrates the opposite sectors to each other, as the jets used in the methods are basically back-to-back. The calibration of neighboring sectors is seemed to be rather complicated using these methods. The p_T balance methods are effective tools in the η-intercalibration. The η-intercalibration procedure using p_T balance method will be discussed later.

The alternative to the p_T balancing methods in ϕ-intercalibration is the rate method which is similar to the energy flow method at cell level, but can be applied on jet basis. The method based on counting the integral jet rates as a function of the azimuthal angle ϕ is sensitive to energy miscalibration and provides an easy way to equalize the response in ϕ direction. This method has been studied in detail, and results are presented later in the next sections of this chapter. Here, one can formulate the basic steps for the calibration procedure based on this method:

- Taking into account the fact that the calorimeter towers have a size of 0.1×0.1 in $\eta \times \phi$ use the calorimeter towers as calibration units.
- Divide the calorimeter into wheels in the η range. Each wheel has a width of $\Delta\eta$=0.1 and contains 64 calorimeter towers.
- Calculate the integrated jet rate, *i.e.* the sum of all events above a fixed E_T threshold, for each calorimeter tower in the η-wheel.
- Make the distribution flat in ϕ for a given wheel at fixed η and extract the calibration constants.
- Repeat the last two steps for all wheels in the examined η-region.

Although the ϕ-intercalibration method applied at cell level is expected to give more accurate results compared to the jet level, the repetition of the intercalibration on the jet level will give a good cross-check of the uniformity of the em scale and validation of the calorimeter linearity after hadronic calibration. Another advantage of the rate method at the jet level, as compared to the cell level, is the simplicity of the application as it doesn't require the detailed information for calorimeter cells available only in ESD and can be

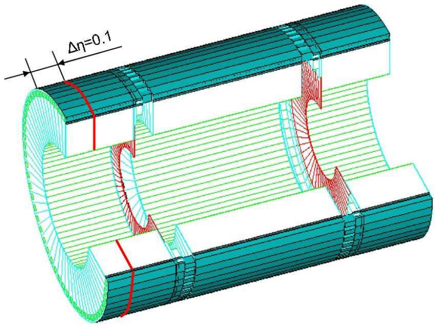

Figure 7.4: Layout view of the Tile Calorimeter barrel and extended barrels [54].

applied at AOD level (see Section 6.1), which is supposed to be standard software level for physics analysis.

After the ϕ-intercalibration the response is equalised across ϕ. The second step is the η-intercalibration. The procedure is performed by applying the dijet p_T balance to intercalibrate different regions of the calorimeter in η. The goal is to achieve (or check) a flat response in η. In the method studied in Section 7.3.4 one calorimeter region in η is chosen as the reference region. This region is supposed to be well understood and properly calibrated. Jets at other pseudorapidities η are calibrated relative to jets in this region. The corrections obtained from the η-calibration are put on top of the ϕ corrections and make the response linear in η direction as well. In the rest of the chapter the studies for both ϕ- and η- calibration steps are presented and discussed.

7.3.1 Data sample preparation

The official CSC[3] production QCD dijet datasets are used in analysis. The datasets have been generated using PYTHIA 6.3 with cross-sections and kinematic cuts according to Table 6.1 in Section 6.4.1, and fully simulated and reconstructed in ATHENA 11.0.42.

The default reconstruction based on the calorimeter towers and calibration scheme referred to as “Method I” has been used for jet reconstruction and calibration. The seeded cone algorithm with a seed value of 1 GeV and split/merge fraction of 0.5 has been used with a jet cone radius R=0.4 and R=0.7.

The produced n-tuples contain the jets with cone size R=0.4 and R=0.7. The n-tuples contain both fully simulated event data and the particle level information for comparison between two levels.

7.3.2 ϕ-intercalibration of the calorimeter using the rate method.

The first study which has been carried out is an estimation of the sensitivity of the rate method to energy miscalibration and the sensitivity dependence on the position of the E_T threshold. The typical differential jet rate expected in ATLAS in a range of $|\eta| < 3.2$ is shown in Figure 7.5. This plot has been obtained by combining all samples J1-J8 weighted by their effective luminosity. A few spikes observed *e.g.* around E_T=500 GeV correspond to the jets which appear at energies far above the maximum cut-off on the hard scale in the PYTHIA generator. The events which contain these jets have much higher

---

[3] Physics data simulated for ATLAS Computer System Commissioning.

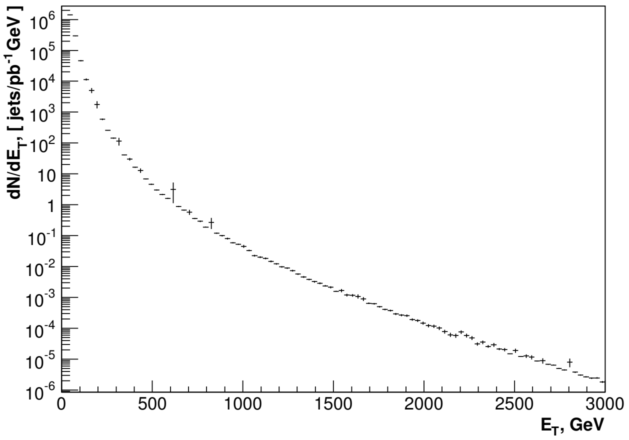

Figure 7.5: Differential jet rate in the range of $|\eta| < 3.2$ at ATLAS simulated with PYTHIA version 6.3.

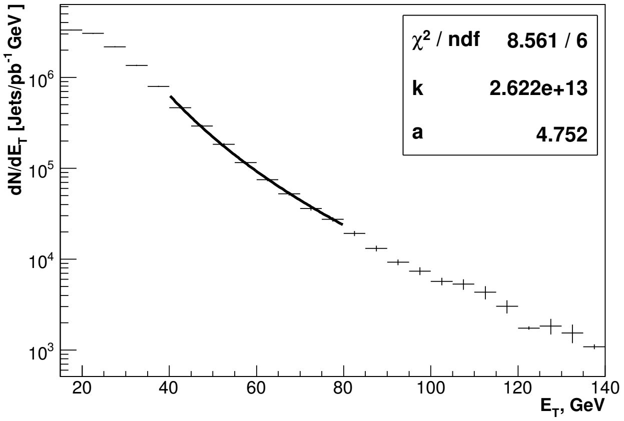

Figure 7.6: Differential jet rate in the low energy range in the central region $0 < \eta < 0.7$.

weights compared to the other events in a given energy range. These jets arise from QCD radiation and underlying event after recent tunes implemented in PYTHIA, and belong to the physics model [86].

The differential jet rate can be fitted by the function:

$$\frac{dN}{dE_T} = kE_T^{-a}, \tag{7.4}$$

where a is fit parameter which reflects the steepness of the curve. Figure 7.5 shows that decrease of the rate depends on the energy range. In addition it depends also on η region. For calibration studies the range of $0 < \eta < 0.7$ with jet energy below 100 GeV has been chosen.

Figure 7.6 shows the fitted by the function eq. (7.4) the differential rate in this range. The parameter a is about 4.7 in the fitted range 30-80 GeV and, as it will be shown later, actually defines the sensitivity of the calibration method.

The effect of energy miscalibration and its reflection in the change of jet rate is shown

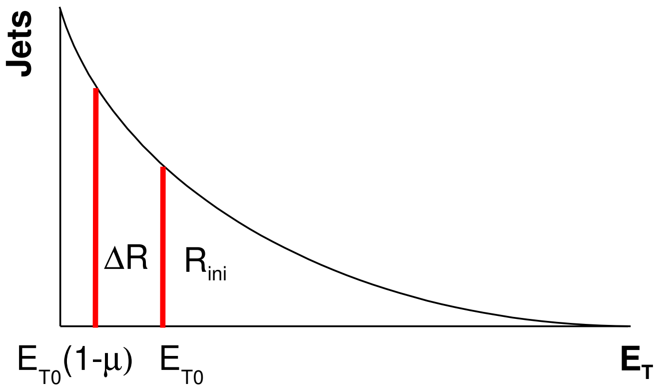

Figure 7.7: The effect of the energy miscalibration on the rate change. The energy is biased as $E_T \rightarrow E_T(1+\mu)$, where μ is the bias. The miscalibration in energy is equivalent to the shift of the E_{T_0} threshold to the $E_{T_0}(1-\mu)$ position and leads to the integral rate change.

in Figure 7.7. The case shown in the plot corresponds to a positive bias *i.e.* to an energy shift $E_T \rightarrow E_T(1+\mu)$, where μ is some miscalibration constant. The jets with energy below the E_{T_0} threshold, but close to it, after the positive bias obtain energies which are above the E_{T_0} threshold and contribute to the positive rate change in the region. The opposite behaviour is observed for the negative bias of the energy scale. In this case some jets which are initially close and above threshold migrate to the energy range which is below threshold, decreasing the number of jets above the threshold.

Now, one can analytically estimate how the energy miscalibration affects the change of the rate [87]. The integrated jet rate above a given threshold E_{T_0} is calculated as follows:

$$R \propto \int_{E_{T_0}}^{\infty} E_T^{-a}\, dE = \frac{E_{T_0}^{1-a}}{a-1} \tag{7.5}$$

In case of an energy miscalibration when the energy scale shifted as $E_T \rightarrow E_T(1+\mu)$ the expression for the changed rate eq. (7.5) can be rewritten as:

$$R' \propto \int_{E_{T_0}(1-\mu)}^{\infty} E_T^{-a}\, dE = \frac{E_{T_0}^{1-a}(1-\mu)^{1-a}}{a-1} \tag{7.6}$$

Subtracting eq. (7.5) from eq. (7.6) and dividing the difference by eq. (7.5) one obtains the expression for the relative rate change as a function of the miscalibration constant μ and a parameter a which is defined in eq. (7.4):

$$\frac{R'-R}{R} = \frac{\Delta R}{R} = (1-\mu)^{1-a} - 1 \tag{7.7}$$

Applying the Taylor series expansion for the eq. (7.7) one gets:

$$\frac{\Delta R}{R} \approx (a-1)\mu \tag{7.8}$$

Setting the value to $a \sim 5$ one can see that in the energy range 40-80 GeV a miscalibration of the *e.g.* 1% gives 4% in the relative rate change:

$$\mu = 1\% \rightarrow \frac{\Delta R}{R} = 4\% \tag{7.9}$$

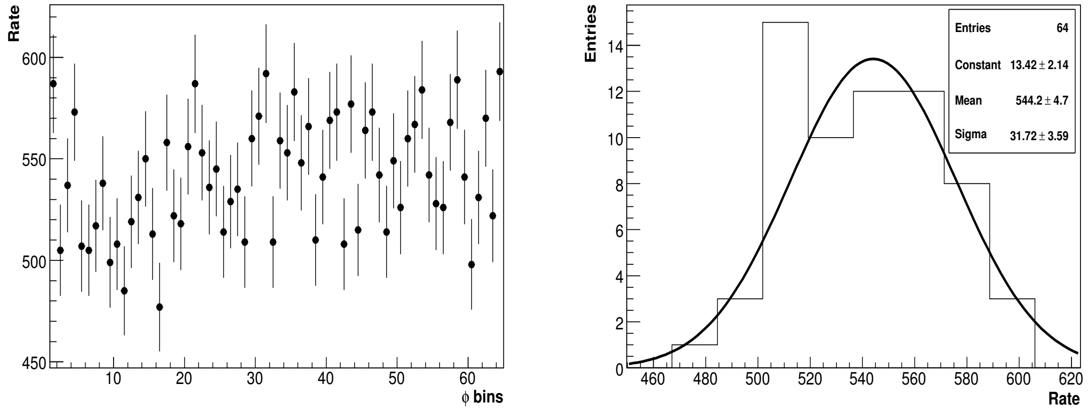

a) b)

Figure 7.8: Rate distribution (a) in 64 sectors of the η-wheel. Each point shows the value of the integrated rate in the corresponding ϕ bin. Gaussian fit (b) applied to the rate distribution.

Thus, having measured the relative rate change $\frac{\Delta R}{R}$ one can find the miscalibration in energy and correct it by setting the corresponding calibration constants. Before coming to the calibration studies based on the explained rate the condition which can affect the accuracy of the calibration method have to be checked:

- The rate distribution in a perfectly calibrated detector obeys Poissonian statistics and really has a uniform distribution across the azimuth.

This check can be performed by analyzing the spread of the distribution versus statistics as described below.

According to the procedure described in Section 7.3 a single η-wheel with $\Delta\eta$=0.5 is chosen in the central part of the calorimeter and divided into 64 sectors.

For the jets falling in each sector the integral rate is calculated. An example of the rate distribution for one η-wheel is shown in Figure 7.8a). A Gaussian fit applied to this rate distribution is shown in Figure 7.8b).

Figure 7.9 shows the distribution of the σ_{rate}/N versus number of events. The σ_{rate} extracted from the Gaussian fit for different number of events. The distribution is fitted according to:

$$\frac{\sigma_{rate}}{N} = \frac{a}{\sqrt{N}} \oplus b. \tag{7.10}$$

As the fit parameters a and b amount to 1 and 0, respectively, one can conclude that jet rate distribution for an ideally calibrated calorimeter obeys a Poissonian statistics and does not have any biases. The error for the value σ_{rate}/N is given by:

$$\Delta\left(\frac{\sigma_{rate}}{N}\right) = \frac{\sigma_{rate}}{N}\sqrt{\left(\frac{\Delta\sigma_{rate}}{\sigma_{rate}}\right)^2 + \left(\frac{\Delta N}{N}\right)^2}. \tag{7.11}$$

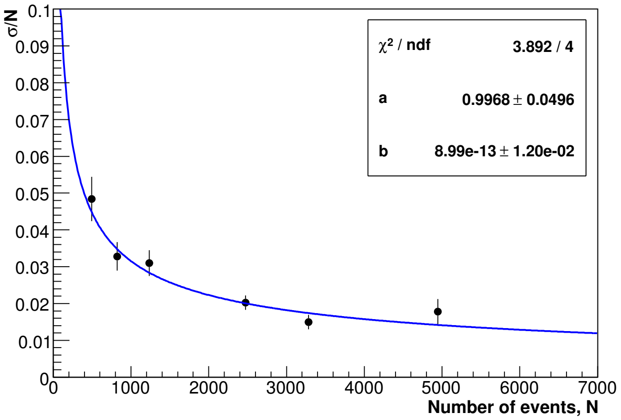

Figure 7.9: Distribution of the σ_{rate} for one wheel versus number of events.

Calibration studies

Since the particular configuration of miscalibration in experimental data is not known, the jet energies have been smeared according to a Gaussian distribution. A miscalibration study has been made for one η-wheel in the central region. The width of the wheel is $\Delta\eta$=0.5. This η-wheel thickness has been chosen to decrease the statistical errors in the study.

For each sector i in a wheel a miscalibration constant ϵ_i obtained from a Gaussian distribution centered at 0, with σ_{miscal}= 5% has been applied. Thus, all jets falling into this ϕ bin have their transverse energies E_T^{miscal} miscalibrated according to:

$$E_T^{miscal} = E_T^{Truth}(1+\epsilon_i), \tag{7.12}$$

where E_T^{Truth} is the initial jet transverse energy. It is assumed that the miscalibration scheme does not have an event-to-event dependence, that means that the miscalibration constants are the same for all events. The distribution of the rates in the η-wheel and the Gaussian fit of this distribution applied after the miscalibration are shown in Figure 7.10. One can notice that the rate distribution becomes broader as expected according to the eq. (7.7), compared to the rate distributions for the initial energy scale shown in Figure 7.8.

The calibration constants have been extracted from the set of miscalibrated dijet events. For each ϕ bin the constant has been determined by the expression:

$$\mu = \frac{R' - N}{N}/(a-1), \tag{7.13}$$

where R' is the integrated rate in a ϕ bin and N is the mean of the rate distribution in a given η-wheel. Figure 7.11 shows a distribution of the extracted calibration constants.

The calibration procedure which then has been applied to the miscalibrated data from another set of the dijet events consists of the following steps:

1. Analyse σ_{rate} in a given η-wheel.
2. If $\sigma_{rate} > \sqrt{N}$, then apply the calibration constants extracted before.

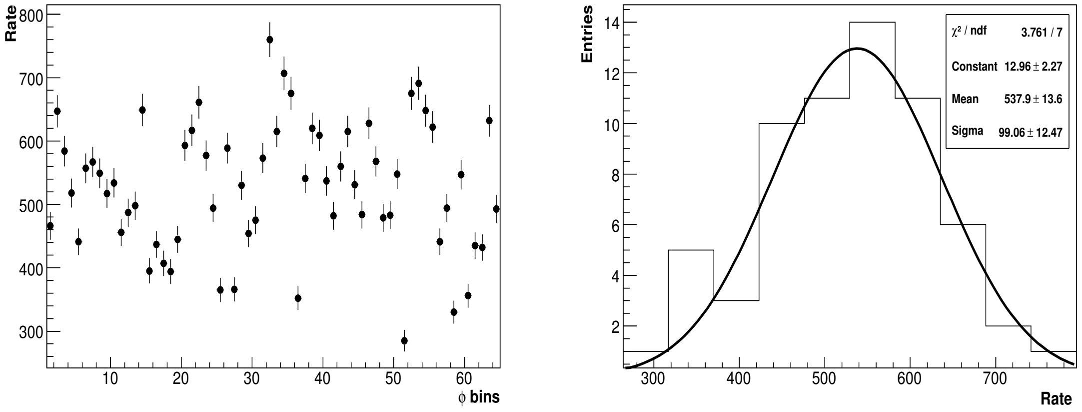

a) b)

Figure 7.10: Rate distribution (a) in an η-wheel after applying the miscalibration constants obtained from the Gaussian distribution with σ_{miscal}= 5%. Gaussian fit (b) to the rate distribution after miscalibration.

The results of this calibration procedure for the rate distribution and jet energy resolution are shown in Figure 7.12. One can see that the calibration procedure returns σ_{rate} of the rate distribution to the value which is smaller than the initial value. The energy resolution distribution has been fitted with a function as defined in Section 28 in eq. (6.3). The coefficients of the sampling, constant and noise terms of the fitting function are given in Table 7.1. One can see that energy miscalibration applied in ϕ basically affects the sampling and constant terms. The applied calibration procedure improves the miscalibrated resolution and returns it to the initial level.

The statistics required to achieve better than 1% precision using the calibration method can be estimated from the following considerations. According to the eq. (7.9) to determine 1% of energy miscalibration one has to achieve $\sim$ 4% in rate deviation. Taking into account that deviation has to be statistically significant it should have $\sim 4\ \sigma_{ini}^{rate}$ deviation,

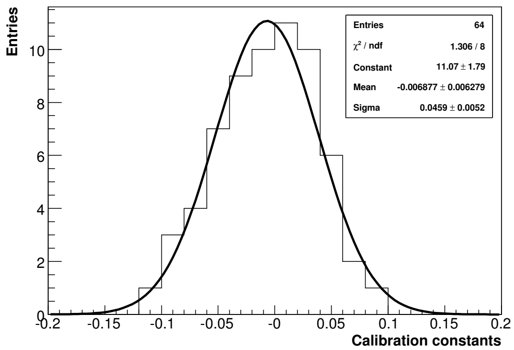

Figure 7.11: Distribution of the calibration coefficients.

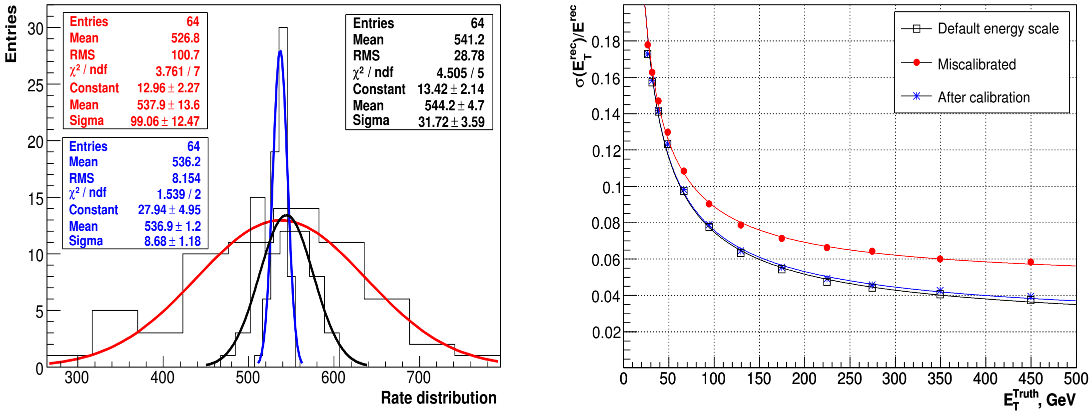

a) b)

Figure 7.12: a) Rate distributions in a single η-wheel: initial rate distribution (black), after energy miscalibration by Gaussian spread with σ of 5% (red), after calibration (blue). b) Jet energy resolution within $0 < \eta < 0.5$: initial scale (black), miscalibrated energies (red), after calibration (blue).

where σ_{ini}^{rate} is the width of the Poisson distribution:

$$\Delta R \simeq 4\sigma_{ini}^{rate} \tag{7.14}$$

These requirements are fulfilled if 10000 events in each calorimeter tower are collected. The σ from 10000 events is:

$$\sigma_{ini}^{rate} = \sqrt{N} = 100 = 1\% \tag{7.15}$$

Thus, $4\sigma_{ini}^{rate}$ correspond to 4% of rate deviation. According to eq. (7.14) and eq. (7.15):

$$\frac{\Delta R}{R} = \frac{4\sigma_{ini}^{rate}}{R} = \frac{400}{10000} = 4\%. \tag{7.16}$$

Figure 7.13 shows the integrated luminosity required to reach the 1% precision for a single calorimeter tower in the central calorimeter region as a function of energy threshold.

Table 7.1: Sampling,constant and noise terms for initial, miscalibrated and calibrated jet energy scale.

Terms	**a, %$\sqrt{GeV}$**	**b, %**	**c, GeV**
Initial scale	62.7	1.9	3.5
Miscalibrated scale	69.1	4.6	3.6
Calibrated scale	62.8	2.3	3.5

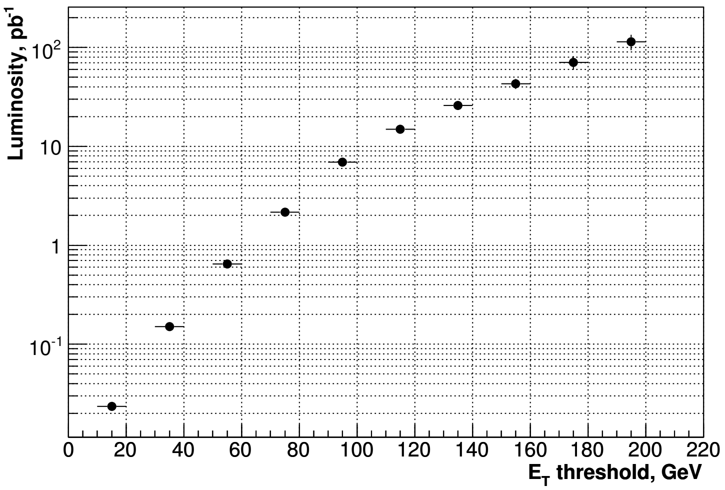

Figure 7.13: Luminosity required to reach precision of 1% in energy calibration in one calorimeter tower versus E_T threshold for the central η region.

The plot in Figure 7.13 does not take the trigger prescaling into account, which is planned for low p_T dijet events. The trigger menu for the initial running period is currently under development. The highest p_T threshold is expected to be at $100 - 150$ GeV, above which no prescaling will be applied. The prescale factors will steeply rise for lower thresholds. For example, a factor of 5 is currently foreseen for $70 < p_T < 100$ GeV, and a factor of 50 for $42 < p_T < 70$ GeV. Scaling the shown luminosity values for *e.g.* E_T threshold of 70 GeV one can see that the remaining statistics will be still sufficient to reach the 1% precision for each calorimeter tower within central region with $10\,\text{pb}^{-1}$ of data.

7.3.3 Beam shift studies

It is well known that the beam at LHC will have some uncertainty in positioning. As a consequence, the interaction vertex will be displaced, affecting the rates uniformity in the azimuthal angle ϕ. The beam displacement can be categorized as follows:

- Beam shift. Parallel shift of the beam with respect to the z axis, typically by a few mm. The beam shift is a fill dependent.
- Beam tilt. The beam is not parallel to the z axis, and has a tilt in x and y coordinates. The value of the beam tilt at Tevatron during the RUN II was ~ 0.8 mrad [84].
- Crossing angle. The angle at which the beams intersect. The expected nominal crossing angle in ATLAS is ~ 285 μrad [36].

In addition the expected vertex distribution (or vertex spread) within a bunch-crossing is a few microns in the transverse plane and a few cm along z axis (currently a Gaussian distribution is used in ATLAS simulations with a sigma of 5.6 cm). While the vertex spread implemented in the simulation does not show any effect on the uniformity of rates, the influence of the other sources of beam misalignment (like beam shift or tilt) is not known.

In this section the effect of beam shift and its possible contribution to the systematic error of the energy calibration based on rates is studied. The study has been performed in several steps:

- Beam shift simulation at the jet particle level.
- Parametrisation of the rate change as a function of beam shift and statistics.
- Estimation of the systematic error due to the beam shift to the energy calibration procedure which was presented in the previous section.

As the simulations for the beam shift are not available in the current ATLAS simulation framework, the effect has been modelled at the particle level of Monte Carlo. The corrections to the (η, ϕ) coordinates of a jet coming from a shifted beam position have been calculated and applied to the jet coordinates at the particle level. This approach allows one to obtain only rough estimation of the effect, if it is significant. For precise studies one has to repeat the full detector simulation for shifted beam position, which accounts for many effects like magnetic field, detector alignment, not accessible at the particle level.

Data sample selection

For the beam shift studies J2 QCD jet data samples have been used. The jets are reconstructed by applying the jet algorithms at particle level. Rates of jets with E_T higher than a threshold value of 40 GeV and cone size R=0.7 are considered in the analysis. The η-wheel has a width of 0.2 in pseudorapidity η.

Beam shift simulation and parametrisation

A geometrical interpretation of the beam shift is given in Figure 7.14. Figure 7.14a) corresponds to a beam shift Δy along the y-axis in the $x - y$ plane. Based on the geometrical considerations for this case the new (η', ϕ') coordinates of the jet are functions of the shift value Δy and the jet coordinates for the nominal beam position. The new coordinates can be calculated as follows:

$$\begin{aligned} \phi' &= \phi_0 + \arcsin\frac{\Delta y \cos\phi_0}{R}, \\ \eta' &= -ln(\tan(\theta'/2)), \; where\ \theta' = \arctan\frac{R + \Delta y \sin\phi_0}{R\cot\theta_0}, \end{aligned} \tag{7.17}$$

where R =1690 mm is the calorimeter radius, ϕ_0 and θ_0 are initial azimuthal and polar angles, respectively. In general case for an arbitrary beam shift $(\Delta x, \Delta y)$ in the $x-y$ plane eq. (7.17) can be rewritten as:

$$\begin{aligned} \phi' &= \phi_0 + \arcsin\frac{(y' - x'\tan(\phi_0))\cos\phi_0}{R}, \\ \eta' &= -ln(\tan(\theta'/2)), \; where\ \theta' = \arctan\frac{R + \sqrt{x'^2 + y'^2}\cos(\phi_0 - \arctan(y/x))}{R\cot\theta_0}, \end{aligned} \tag{7.18}$$

where the x' and y' are the new beam coordinates in the $x - y$ plane. The corrections in eq. (7.18) have been applied to the initial (η, ϕ) jet coordinates. As expected, the uniformity of the rate distribution in azimuthal angle is affected by the shifted beam position.

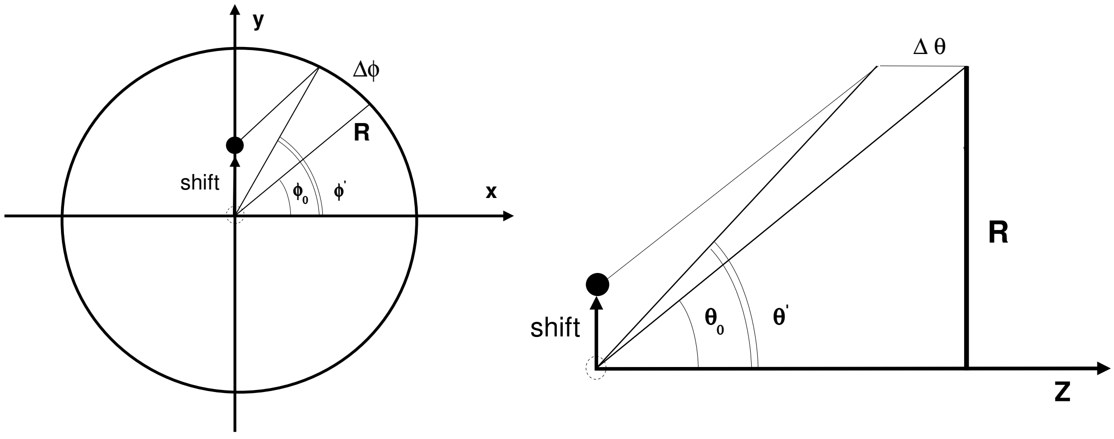

a) b)

Figure 7.14: Geometrical representation of the shift of the beam position in $x-y$ (a) and z plane (b).

An example of the rate distributions in a single η-wheel in the central region for two beam shifts along y axis, Δy=200 mm and Δy=50 mm, is shown in Figure 7.15. The huge values of the beam shift used in the example are chosen to demonstrate the beam shift effect, while for beam shift values close to a real few mm the effect is not visible within statistical fluctuations due to the limited statistics (700k events in J2 sample). To study

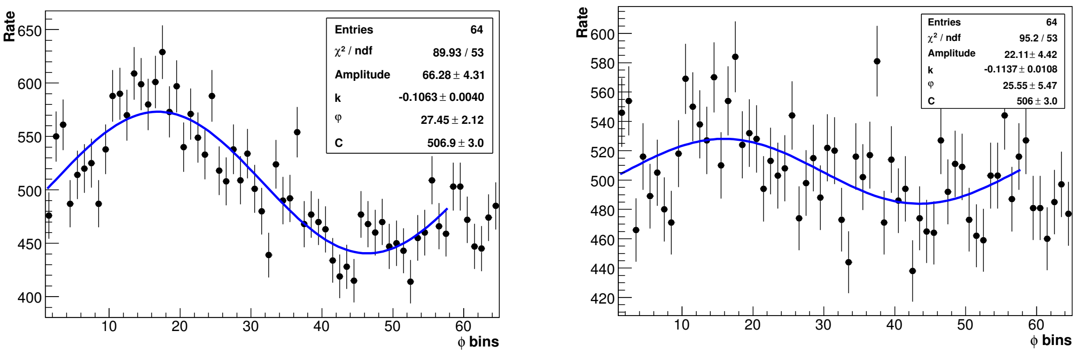

a) b)

Figure 7.15: Rate distributions fitted by a sine function for two beam shifts along the y axis: a) Δy=200 mm; b)Δy=50 mm.

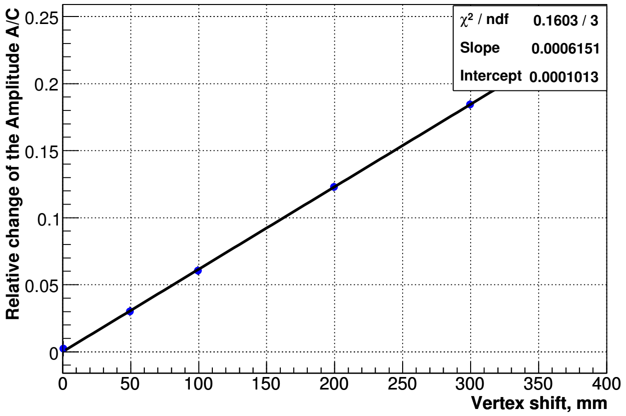

Figure 7.16: Relative change of the amplitude (in fitting sine function) versus beam shift.

the beam shift at a few mm scale, the rate distributions for large beam shifts (order of cm) have been fitted by a sine function:

$$F(x) = A\sin(kx + \varphi) + C \tag{7.19}$$

where A is an amplitude and C is a constant which represents an offset. Fits using eq. (7.19) have been done for the several beam shifts: 50 mm, 100 mm, 200 mm, 300 mm. The ratio of amplitude and offset extracted from the fit functions defines the relative amplitude change for different beam shifts. Figure 7.16 shows this relative amplitude change versus beam shift, fitted by a linear function. From Figure 7.16 one can see that the amplitude scales linearly with the beam shift. The relative amplitude change for small beam shifts can be extracted from the linear fit.

At this point a parametrisation of the rate as a function of beam shift and number of events using eq. (7.19) is done. The rest of the study has been performed using a toy MC model. The following steps can be summarised as follows:

- Simulate the rate distribution in the η-wheel according to parametrisation for different beam shifts and event numbers.
- Fit the rate distributions and extract σ_{Rate}.
- Parametrise σ_{Rate} as a function of beam shift and number of events σ_{Rate}=F(shift,N$_{events}$).
- Estimate the beam shift contribution to the error of the energy calibration procedure described in the Section 7.3.2.

Figure 7.17 shows an example of the σ_{rate} distribution with and without shift of the beam position versus number of events. As discussed in Section 7.3.2, the rate distribution for the nominal beam position obeys the Poissonian statistics and is referred to as σ_{ini} in Figure 7.17. The distribution of σ_{final} corresponds to a beam shift of Δy=20 mm. The difference between σ_{final} and σ_{ini} defines σ_{shift} contribution to the rate change coming from the beam shift. The distribution of σ_{final} is parametrised by the function:

$$\sigma_{rate}^{final} = \alpha N^{0.3} + \beta N + \gamma, \tag{7.20}$$

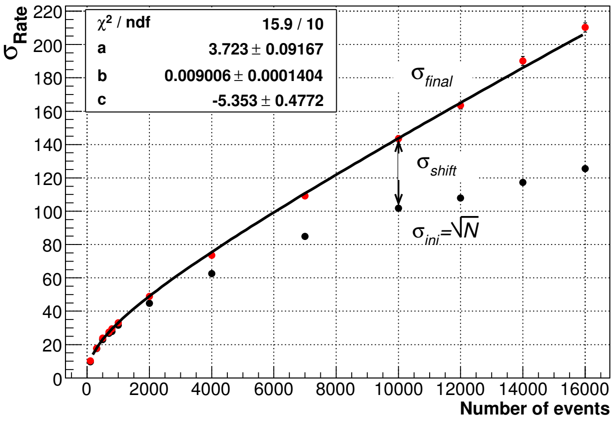

Figure 7.17: σ_{Rate} distribution without and with beam shift (Δy=20 mm) as a function of number of events.

where N is number of events, and α, β, γ are the fitting parameters. The fitting procedure has been repeated for several beam shifts: 0 mm, 10 mm, 20 mm, 30 mm. The extracted parameters α, β, γ of the function in eq. (7.20) have been fitted by the second order polynomial. The results of these fits are shown in Figure 7.18. Finally a full parametrisation of σ_{final} as a function of the beam shift and number of events is obtained. The values for σ_{final} obtained for different beam shifts for the required 10000 events are given in Table 7.2. Now one can estimate the systematic error contribution due to the beam shift to the energy calibration based on the rate method. According to eq. (7.9) and eq. (7.13) the relative error of energy calibration is:

$$\frac{\Delta E}{E} = \frac{1}{4}\frac{\sigma_{final} - \sigma_{ini}}{R} \tag{7.21}$$

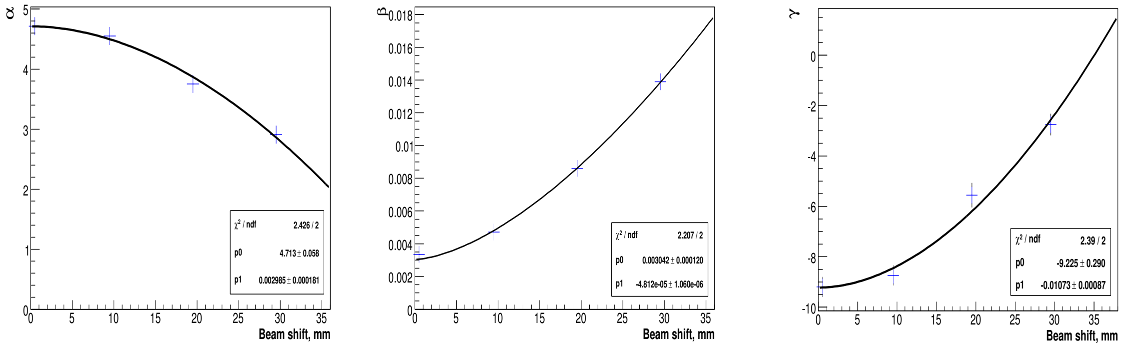

a) b) c)

Figure 7.18: Parameters α, β, γ as function of beam shift. The points are fitted by second order polynomial.

Table 7.2: Table of σ_{Rate} for initial and shifted beam position for 10000 events.

Beam shift	σ_{ini}	σ_{final}	σ_{shift}
2 mm	100.53	101.81	< 1%
4 mm	100.53	102.17	1.63%
6 mm	100.53	104.57	4.04%
8 mm	100.53	107.07	7%

where R is the rate equal to 10000 events. From this the energy error *e.g.* for a beam shift 4 mm is $\sim$ 0.005%. This small contribution to the energy error is obtained for the η-wheel in the central region, where the jets or other particles are mostly affected by the beam shift. In the regions with higher η values the contribution from the beam shift is even smaller than in the example above.

The effect of beam tilt can be approximated by the beam shift in the transverse plane as a function of η. The effect of the tilt is higher for jets with higher η values. Assuming a tilt of 1 mrad (the beam tilt at Tevatron) the corresponding maximum beam shift is 6 mm. According to Table 7.2 this shows that the beam tilt also negligibly affects the energy calibration.

7.3.4 η-intercalibration of the calorimeter

As discussed in Section 7.3 to intercalibrate the different regions in the calorimeter dijet p_T balance can be used. In the proposed method the p_T balance is applied to the two leading jets in two different calorimeter regions in the pseudorapidity η. One region is referred to as reference region, while the another one is referred as probe region. The reference region is supposed to be well understood and properly calibrated. Jets in the probe region are calibrated relative to jets in the reference region. The p_T balance between the two leading reconstructed jets can be defined in several ways, *e.g.* as:

$$B = \frac{p_T^{\text{probe}}}{p_T^{\text{ref}}} , \tag{7.22}$$

or as

$$A = \frac{p_T^{\text{probe}} - p_T^{\text{ref}}}{(p_T^{\text{probe}} + p_T^{\text{ref}})/2} , \tag{7.23}$$

where p_T^{ref} is the transverse momentum of the jet in the reference region, and p_T^{probe} is that of the jet in the region to be calibrated.

In order to choose a better definition, both quantities have been studied in events with both jets in the same region $|\eta| < 0.7$, from which one jet was randomly chosen as the reference one and the other as the probe jet. The first definition is intrinsically asymmetric, as shown in Figure 7.19a). This asymmetry can be easily understood from its asymptotic behaviour: for $p_T^{\text{ref}} \to \infty$, $B \to 0$, while for $p_T^{\text{ref}} \to 0$, $B \to \infty$. This asymmetry can affect the mean value obtained from a Gaussian fit. The second definition of p_T balance is symmetric, as shown in Figure 7.19b) and is preferable.

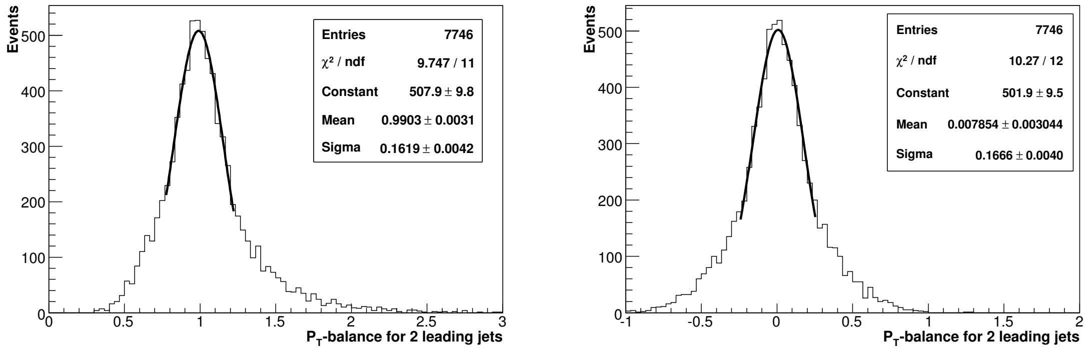

a) b)

Figure 7.19: The p_T balance distributions as measured with both jets in the central region $|\eta| < 0.7$ for two definitions of the balance: a) eq. 7.22; b) eq. 7.23.

The p_T balance is affected by calorimeter instrumental effects, such as the calorimeter calibration, dead material, noise etc., and also by physics of dijet events, such as initial and final state gluon radiation, underlying event, fragmentation, the jet reconstruction algorithm etc. Both physics and instrumental effects can depend on η. Jets in central and forward regions with the same p_T are quite different in energy. It is important to disentangle calorimeter effects from physics in order to correct only for the calorimeter effects. To limit ISR/FSR, a cut on the azimuthal angle between the two jets $\Delta\phi > 3$ is applied. This cut makes the distributions for both p_T balance definitions more narrow, and also reduces the effect of the intrinsic asymmetry for the first p_T balance definition. Figure 7.20 shows the distribution of the extracted mean values of p_T balance distributions

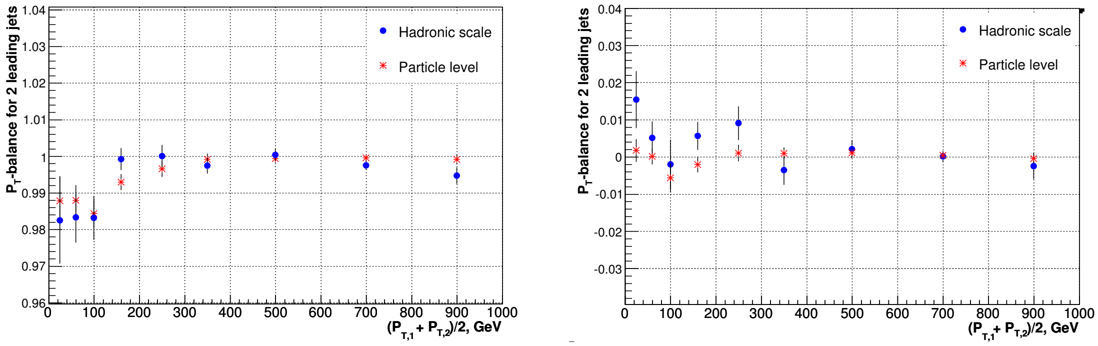

a) b)

Figure 7.20: The fitted mean p_T balance as a function of the of half sum p_T of two leading jets for both definitions of the p_T balance: eq. 7.22 (left), eq. 7.23 (right).

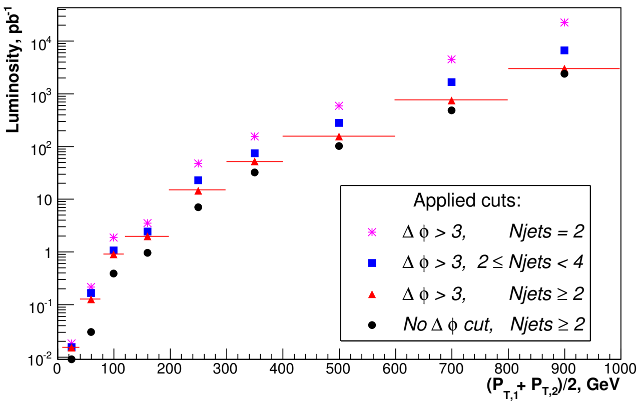

Figure 7.21: Integrated luminosity required to reach 0.5% precision as a function of p_T in the probe region $0.7 < \eta < 0.8$ with different sets of cuts: all dijet events (black circles), $\Delta\phi > 3$ between the two leading jets (red triangles), in addition to $\Delta\phi$ cut, less than 4 jets in an event (blue squares), exactly two reconstructed jets (magenta stars). The reference region is $0 < |\eta| < 0.7$.

fitted by Gaussian as a function of p_T. One can see that some deviations from perfect balancing is still present and have an order of $\sim 1-2\%$ for $p_T < 100\,\text{GeV}$, both for truth and for reconstructed jets.

The additional cuts can be applied to obtain a better p_T balancing in dijet sample and thus to reduce the width of the p_T balance distributions. The cuts based on the reduction of the number of jets in the events have been studied below. For example, the total number of reconstructed jets with $p_T > 10\,\text{GeV}$ can be limited to $N_{\text{jet}} < 4$ or even to $N_{\text{jet}} = 2$. These cuts should suppress the asymmetry in the p_T balance distributions. However, these additional cuts significantly reduce the statistics of the sample, as shown in Figure 7.21. This Figure shows the integrated luminosity required to reach a statistical precision of 0.5% of the p_T balance fit mean value in the probe range $0.7 < \eta < 0.8$, where $0 < |\eta| < 0.7$ is defined as the reference region. The luminosity values are shown for different sets of cuts. The cuts on N_{jet} reduce the statistics by a factor of $5-10$.

These cuts are not necessary if one uses the second definition of the p_T balance. Without these cuts, 0.5% precision can be reached in this η region with $10\,\text{pb}^{-1}$ of data for $p_T \lesssim 300\,\text{GeV}$, and with $100\,\text{pb}^{-1}$ for $p_T \lesssim 500\,\text{GeV}$.

Similar plots have been done for the other η regions. Higher integrated luminosities are required for larger η at the same p_T values, compared to the central region. On the other hand, the size of the reference region can be increased sequentially, namely, as soon as one η has been checked or recalibrated, it can be added to the reference region to study the next η range.

Calibration studies

For calibration studies the reference and probe regions have been defined in $0 \leq \eta < 0.6$ and $\eta < 3.2$, respectively. The p_T balance distributions have been studied in 4 different p_T bins:

- 10-50 GeV

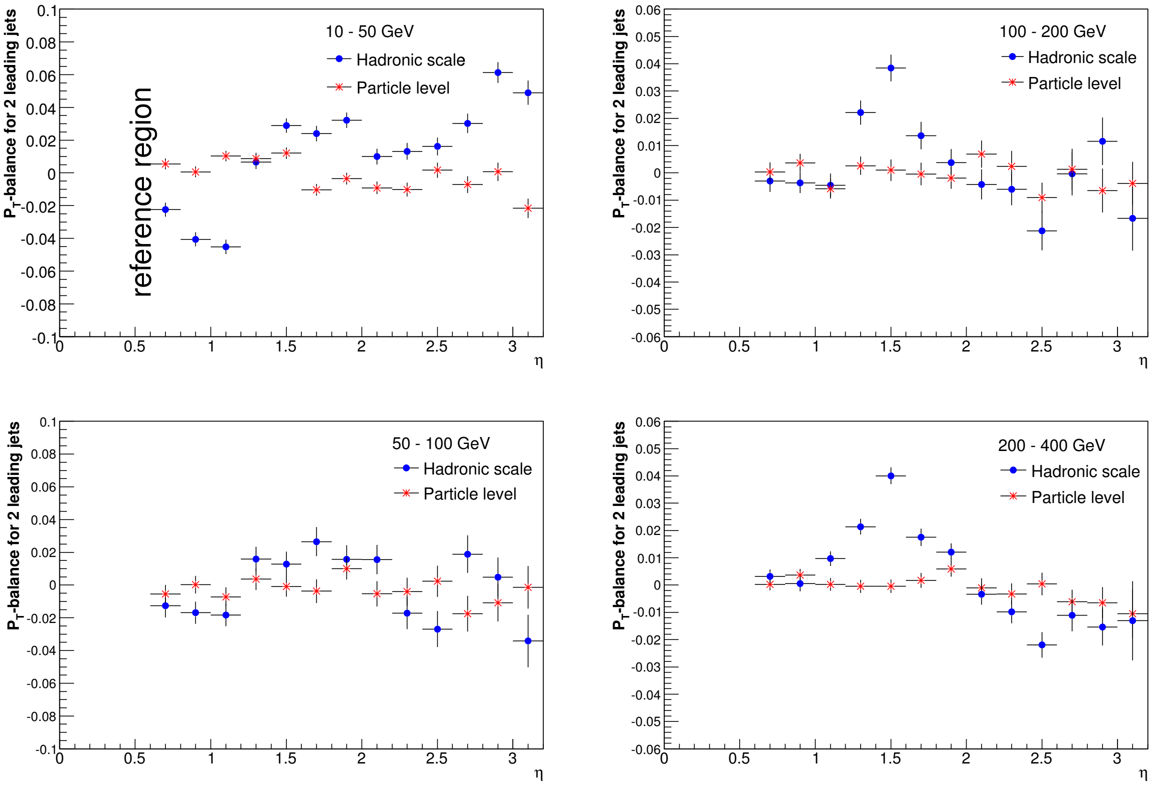

Figure 7.22: p_T balance A across the full η region in 4 p_T bins: 10-50 GeV (left-top), 50-100 GeV (left-bottom), 100-200 GeV (right-top) and 200-400 GeV (right-bottom) for particle level jets (red crosses) and for fully simulated jets at hadronic scale (blue circles).

- 50-100 GeV
- 100-200 GeV
- 200-400 GeV

Figure 7.22 shows the p_T balance A for particle level jets and for fully simulated jets at the hadronic scale. The p_T balance is quite flat across the full η region for particle jets, while for fully simulated jets detector and calibration effects are observed in some regions, in particular in the crack region between the barrel and the endcap section of the calorimeter around $\eta = 1.5$.

According to the eq. (7.23) the calibration coefficients have been calculated to restore the balance of fully simulated jets across η. The results for two p_T bins are shown in Figure 7.23. A check of the procedure is performed with the Monte Carlo simulation by looking at the response $r = P_T^{\mathrm{rec}}/P_T^{\mathrm{truth}}$ before and after the correction. An example is given in Figure 7.24 for jets in the 200-400 GeV range.

The calibration procedure can be further improved by plotting the calibration coefficients as functions of p_T and fitting them, as shown in Figure 7.25 for two η bins: the transition region $1 < |\eta| < 1.2$ between the central barrel and the forward barrel, and a forward region $2.6 < |\eta| < 2.8$. The observed p_T dependences result from energy losses and from the currently used jet calibration.

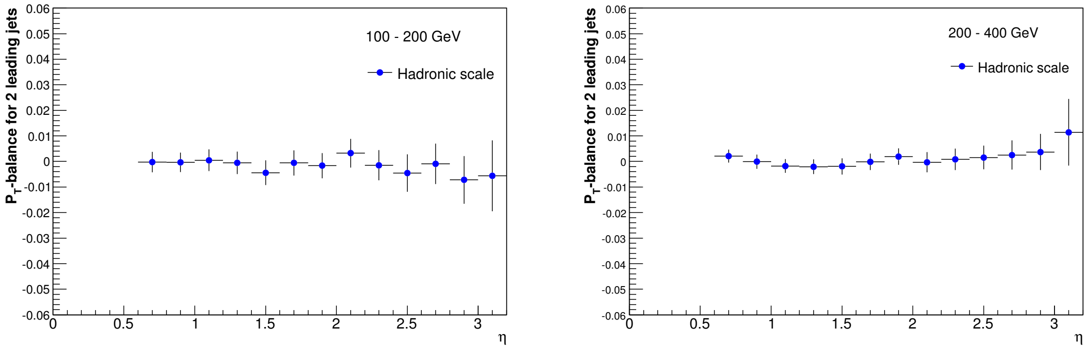

a) b)

Figure 7.23: p_T balance A after the calibration across the full η region in 2 p_T bins: a) 100-200 GeV; b) 200-400 GeV.

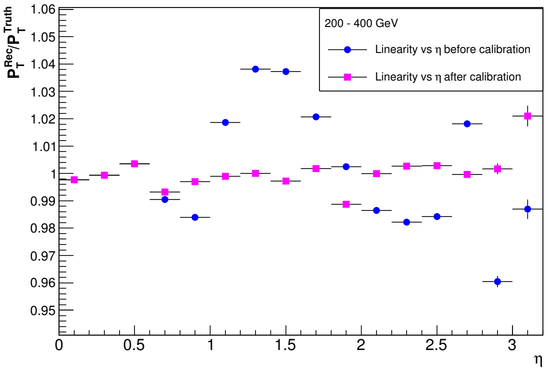

Figure 7.24: Response r before (blue) and after (red) the correction across the full η region.

Further cross-checks of systematic effects can be made. One of them is to study the η dependence of the leading and sub-leading jets multiplicity. Figures 7.26 shows the distributions for particle jets and for fully simulated jets. While for particle jets, there is no difference between leading and sub-leading jets, for fully simulated jets the number of sub-leading ones is smaller in crack regions which are overcalibrated with respect to the central region as was shown in Figure 7.22. Thus the sub-leading jets are swapped by the leading ones. After the calibration the effect vanishes.

7.4 Summary

A multi-step procedure is applied to the jet energy measured in detector to recover the absolute Jet Energy Scale. The calorimeter calibration is only one, but essential step in this procedure. The systematics coming from calorimeter measurements will significantly

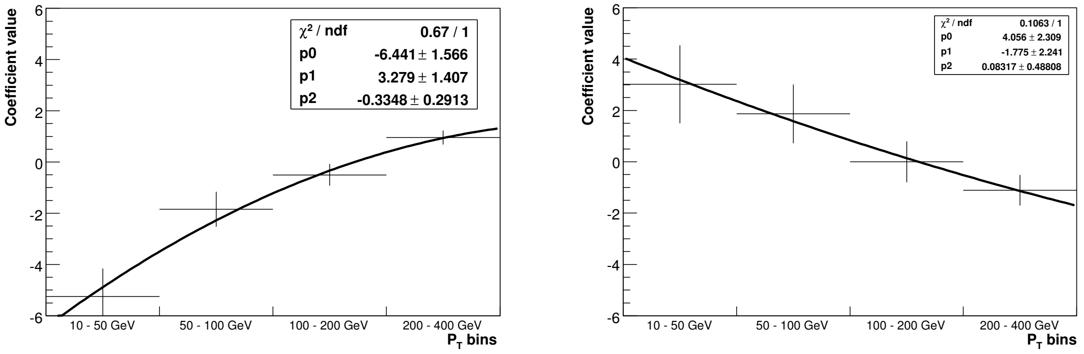

a) b)

Figure 7.25: Calibration coefficients as functions of jet p_T for two η bins: a) $1 < |\eta| < 1.2$; b) $2.6 < |\eta| < 2.8$. The points are fitted by second order polynomial.

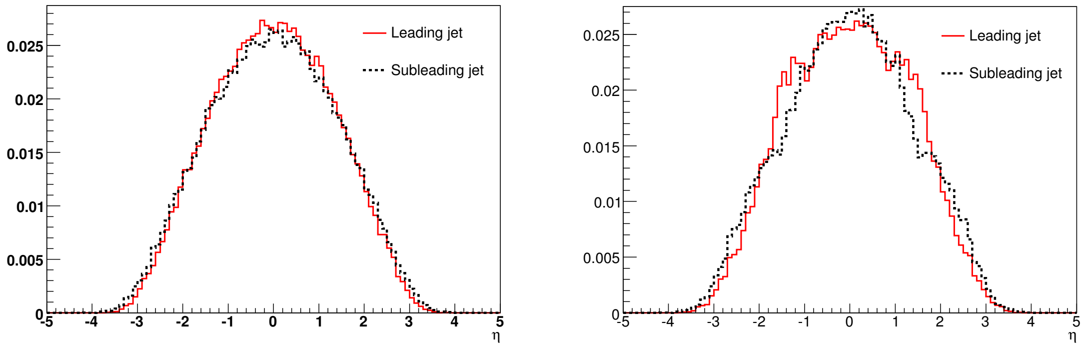

a) b)

Figure 7.26: η dependence of the leading and sub-leading jet distributions: a) for particle jets; b) for fully simulated jets.

contribute to the error of the Jet Energy Scale which in turn affects the precision of *e.g.* the jet cross-section measurements.

The developed calorimeter calibration methods described in this chapter exploit the rich statistics of QCD dijet events. The uniformity of the response in azimuthal angle ϕ is checked and calibrated by applying a method which is based on the jet rate calculation. The studies have shown a high sensitivity of the method to the energy miscalibration. The method improves the constant term in the resolution function. The effect of beam shift and tilt has been studied as a source of the systematic error to the rate method and shown a negligibly small contribution to the error of the method.

The uniform linearity of the calorimeter response across η is achieved by applying the calibration method based on p_T balancing of the two leading jets in event. Together with instrumental corrections for the imperfections in the calorimeter the method also provides the corrections related to the physics effects like η dependence of the underlying event and pile-up.

For both methods presented in this chapter the statistics estimations have shown that the required accuracy for energy calibration can be achieved during initial data taking.

Conclusions

The work presented in the first part of this thesis is related to the development of quality assurance tests for the main processing component of the Pre-Processor system of the ATLAS Level-1 Calorimeter Trigger. A thorough testing of all functional MCM blocks has been performed. All logic blocks in the PPrASIC have been examined with different test-patterns in all possible modes. The results for the extensive tests of the Multi-Chip Module, which proved it functions correctly are presented. The developed testing procedures were combined in the testing software package, which has been successfully applied to a few thousand Multi-Chip Modules during the large scale production. The results of the production show an overall yield of working MCMs higher than 80%.

In the second part of the thesis the performance of the calorimeter shower parametrisation model implemented in the fast simulation is studied using QCD dijet events. The results of the validation tests of the fast simulation performance with shower parametrisation have shown good agreement between fast and full simulation at the electromagnetic scale for the calorimeter response; however the deviations have been observed in the energy resolution distributions. The deviations are larger in the calorimeter end-cap regions, compared to the central region. The calibration procedure applied to fast simulated data at the electromagnetic scale provides a linear response at the hadronic scale. Again, the main deviations at the hadronic scale have been observed in the jet energy resolutions between fast and full simulation.

Calorimeter *in situ* intercalibration methods based on QCD dijet events are studied in the last part of the work. The objectives of these studies were to find the pertinent methods which can be applied at the hadronic jet energy scale for calorimeter intercalibration, estimate the sensitivity to the energy miscalibration, and the statistical and systematic effects. The intercalibration studies are performed in the azimuth angle ϕ and in pseudorapidity η. The sensitivity of the rate method applied in azimuthal direction to the energy miscalibration is determined. The effect of beam shift and tilt has been studied as a source of systematical error to the rate method and shown a negligibly small contribution to the systematics of the method. The calibration across pseudorapidity η is performed by the p_T balancing method. Together with instrumental corrections for the imperfections in the calorimeter the method also provides the corrections related to the physics effects like η-dependence of the underlying event and pile-up. For both methods the statistics required to reach the desired accuracy in calibration is estimated.

Appendix A

ATLAS kinematics

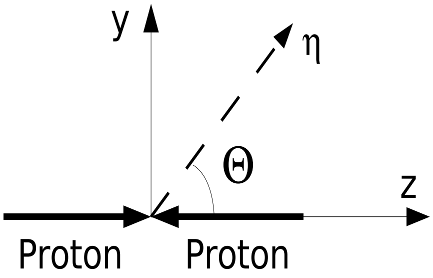

Figure 27: y-z plane.

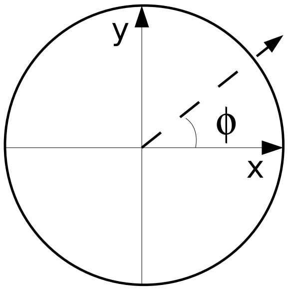

Figure 28: x-y plane.

- The z axis is defined along the beam direction.
- The x-y plane is the plane transverse to the beam direction.
- The azimuthal angle ϕ is measured around the beam axis.
- The polar angle θ is the angle relative to the beam axis.

For a given particle or jet with energy E and 3-momentum $\overrightarrow{p} = (p_x, p_y, p_z)$ the following longitudinally boost-invariant variables are defined:

$$\text{transverse momentum} \qquad p_T = \sqrt{p_x + p_y}, \tag{24}$$

$$\text{azimuthal angle} \qquad \phi = \arctan p_y/p_x \tag{25}$$

The rapidity y and pseudorapidity η are defined with respect to the beam axis:

$$y = \frac{1}{2} ln(\frac{E + p_z}{E - p_z}) \tag{26}$$

$$\eta = \lim_{m \to 0} y = -ln(\tan\frac{\theta}{2}) \tag{27}$$

The pseudorapidity η describes the polar angle θ of the particle or jet which is defined as:

$$\theta = \arctan p_T/p_z \tag{28}$$

In the limit of a massless particle the pseudorapidity equals to rapidity. The usage of rapidity is motivated by its simple transformation under a boost along the beam axis. The difference dy is invariant under longitudinal boosts.

Appendix B

MCM testing menus.

A graphical interface of the Multi-Chip Module testing package in mode ”Full MCM Quality Assurance test” is shown in Figure 29. The testing is performed as a multi-step procedure. The status boxes on the right side display the result for each single test ”Done/Failed”.

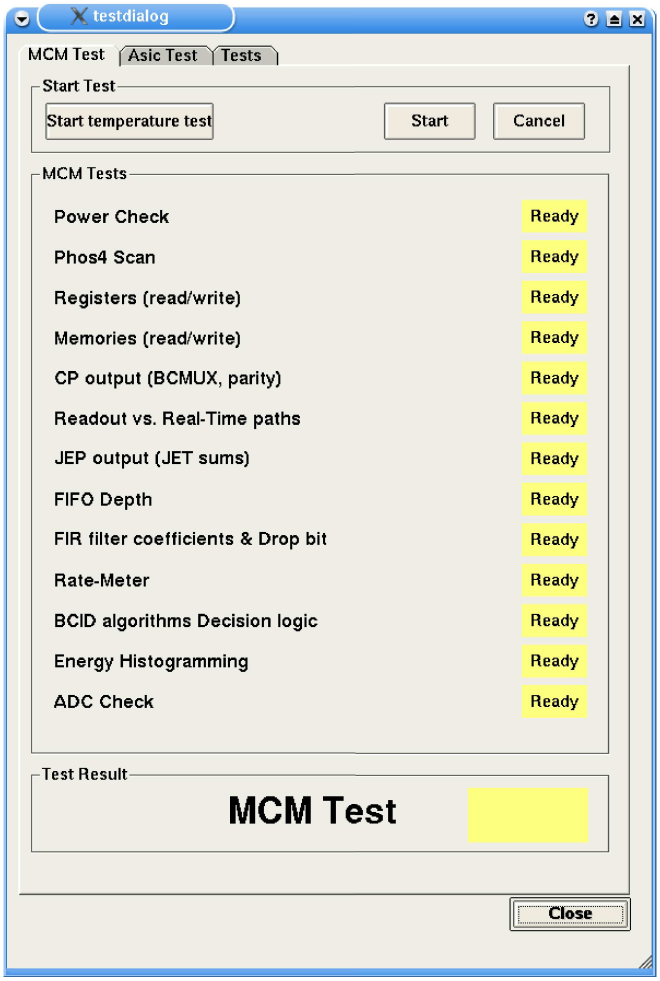

Power Check	Ready
Phos4 Scan	Ready
Registers (read/write)	Ready
Memories (read/write)	Ready
CP output (BCMUX, parity)	Ready
Readout vs. Real-Time paths	Ready
JEP output (JET sums)	Ready
FIFO Depth	Ready
FIR filter coefficients & Drop bit	Ready
Rate-Meter	Ready
BCID algorithms Decision logic	Ready
Energy Histogramming	Ready
ADC Check	Ready

MCM Test

Figure 29: MCM testing package in mode ”Full MCM Quality Assurance test”.

A graphical interface of the Multi-Chip Module testing package in mode ”PPrASIC Wafer test” is shown in Figure 30.

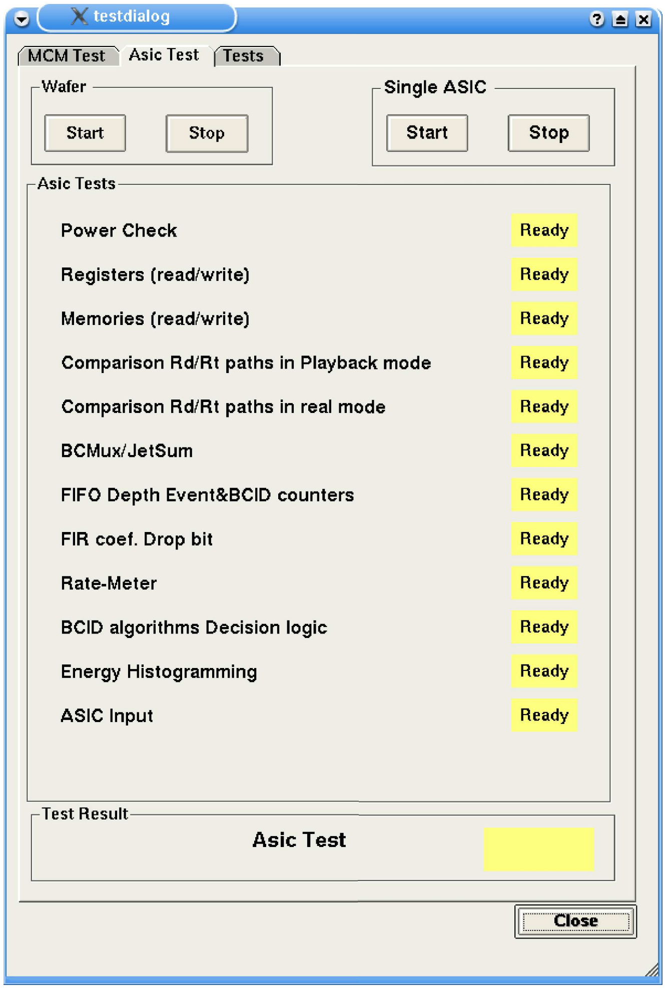

Power Check	Ready
Registers (read/write)	Ready
Memories (read/write)	Ready
Comparison Rd/Rt paths in Playback mode	Ready
Comparison Rd/Rt paths in real mode	Ready
BCMux/JetSum	Ready
FIFO Depth Event&BCID counters	Ready
FIR coef. Drop bit	Ready
Rate-Meter	Ready
BCID algorithms Decision logic	Ready
Energy Histogramming	Ready
ASIC Input	Ready

Figure 30: MCM testing package in ”PPrASIC Wafer test” mode.

A configuration interface contain all the PPrASIC registers is shown in Figure 31. The interface is used in "Debugging mode" for manual PPrASIC configuration.

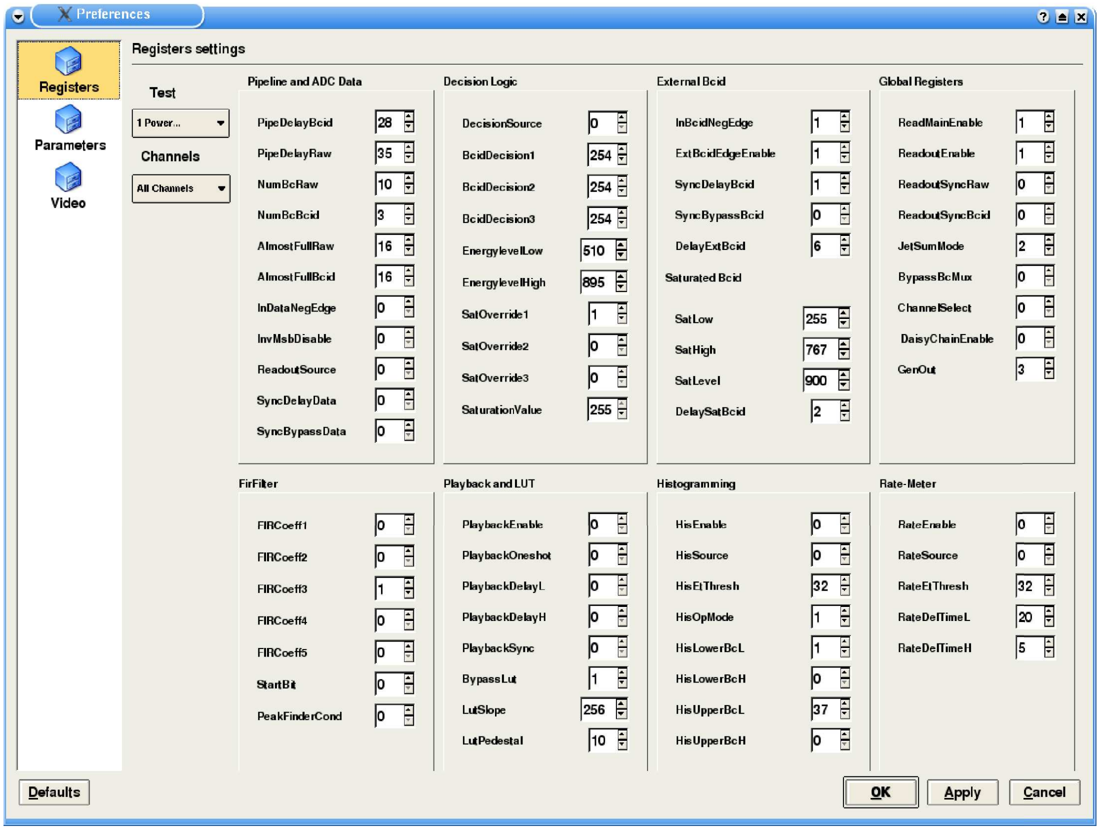

Registers settings

Test: 1 Power...

Channels: All Channels

Pipeline and ADC Data

PipeDelayBcid	28
PipeDelayRaw	35
NumBcRaw	10
NumBcBcid	3
AlmostFullRaw	16
AlmostFullBcid	16
InDataNegEdge	0
InvMsbDisable	0
ReadoutSource	0
SyncDelayData	0
SyncBypassData	0

Decision Logic

DecisionSource	0
BcidDecision1	254
BcidDecision2	254
BcidDecision3	254
EnergylevelLow	510
EnergylevelHigh	895
SatOverride1	1
SatOverride2	0
SatOverride3	0
SaturationValue	255

External Bcid

InBcidNegEdge	1
ExtBcidEdgeEnable	1
SyncDelayBcid	1
SyncBypassBcid	0
DelayExtBcid	6

Saturated Bcid

SatLow	255
SatHigh	767
SatLevel	900
DelaySatBcid	2

Global Registers

ReadMainEnable	1
ReadoutEnable	1
ReadoutSyncRaw	0
ReadoutSyncBcid	0
JetSumMode	2
BypassBcMux	0
ChannelSelect	0
DaisyChainEnable	0
GenOut	3

FirFilter

FIRCoeff1	0
FIRCoeff2	0
FIRCoeff3	1
FIRCoeff4	0
FIRCoeff5	0
StartBit	0
PeakFinderCond	0

Playback and LUT

PlaybackEnable	0
PlaybackOneshot	0
PlaybackDelayL	0
PlaybackDelayH	0
PlaybackSync	0
BypassLut	1
LutSlope	256
LutPedestal	10

Histogramming

HisEnable	0
HisSource	0
HisEtThresh	32
HisOpMode	1
HisLowerBcL	1
HisLowerBcH	0
HisUpperBcL	37
HisUpperBcH	0

Rate-Meter

RateEnable	0
RateSource	0
RateEtThresh	32
RateDelTimeL	20
RateDelTimeH	5

Figure 31: A configuration interface of the MCM testing package.

List of Figures

List of Tables

Bibliography

[1] Francis Halzen, Alan D. Martin,
Quarks & Leptons: An Introductory Course in Modern Particle Physics,
John Wiley & Sons, Inc. (1984).

[2] P. W. Higgs, Phys. Rev. Lett. **13** (1964) 508.

[3] S. Weinberg,Rev. Mod. Phys. 52, 515 (1980).

[4] H. Georgi and S. L. Glashow, Phys. Rev. Lett. **32** (1974) 438.

[5] Lipkin, Harry J., Phys. Rev. D 7, 846 - 852 (1973)

[6] Gell-Mann,
M., 1964a, Phys. Lett. 8, 214

[7] G.Zweig, CERN Reports 8182/TH 401 and 8419/TH 412 (1964) unpublished.

[8] H. W. Kendall, Rev. Mod. Phys. 63, 597 - 614 (1991)

[9] J. D. Bjorken, Phys. Rev. **179**, 1547 (1969).

[10] D. J. Gross and F. Wilczek, Phys. Rev. D **8** (1973) 3633.

[11] J. C. Collins and D. E. Soper, Ann. Rev. Nucl. Part. Sci. **37** (1987) 383.

[12] G. Dissertori, I. Knowles, M. Schmelling,
Quantum Chromodynamics, Clarendon press, Oxford, 2003

[13] V. N. Gribov and L. N. Lipatov,
Yad. Fiz. **15** (1972) 781 and 1218 [Sov. J. Nucl. Phys. **15** (1972) 438 and 675].

[14] Y. L. Dokshitzer, Sov. Phys. JETP **46** (1977) 641 [Zh. Eksp. Teor. Fiz. **73** (1977) 1216].

[15] G. Altarelli and G. Parisi, Nucl. Phys. B **126** (1977) 298.

[16] J. M. Campbell, J. W. Huston and W. J. Stirling, Rept. Prog. Phys. **70**, 89 (2007) [arXiv:hep-ph/0611148].

[17] B. R. Webber,
Hadronization, [arXiv:hep-ph/9411384].

[18] N. Werner [H1 Collaboration], [arXiv:hep-ex/0305109].

[19] P. D. B. Collins and A. D. Martin, Rept. Prog. Phys. **45** (1982) 335.

[20] S. Catani, Y. L. Dokshitzer, M. H. Seymour and B. R. Webber, Nucl. Phys. B **406** (1993) 187.

[21] Y. L. Dokshitzer, G. D. Leder, S. Moretti and B. R. Webber, JHEP **9708** (1997) 001 [arXiv:hep-ph/9707323].

[22] S. Bethke *et al.* [JADE Collaboration], Phys. Lett. B **213**, 235 (1988).

[23] J. E. Huth,N. Wainer, K. Meier *et al.*,
Toward a standardization of jet definitions,
FNAL-C-90-249-E

[24] G. C. Blazey *et al.*,
Run II jet physics,
arXiv:hep-ex/0005012.

[25] B. Abbott *et al.* [D0 Collaboration], Nucl. Instrum. Meth. A **424**, 352 (1999) [arXiv:hep-ex/9805009].

[26] K. C. Frame [D0 Collaboration], SPIRES entry Prepared for 8th International Conference on Calorimetry in High-Energy Physics (CALOR 99), Lisbon, Portugal, 13-19 Jun 1999

[27] M. H. Seymour,
Nucl. Phys. B **513**, 269 (1998),
[arXiv:hep-ph/9707338].

[28] A. Abulencia *et al.* [CDF Run II Collaboration], Phys. Rev. D **74** (2006) 071103 [arXiv:hep-ex/0512020].

[29] S. D. Ellis, Z. Kunszt and D. E. Soper, Phys. Rev. Lett. **69**, 3615 (1992) [arXiv:hep-ph/9208249].

[30] D. Stump, J. Huston, J. Pumplin, W. K. Tung, H. L. Lai, S. Kuhlmann and J. F. Owens, JHEP **0310** (2003) 046
[arXiv:hep-ph/0303013].

[31] M. M. Block and F. Halzen, Phys. Rev. D **73** (2006) 054022
[arXiv:hep-ph/0510238].

[32] S. Keller and J. Womersley, Eur. Phys. J. C **5** (1998) 249
[arXiv:hep-ph/9711304].

[33] A. I. Etienvre, PoS **TOP2006** (2006) 023.

[34] W.J. Stirling,
presented at the Workshop on Theory of LHC Processes,CERN,February 1998.

[35] R. Barate *et al.* [LEP Working Group for Higgs boson searches], Phys. Lett. B **565** (2003) 61,
[arXiv:hep-ex/0306033].

[36] Bruning *et al.*,
LHC design report. Vol. I: The LHC main ring,
CERN-2004-003-V-1

[37] S. Amato *et al.* [LHCb Collaboration],
LHCb technical proposal,
CERN-LHCC-P-4

[38] [ALICE Collaboration],
ALICE: Technical proposal for a large ion collider experiment at the CERN LHC,
CERN-LHCC-P-3

[39] ATLAS experiment,
`http://atlasexperiment.org/atlas_photos.html`

[40] [ATLAS Collaboration],
ATLAS inner detector: Technical design report. Vol. 2,
CERN-LHCC-97-17

[41] C. Grupen, A. Boehrer and L. Smolik, Camb. Monogr. Part. Phys. Nucl. Phys. Cosmol. **5** (1996) 1.

[42] A. Airapetian *et al.* [ATLAS Collaboration],
ATLAS calorimeter performance,
CERN-LHCC-96-40

[43] ATLAS Level-1 Trigger Group,
ATLAS First-Level Trigger Technical Design Report, ATLAS TDR-12, CERN/LHCC/98-14, CERN, Geneva, 1998.

[44] G. Lehmann *et al.*, In the Proceedings of 2003 Conference for Computing in High-Energy and Nuclear Physics (CHEP 03), La Jolla, California, 24-28 Mar 2003, [arXiv:cs/0306101].

[45] M. Grothe *et al.* [ATLAS High Level Trigger Group], Architecture of the ATLAS high level trigger event selection software eConf **C0303241** (2003) WEPT004 [Nucl. Instrum. Meth. A **518** (2004) 537]
[arXiv:physics/0306097].

[46] S. Stancu, M. Ciobotaru and K. Korcyl, IEEE Trans. Nucl. Sci. **53** (2006) 826.

[47] Z. Hajduk *et al.*,
The S-LINK in the data sources for trigger demonstrators in the LHC environment.
Proceedings of the Xth IEEE Real Time Conference, 1997

[48] H.P. Beck *et al.*
Performance of the final Event Builder for the ATLAS,
Proceedings of Xth IEEE Real Time Conference 2007

[49] G. Duckeck *et al.* [ATLAS Collaboration],
ATLAS computing: Technical design report,
ATLAS-TRD-017

[50] [ATLAS Collaboration],
ATLAS high-level trigger, data acquisition and controls: Technical design report,
ATLAS-TRD-016

[51] J. R. A. Booth *et al.*,
Commissioning Experience with the ATLAS Level-1 Calorimeter Trigger System,
IEEE Transactions on Nuclear Science,
RT2007-TDAQ-TRIG08, CERN-ATL-COM-DAQ-2007-006

[52] W. E. Cleland *et al.*
Receiver/Monitor System for the ATLAS Liquid Argon Calorimeter,
ATL-AL-EN-0043,

[53] [ATLAS Collaboration],
ATLAS Liquid Argon Calorimeter: Technical Design Report,
CERN/LHCC 96-41

[54] [ATLAS Collaboration],
ATLAS tile calorimeter: Technical design report, CERN-LHCC-96-42

[55] The ATLAS group at the KIP Heidelberg,
The Pre-Processor Module (PPM) for the ATLAS Level-1 Calorimeter Trigger

[56] E. Eisenhandler,
ATLAS Level-1 Calorimeter Trigger Algorithms,
CERN-ATL-DAQ-2004-011

[57] Cluster Processor Module,
Specification of the Cluster Processor Module for the ATLAS Level-1 Calorimeter Trigger Version 2.02

[58] Jet/Energy Processor Module,
Specification of the Jet/Energy Processor Module for the ATLAS Level-1 Calorimeter Trigger Version 1.2

[59] U. Pfeiffer,
A Compact Pre-Processor System for the ATLAS Level-1
Calorimeter Trigger
PhD Thesis, Institut für Hochenergiephysik der Universität
Heidelberg

[60] K. Penno,
A Test Enviroment for the ATLAS Calorimeter Trigger
Diploma Thesis, Kirchhoff Instisut für Physik der Universität
Heidelberg

[61] National Semiconductor
LVDS Owner's Manual - Low-Voltage Differential Signaling

[62] J. Redd,
Calculating Statistical Confidence Levels for Error-Probability Estimates
Lightwave Magazine, pp. 110-114,2000.

[63] J. Garvey, The UK Level-1 Trigger Group
Bunch Crossing Identification for the ATLAS Level - 1 Calorimeter Trigger
ATLAS Internal Note,
ATL-DAQ-96-051

[64] Achenbach,R
ASIC and MCM production, presented at Level-1 Calorimeter Trigger Joint Meeting, 2005

[65] The ATLAS group at the KIP Heidelberg,
Production Readiness Review (PRR) for the ASIC/MCM assembly

[66] Pfeiffer, U and Hötzel, W
Bunch-Crossing Identification for saturated calorimeter signals
ATL-DAQ-99-009, 1999

[67] Hinderer *et al.*,
The Final Multi-Chip Module of the ATLAS Level-1 Calorimeter Trigger

[68] Austria Micro Systems,
http://www.austriamicrosystems.com/

[69] Würth Elektronik GmbH & Co.
`http://www.we-online.com/`

[70] HASEC-Elektronik GmbH.
`http://www.hasec.de`

[71] The ATLAS group at the KIP Heidelberg,
Production Readiness Review (PRR) for the ASIC/MCM assembly

[72] LHCb software architecture group,
LHCb Data Processing Applications framework,
LHCb 98-064 COMP

[73] E. Richter-Was, D. Froidevaux and L. Poggioli,
ATLFAST 2.0, A fast simulation package for ATLAS, ATLAS note,
ATL-PHYS-98-131

[74] D. Cavalli, *et al.*
Performance of the ALTAS fast simulation ATLFAST, ATLAS note,
ATL-PHYS-INT-2007-005

[75] K. Mahboubi, K. Jacobs,
A fast parametrization of electromagnetic and hadronic calorimeter showers,
ATL-SOFT-PUB-2006-001

[76] Iacopo Vivarelli,
Jet calibration - Status report, ATLFAST Validation Meeting, 2006

[77] `https://twiki.cern.ch/twiki/bin/view/Atlas/FastCaloSim`

[78] P. Loch,
Suggestions for a General Energy Reconstruction Scheme for the ATLAS Calorimeters, ATLAS note, cal-97-091

[79] P. Loch,
Hadronic calibration with early data,
presented at ATLAS Calorimeter Calibration Workshop, Costa Brava, Sep, 2006

[80] Frank E. Page and Sanjay Padhi,
Rome jet calibration based on ATHENA 9.0.4, ATLAS note,

[81] C. Roda and I. Vivarelli,
Cell Based Jet Calibration, ATLAS note, ATL-PHYS-PUB-2005-019

[82] C. Cojocaru, et al.,
Nucl. Instrum. Meth. A531 (2004) 481-514

[83] A. Bhatti *et al.*, Nucl. Instrum. Meth. A **566** (2006) 375
[arXiv:hep-ex/0510047].

[84] W. Ashmanskas *et al.*, Part. Nucl. Lett. **5** (2002) 12.

[85] K. Peters,
Precision Calibration of the D0 HCAL in Run II,
[arXiv:physics/0608002]

[86] `http://projects.hepforge.org/pythia6/trac/ticket/6`

[87] V. Lendermann, P. Weber,
Calorimeter Intercalibration using Energy Flow method, presented at ATLAS Trigger & Physics Week, CERN, 2007

Acknowledgments

It's my pleasure to thank everyone whose support and assistance during these years made the appearance of this thesis possible.

First of all I would like to express gratitude to my supervisor Prof. Karlheinz Meier for providing an opportunity to work on frontier of modern physics. I'm very grateful for his support and encouragement of all my initiatives. I was always impressed by his physics enthusiasm and ability to share it with other people.

I would like to thank Dr. Paul Hanke, who was always very kind to me. The discussions we held from the first days and the answers he gave on my, sometimes naive, questions helped me a lot in understanding the ATLAS experiment and trigger particularly. I'm also very grateful for the important comments he made on the trigger part of the thesis.

My warmest thanks I would like to address to Dr. Kambiz Mahboubi. I appreciate much his readiness to help with any problem I had and continual assistance. I will always remember the long evenings we spent in the lab, solving the PPrASIC puzzles. I admire his excellent knowledge of the ATLAS physics and hardware he shared with me during our endless and exciting discussions, which were full of humor and fun.

I would like express my gratefulness to Klaus Schmitt for the outstanding help in the development of the Multi-Chip Module hardware tests. His intuitive understanding of an electronics resulted in simple and elegant solutions for the problems which we discussed.

I would like to thank Prof. Ulrich Uwer, who kindly agreed to be a referee of this work.

I'm very grateful to Dr. Victor Lendermann for his continual support and guidance during the second part of the thesis. I learnt a lot from him during the countless hours of discussion on calibration issues and physics analysis in general.

I would like to thank Prof. Hans-Christian Schultz-Coulon for the permanent interest in my work. Questions, critical comments and interesting suggestions he made during the presentations of my work in our weekly physics meeting were the matter of great importance for me.

I owe my thanks to Dr. Jürgen Stiewe, who kindly agreed to read my thesis and to make corrections and comments.

Many thanks go to Dr. Christoph Geweniger, who was always ready to discuss my work and to propose interesting suggestions.

I would like to thank Ralf Achenbach for the collaborative work in harsh environment of the KIP clean room. We've got a lot of fun and excitement testing the PPrASIC wafers and MCMs.

I also want to thank Prof. Eike-Erik Kluge for important comments of my work and kind attitude.

My next thanks go to Dr. Florian Föhlisch. We spent many years full of fun and not only sitting in the same office. It was always my pleasure to talk to him.

I also would like to thank Victor Andrei and Frederik Rühr for a number of fruitful discussions we had and for the time we spent outside.

My special thanks go to Dr. Iacopo Vivarelli with whom I had a few important discussions and permanent mail exchange.

I express my thanks to all colleagues from L1Calo collaboration. They are all very nice people. I was always glad to meet them and to have conversations during collaboration meetings.

Finally I would like to extend my thanks to the whole KIP Particle Physics group, which is expanding rapidly now. I have to mention Alexander Tadday, Dr. Jochen Dingfelder, Bernd Amend, Dr. John Taylor Childers III, Michael Henke, Felix Müller, Dr. Martin Wessels, Dr. Rainer Stamen, Ion Stroescu, Dr. Katja Krüger, Andreas Jung and Klaus Urban, whose support and friendly attitude I felt during the last few months.

My last, but the most thanks I would address to my family. I want to thank my parents for supporting me in all things I do. I would like to thank my dear wife Lena for the tremendous support and patience during all years I was busy with my thesis. I appreciate it very much, indeed. My last thanks go to my little daughter Elisa, who is the main source of joy and inspiration for me.